HZDR-062

SIMULATION STUDIES FOR THE IN-VIVO DOSE VERIFICATION OF PARTICLE THERAPY

Heide Rohling

Wissenschaftlich Technische Berichte
HZDR-062 · ISSN 2191-8716

WISSENSCHAFTLICH-
TECHNISCHE BERICHTE

HZDR
HELMHOLTZ
ZENTRUM DRESDEN
ROSSENDORF

Wissenschaftlich-Technische Berichte
HZDR-062

Heide Rohling

SIMULATION STUDIES FOR THE IN-VIVO DOSE VERIFICATION OF PARTICLE THERAPY

HZDR

HELMHOLTZ
ZENTRUM DRESDEN
ROSSENDORF

Druckausgabe: ISSN 2191-8708

Elektronische Ausgabe: ISSN 2191-8716

Qucosa: http://fzd.qucosa.de/startseite/

Die vorliegende Arbeit wurde sowohl als Dissertation an der Medizinischen Fakultät Carl Gustav Carus der Technischen Universität Dresden sowie als Wissenschaftlich-Technischer Bericht des Helmholtz-Zentrum Dresden – Rossendorf mit der Berichtsnummer **HZDR-062** veröffentlicht.

2015

Herausgegeben vom

Helmholtz-Zentrum Dresden - Rossendorf

Bautzner Landstraße 400

01328 Dresden

Germany

Aus dem OncoRay – National Center for Radiation Research in Oncology
Sprecher: Herr Prof. Dr. Michael Baumann

Simulation studies for the in-vivo dose verification of particle therapy

D i s s e r t a t i o n s s c h r i f t

zur Erlangung des akademischen Grades
Doktor der Medizintechnologie
Doctor rerum medicinalium (Dr. rer. medic.)

vorgelegt

der Medizinischen Fakultät Carl Gustav Carus
der Technischen Universität Dresden

von

Dipl.-Math. Heide Rohling

aus Bielefeld

Dresden 2014

1. Gutachter: Prof. Dr. Wolfgang Enghardt

2. Gutachter: Prof. Dr. Oliver Jäkel

Tag der mündlichen Prüfung: 8. Juni 2015

gez.: .....
Vorsitzender der Promotionskommission
(Prof. Dr. Edmund Koch)

Contents

List of Figures

List of Tables

List of abbreviations

BGO	Bismuth germanate
CT	Computed Tomography
CTR	Coincidence time resolution
CZT	Cadmium zinc telluride
DRES	Dresner model
EBITEM	ENSDF-Based Isomeric Transition and isomEr production Model
ENVISION	European NoVel Imaging Systems for ION therapy
FOV	Field-Of-View
FWHM	Full width at half maximum
GEM	Generalized Evaporation Model
Gy	Gray
GyE	Gray Equivalent
GSI	GSI Helmholtzzentrum für Schwerionenforschung GmbH
HIMAC	Heavy-Ion Medical Accelerator in Chiba
HU	Hounsfield unit
HZDR	Helmholtz-Zentrum Dresden-Rossendorf
IFIC	Institut de Fisika Corpuscular
IMP	Institute of Modern Physics, Chinese Academy of Sciences
IMRT	Intensity-Modulated Radiotherapy
INC	Intra-Nuclear Cascade model
IP	Incident particle
KVI	Kernfysisch Versneller Instituut
LET	Linear Energy Transfer
LSO	Lutetium oxyorthosilicate
LYSO	Lutetium yttrium orthosilicate

MAP	Maximum-A-Posteriori
MLEM	Maximum-Likelihood Expectation-Maximization
NIRS	National Institute of Radiological Sciences
OncoRay	National Center for Radiation Research in Oncology, Dresden
OSEM	Ordered-Subset Expectation-Maximization
PET	Positron Emission Tomography
PGI	Prompt Gamma Imaging
PMMA	Polymethyl methacrylate
PT-PET	Particle Therapy Positron Emission Tomography
QMD	Quantum Molecular Dynamics model
RBE	Relative Biological Effectiveness
RMSE	Root Mean Square Error
ROI	Region Of Interest
RPC	Resistive Plate Chamber
SDM	Statistical Decay Model
SPECT	Single-Photon Emission Computed Tomography
SNR	Signal-to-Noise Ratio
TOF	Time-of-flight
YaPET	Yet another PET Evaluation Tool

1 Introduction

Despite all advances in medical research, cancer is still one of the most lethal diseases. About 44 % of all cancer patients in Germany do not survive the first five years following the diagnosis (Kaatsch et al., 2013). The treatment of malignant diseases is mainly based on surgical removal of the affected tissue, cytotoxic chemotherapy, radiotherapy, or combinations thereof, the individual strategy of the treatment is dependent on the type and stage of the illness. At present, cancer research is focused on the one hand on the diagnosis in an early stage of the malignancy, this includes e.g. medical imaging. On the other hand, the treatment is improved regarding high tumor control rates and the prevention of late side effects. Much effort is currently put into the study of cancer biology resulting in the development of new drugs. For instance, cancer genome studies are carried out aimed at the identification of all mutations leading to the uncontrollable cell growth (Stratton, 2009). Radiotherapy, although being applied for more than one hundred years, is still a subject of research. Nowadays, about 50 % of all cancer patients receive radiotherapy (Baskar et al., 2012), which is standardly performed with X-rays (bremsstrahlung) or electrons, either with an external beam (teletherapy) or by means of a radioactive source brought into the tumor region (brachytherapy). One example for a recent improvement in photon therapy is Intensity-Modulated Radiotherapy (IMRT) which has become routine in more and more clinics. Furthermore, a growing and promising field of research is radiotherapy with proton beams and other light ion beams.

Proposed for the first time in 1946 (Wilson, 1946), therapeutic irradiation with protons or other light ions is currently supplied by about 40 facilities in the world (Particle Therapy Co-Operative Group, 2013) and many more are planned or under construction. Most of the facilities in operation perform treatments with proton beams and a few particle therapy centers provide carbon ion beams for therapeutic irradiation of tumor patients. The ions are typically accelerated up to energy values that correspond to a particle range in water of about 30 cm and directed to the tumor region. This kind of radiotherapy profits from the advantageously distributed dose deposition inside matter: for ions the maximum of the depth dose curve is close to the end of their range, at the so-called Bragg peak, which is followed by a sharp decline of dose. The range of the beam particles is adjusted by the variation of the incident energy. In this way, the tumor volume can be covered by the superposition of several Bragg peaks. Since the beam particles are stopped completely

in the tissue and with the position of the Bragg peak set to the tumor region, an exact application of high dose to the tumor is possible while sparing the surrounding normal tissue. In contrast to proton beams and other light ion beams, photons deposit the maximal dose close to the skin, followed by an exponential decrease of dose with the depth. Thus, particle therapy provides a clear advantage over conventional treatment with photons, especially, with respect to the treatment of deep-seated tumors in close vicinity to organs at risk, like the brain stem and optic nerves. Due to the favorable depth dose profile of ions in matter, particle therapy is for some types of tumors the only option to treat the patient in a successful way.

The advantageous dose distribution of light ions in tissue is also one of the major risks of particle therapy. In contrast to conventional irradiation with photons, the precision of dose delivery with particle beams is very sensitive to small density changes in the irradiated volume and fatal deviations between the actual and the prescribed dose application can result. If the tumor is not entirely irradiated and normal tissue receives a high dose instead, the success of the treatment is endangered and severe side effects can occur. Deviations from the treatment planning can be patient-specific, for example caused by changes in the patient's tissue. During the usually week-long treatment, variations in the tissue density due to tumor shrinkage or mucus-filled cavities are not uncommon. Furthermore, neither an incorrect positioning of the patient, nor systematic errors in the treatment plan can be excluded. Therefore, a non-invasive, in-vivo monitoring of the dose deposition is highly desired to ensure the best therapeutic outcome.

In-vivo dose monitoring of particle therapy is based on the detection of secondary radiation which occurs when the particle beam interacts with the nuclei of the patient's tissue. Up to now, the only clinically proven method for dose monitoring of ion beam therapy is Particle Therapy Positron Emission Tomography (PT-PET). This technique makes use of the β^+-radionuclides resulting from nuclear reactions along the path of the beam. With PT-PET the annihilation photons following the annihilation of the positrons which originate from the β^+-decay are detected. Another strategy for the monitoring of radiotherapy with ions heavier than protons is based on the detection of secondary protons which appear as fragments from nuclear reactions between the projectiles and the nuclei of the target. This technique is called Interaction Vertex Imaging (Henriquet et al., 2012). Another approach is Prompt Gamma Imaging (PGI). PGI is based on the detection of the prompt γ-rays emitted after the excitations of the nuclei of the human tissue during therapeutic irradiation. Different concepts concerning the detection of these prompt γ-rays are followed at the moment. One approach relies on the Compton effect. The dedicated hardware, which is under investigation, e.g. at National Center for Radiation Research in Oncology, Dresden (OncoRay) in collaboration with the Helmholtz-Zentrum Dresden-

Rossendorf (HZDR), is called Compton camera.

The project European NoVel Imaging Systems for ION therapy (ENVISION) funded by the European Commission under FP7 Grant Agreement number 241851 dealt with all challenges of the in-vivo dosimetry for particle therapy. Fifteen European research centers and one company were involved in this project.

Supported by ENVISION, this thesis contributes to the progress of particle therapy monitoring by means of simulations. In chapter 2 the fundamental principles of particle therapy and the state of the art of in-vivo dosimetry for particle therapy using either PT-PET or PGI are described in detail. In chapter 3 the secondary radiation which is the basis for particle therapy monitoring with PT-PET and PGI, respectively, is considered. The production of β^+-emitting nuclei and the prompt γ-ray emissions during particle irradiation are modelled by particle transport simulation codes. The second topic of this thesis is the optimization of dedicated detection systems for PGI (chapter 4) and PT-PET (chapter 5). Chapter 4 deals with the Compton camera, including recommendations for the setup of the prototype and a discussion of suitable event filters. In chapter 5 an evaluation of a detector based on Resistive Plate Chambers (RPCs) for the application to PT-PET can be found. RPCs are compared to scintillator-based scanners which have already been applied to this purpose. All simulation parameters are chosen to model reality as accurately as possible and comparisons to available experimental data are given. For the analysis in chapter 5 real patient data are used. Finally, in chapter 6 conclusions and an outlook concerning the application of new detector systems to particle therapy monitoring are given.

2 Physical and technological background of particle therapy monitoring

2.1 Particle therapy

Radiotherapy, either applied with photons, electrons, or particles (protons and light ions), relies on energy transfer of the projectiles to the tumor cells. Excitations and ionizations of atoms and molecules of the tissue are induced and lead to biological modifications of the cells. Cell death results if the DNA of the cells is damaged and repair mechanisms fail. A measure of the mean energy loss along the path of particles in matter is the Linear Energy Transfer (LET):

$$LET := \frac{dE}{dx} \tag{2.1}$$

with E being the energy and x the distance. The energy loss along the path of charged ions can be calculated as a function of the type of the projectile and the target material with the Bethe-Bloch formula (Bethe and Ashkin, 1953). By integrating the inverse of (2.1), the range of the particles can be determined. The effect of ionizing radiation on tissue is quantified by the absorbed dose which is a measure of the energy deposition per mass with the unit Gray (Gy), equal to $\mathrm{J\,kg^{-1}}$. The higher the dose applied to the tumor, the higher the tumor control rate. For a curative treatment about 60 to 70 Gy are required.

The limiting factor for dose in radiotherapy is the dose deposition in normal tissue. Therefore, the favorable depth dose distribution of protons and other light ions in matter, which is due to their physical properties, makes particle therapy advantageous over conventional treatment with photons. At the moment, it is unclear which ion species is best suited for a therapeutic irradiation due to a lack of systematic studies, but an optimum is assumed for ions with atomic numbers between one and six (Eickhoff and Linz, 2008). Therapeutic ion beams of the same dose but different atomic numbers differ with respect to the biological effect which is quantified as Relative Biological Effectiveness (RBE). The RBE for one specific type of particles gives the ratio of the applied dose to the dose of a therapeutic irradiation with photons which is needed to produce the same effect on the tissue. While for protons the RBE is hardly higher than 1 at the Bragg peak (Paganetti et al., 2002), carbon ions provide an enhanced RBE in the Bragg-peak region (Kraft, 2000).

Thus, for carbon ion therapy, the dose is measured in Gray Equivalent (GyE). A dose given in GyE produces the same biological effect as the dose in a therapeutic irradiation with photons of one specific energy measured in Gy. The RBE of ions was already studied decades ago (Blakely et al., 1980). Carbon ions are better capable of treating hypoxic areas and show less lateral straggling than protons (Schardt et al., 2010a). On the other hand, compared to proton irradiation, the distal fall-off behind the Bragg-peak is not as sharp due to fragments of the incident carbon ions which have a larger range than the primary particles (Schardt et al., 2010a). Exploiting the influence of the cell cycle and better recovery of normal cells compared to malignant cells, conventional radiotherapy is usually performed in daily fractions of 1.5 to 3 Gy (Baskar et al., 2012). For proton therapy usually a similar treatment regime of circa 2 Gy per fraction is used. For carbon ions the repair capacity of normal cells is reduced compared to photons and protons (Hall and Garcia, 2012) making hypofractionation reasonable. As a result, the patient throughput could be enhanced. Aside from protons and other light ions, further particles are considered for therapeutic irradiation. Neutrons have been used because of their high RBE and their favorable behavior concerning hypoxia, but neutrons show a high level of damage to normal tissue (Hall and Giaccia, 2012). Also pion beams have already been applied (Von Essen et al., 1987) and even antiprotons are under consideration for medical application (Bassler et al., 2008; Bittner et al., 2014).

According to estimations, 13.5 % of all patients who receive radiotherapy are candidates for particle therapy (Mayer et al., 2004). For certain types of tumors particle therapy is already the treatment of choice. For example, therapeutic proton irradiation of eye cancer is widely applied since it allows eye preservation (Kacperek, 2012). For tumors at the skull base particle therapy can provide sufficient sparing of critical organs while delivering a dose which is high enough to stop tumor growth. High local control rates are obtained for these tumors which often cannot be resected completely by surgery. In particular, the tumor control rate of chordoma patients raised distinctly after establishing ion beam therapy as a standard treatment for those patients (Schulz-Ertner, 2012). For pediatric tumors the reduction of secondary malignancies and late toxicity is expected (Woo, 2012). For other tumors the investigations of the advantages of particle therapy compared with conventional treatment are still ongoing. Further studies include the combination of particle therapy with chemotherapy and the optimization of dose and fractionation, taking into account local control rates, toxicity, and economic questions. For example, within a clinical study with carbon ions at National Institute of Radiological Sciences (NIRS), Japan, lung cancer patients received the total curative dose in one session (Takahashi et al., 2014). In another recent study promising results for pancreatic cancer were achieved by combining carbon ion treatment with high dose chemotherapy (Shinoto et al., 2013).

The main restriction of particle therapy is the availability of particle accelerators which provide a sufficient energy for the projectile particles. For conventional radiotherapy with photons, electron linear accelerators are used in industrialized countries, which are standardly fabricated, of compact size, and operated in clinical routine in many hospitals. For particle therapy a more powerful and comparatively expensive circular accelerator is necessary. Protons for medical application are usually accelerated with an isochronous cyclotron to more than 200 MeV. For carbon ion therapy an even larger and more expensive synchrotron is required. Concerning the techniques of particle therapy monitoring described in the following, the type of accelerator is of importance: cyclotrons deliver a continuous beam while beam bunches are extracted from a synchrotron. Thus, using a synchrotron, there are pauses between beam extraction cycles in the range of seconds. Several approaches aimed at the reduction of energy and costs are currently under investigation, e.g. the acceleration of protons by means of a laser (Zeil et al., 2013).

The success of a therapeutic irradiation with protons or other light ions relies on the precise application of sufficient dose to the tumor volume. In order to ensure the quality of the treatment, a control of the agreement between the prescribed and the actual dose deposition is required. This monitoring has to be non-invasive and as fast as possible. If a deviation from the prescribed dose is observed, the reason for this deviation has to be found and appropriate corrections have to be taken before the next treatment session starts. This can include a new treatment plan, a new Computed Tomography (CT) scan, and the intake of decongestant medicines. Optimally, a monitoring system is able to detect deviations during an ongoing therapeutic irradiation and alarm the medical staff to stop immediately in case of an unexpected dose deposition.

2.2 Particle Therapy Positron Emission Tomography (PT-PET)

Positron Emission Tomography (PET) is a standard method in nuclear medicine for the diagnosis and staging of various illnesses. This method is based on a β^+-radioactive substance injected into the patient prior to the PET scan. The uptake and distribution of this radiopharmaceutical agent in the patient's body depends on specific metabolic processes and can indicate a disease. A β^+-emitting nucleus, also referred to as positron-emitting nucleus, decays by releasing a positron (e^+) and a neutrino (ν) into a nucleus with the same mass number (A) but an atomic number (Z) reduced by 1:

$$ {}^{A}_{Z}X \rightarrow {}^{A}_{Z-1}Y + e^+ + \nu \tag{2.2} $$

The resulting positron annihilates with an electron of the tissue. This annihilation process is accompanied by usually two annihilation photons which travel in opposed directions

and each of them has an energy of 511 keV. By detecting the annihilation photons escaping from the patient's body, the distribution of the positions of annihilations can be deduced and, thereby, the distribution of the injected substance is revealed.

The first application of PET to the range verification of particle therapy was performed at Lawrence Berkeley National Laboratory in Berkeley, USA (Llacer et al., 1984) by means of radioactive beams. This technique was later also applied at Heavy Ion Medical Accelerator in Chiba (HIMAC) in Japan (Iseki et al., 2004). The aim was to verify the range of the beam particles prior to the treatment with a low-intense β^+-radioactive beam. In contrast to this, PET was also proven feasible for stable therapeutic beams by making use of the β^+-radioactivity which is produced by nuclear fragmentation reactions between the beam particles and the nuclei of the human tissue. Compared to PT-PET measurements for β^+-radioactive ion beams, the β^+-activity resulting from fragmentation processes is low. On the other hand, radioactive probing beams require effort concerning the isotope separation and the shielding of the primary beam. Therefore, this technique is not applied any more and is not considered in the following. At GSI Helmholtzzentrum für Schwerionenforschung GmbH (GSI) in Darmstadt, PT-PET was performed to monitor the treatment with ^{12}C ions of more than 400 patients during the pilot study from 1997 to 2008 (Enghardt et al., 2004). Range deviations corresponding to 6 mm in water were detected with a sensitivity higher than 90 % (Fiedler et al., 2010a). For proton radiotherapy the clinical application of PT-PET was also evaluated (Parodi and Enghardt, 2000; Parodi et al., 2002; Knopf et al., 2009; Parodi et al., 2007; Nishio et al., 2010). In addition to this, the feasibility of PT-PET was demonstrated by experiments for ^{7}Li (Priegnitz et al., 2008), ^{3}He (Fiedler et al., 2006; Fiedler, 2008), and ^{16}O (Sommerer et al., 2009). Up to now, PT-PET is the only method which has been successfully applied to the in-vivo dose verification of particle therapy.

The monitoring of particle therapy by means of PT-PET is a complex procedure due to the fact that the applied dose is not directly correlated to the distribution of the β^+-emitting nuclei. This is caused by the different underlying physical processes: dose is deposited by interactions with the electrons of the tissue, whereas β^+-activity is generated via peripheral nucleus-nucleus collisions. There are two solutions to obtain the distribution of the dose from the measured activity distribution: one approach is the use of an analytical convolution algorithm (Parodi and Bortfeld, 2006; Attanasi et al., 2011; Frey et al., 2014). This approach is considered for the range verification of therapeutic proton beams, not for other ion beams. The second and established method to predict the distribution of the β^+-activity is based on Monte Carlo simulations. By comparing the simulated to the measured distributions of annihilation points, deviations from the prescribed dose can be detected. This simulation takes into account the production of the relevant β^+-emitters,

their decay, the distribution and the transport of the positrons, and the propagation of the annihilation photons, as well as their detection (Hasch, 1996; Pönisch et al., 2004). It has to be performed for each each patient and each irradiation field individually, based on the treatment plan, and dependent on the time structure of the irradiation. Finally, the measured as well as the simulated data are reconstructed with the same algorithm and both distributions are compared to each other (Enghardt et al., 2004). To obtain reliable results, the washout of the β^+-emitters in the patient has to be considered which has large impact (e.g. Fiedler et al., 2008; Mizuno et al., 2003; Tomitani et al., 2003, Knopf et al., 2009, Hirano et al., 2013,). If moving volumes, e.g. lesions in the lung or liver are treated, patient motion during the PET acquisition has also to be taken into account. Suitable methods for motion-compensated PT-PET are developed (Parodi et al., 2009; Laube et al., 2013; Stützer et al., 2013) .

A basic physical process to be considered for the modelling of the expected distribution of annihilation points is the production of the β^+-emitting nuclei along the beam path. This step requires the total cross sections of the interactions between projectile and target nuclei, the reaction cross sections, i.e. the probabilities for the specific reaction channels, and the transport of the fragments. The most abundant β^+-emitting nuclei generated during therapeutic irradiation are ^{11}C, ^{15}O, ^{13}N, and ^{10}C with half lives of 20 min, 2 min, 10 min, and 19 s, respectively. While during a proton treatment β^+-emitting nuclei only result from target fragmentation, ^{11}C and ^{10}C also appear as projectile fragments during therapeutic irradiation with ^{12}C ions. The Monte Carlo simulations predicting the β^+-activity during the carbon ion pilot study at GSI (Hasch, 1996) made use of semi-empirical total reaction and fragmentation reaction cross section models (Sihver et al., 1993; Sihver and Mancusi, 2009). An alternative way to obtain the depth-dependent yields of β^+-emitting nuclei is to measure thick target yields. For example, the yields can be deduced from PET measurements performed during and directly after the irradiation. The number and type of the decaying β^+-emitting nuclei can be derived with a fitting procedure which is based on the half-lives of the nuclei (Parodi et al., 2002). A yield database for lithium and carbon ion irradiation was established this way (Priegnitz et al., 2012).

For the application of PT-PET it is crucial to consider the structure of the beam application. Data acquisition of the annihilation photons during beam extraction is difficult due to the high background produced by prompt γ-rays (Enghardt et al., 2004). For this reason, clinical PT-PET has either been performed during the spill pauses of a synchrotron beam or after the irradiation. The former technique is called in-beam PET, the latter in-room or off-line PET, depending on the availability of a PET scanner inside the treatment bunker. None of the concepts in-beam, in-room, and off-line PET is best with respect to all of

the following aspects: costs, image quality, and disturbance of clinical routine (Shakirin et al., 2011). The choice mainly depends on the environment in the treatment facility, in particular on the type of accelerator.

Off-line PET measurements are started several minutes after the irradiation because of transport and repositioning of the patient. This method suffers from low count rates, since many β^+-emitters have decayed before the start of the PET measurement. Another problem is the washout of the positron-emitters mainly caused by blood flow. In addition to this, if the patient is treated with two fields, the activity from the fields interfere and can make off-line PET infeasible, e.g. for two opposing fields. In this case it would be optimal to perform PT-PET after the application of the first field. This is a challenge concerning the disturbance of the clinical routine. However, it was demonstrated by a clinical study that offline PET-CT measurements can provide quality assurance of proton therapy (Parodi et al., 2007). Recently, clinical experiences with off-line PET-CT applied several minutes after the treatment with carbon ions were described (Bauer et al., 2013).

If, in contrast to off-line PET, a PET camera is available in the treatment room and the patient is moved there instantaneously after the irradiation without being repositioned, the monitoring is called in-room PET. This concept requires a PET camera with a transport system. However, higher count rates can be provided with in-room PET than with off-line PET (Shakirin et al., 2011).

During the pilot study at GSI, therapy monitoring was successfully conducted with in-beam PET. Since the PET-signal was corrupted during beam extraction, about 40 % of the true coincidences could not be used for the reconstruction. An idea to overcome this loss of data is to make use of the radio frequency of the beam delivery (Parodi et al., 2005). A recent study considered in-beam PET for a continuous cyclotron beam using a detector with a low dead time to reduce the background (Sportelli et al., 2014). However, this study only comprises irradiated homogeneous phantoms. Another challenge of in-beam PET is that a standard full-ring scanner is not applicable to avoid interference with the therapeutic beam. At GSI a double-head PET camera made of bismuth germanate (BGO) was integrated into the treatment site (Enghardt et al., 2004). Each head had a size of $42 \times 21\,\mathrm{cm}^2$ (Enghardt et al., 2004). This geometry prevented optimal image quality due to limited angle artifacts (Shakirin, 2009). Simulation studies of further double-head scanners with different geometries of larger solid angle coverage are promising (Shakirin, 2009). Tilted scanners or two scanners with a gap in-between (”OpenPET”) are also studied for this purpose (Tashima et al., 2012).

Once the PET measurements are taken, the β^+-activity needs to be reconstructed. To-

mographic reconstruction is either performed with analytical or algebraic algorithms. Usually, the reconstruction of three-dimensional PET data is performed with an algebraic method: the iterative Maximum-Likelihood Expectation-Maximization (MLEM) algorithm or a derivative method. This procedure provides the comfortable incorporation of corrections. For in-beam PET algebraic methods are used exclusively, since analytical methods are not applicable due to the low count rates and the detector geometry (Lauckner, 1999). In this work it is assumed that the measured data is stored in list-mode data format, i.e., for each registered pair of photons the channel between the positions of detection and the corresponding time stamps are saved individually. A version of the original MLEM (Shepp and Vardi, 1982) adapted to list-mode data is applied in this work. Let vector $b \in \mathbb{R}^N$ represent the channels of detection, with N being the number of events. The space where the annihilations occur is discretized to a field of three-dimensional bins (voxels). The vector containing the voxel values is in the following named $f \in \mathbb{R}^M$ with M being the number of voxels. The relation between image f and measured data b is given by the linear equation (2.3).

$$Af = b \tag{2.3}$$

In equation (2.3) $A \in \mathbb{R}^{N \times M}$ denominates the so-called system matrix. It contains the probabilities a_{ij} for an annihilation in voxel j to be detected as event i ($\forall\, i = 1, ..., N$ and $\forall\, j = 1, ..., M$).

MLEM relies on the redistribution of activity for each event in the channel linking the two positions where the annihilation photons were registered. In the first step of the reconstruction algorithm, f is initialized with arbitrary, usually homogeneous, non-negative values. Then, in each iteration $n \in \mathbb{N}$ of the MLEM reconstruction procedure, f is updated, cf. equation (2.4), with convergence to the emission distribution that agrees best with the measurement b.

$$\text{MLEM:} \quad f_j^{n+1} := \frac{f_j^n}{\sum\limits_{i=1}^{N} a_{ij}} \sum_{i=1}^{N} \frac{a_{ij}}{\sum\limits_{j'=1}^{M} f_{j'}^n a_{ij'}} \tag{2.4}$$

This iterative method is derived from the maximization of an objective function which represents the probability for the measured events to originate from the emission distribution f (Shepp and Vardi, 1982). Thus, the objective function is based on the Poisson distribution of the PET-signal, i.e. the radioactive decay in a certain voxel of the source. Convergence and positivity of the image values have been proven (Shepp and Vardi, 1982). The term $\sum\limits_{i=1}^{N} a_{ij}$ is used to compensate for the different detection probabilities for emissions occurring in different voxels. It is often replaced by the precalculated value of

detection efficiency s_j for each voxel j, $j = 1, ..., M$.

Due to the size of the system matrix, its calculation and storage are challenges of three-dimensional PET reconstruction. The fastest solution is the use of the *on-the-flight* system matrix (Lauckner, 1999; Shakirin, 2009): the matrix is not stored, but in each step of the reconstruction the corresponding part of the system matrix is calculated for each event ”on-the fly”, i.e., when it is needed.

In the ideal case, corrections for all physical processes affecting the measured events are taken into account. For instance, a correction for random coincidences is required. Furthermore, the different detection efficiencies of the crystals of a PET camera also have to be considered. Corrections regarding the attenuation and scattering in the patient's tissue and close environment should be included. Information derived by CT scans are used as basis for the correction of scattering and attenuation. The mentioned corrections are applied in each iteration of the MLEM algorithm (Lauckner, 1999; Pönisch et al., 2003).

Many variations of the MLEM algorithm exist. One approach is the Ordered-Subsets Estimation-Maximization (OSEM) which only considers a subset of events in each step of the procedure, instead of taking into account all events. OSEM has already been applied successfully to PT-PET (Shakirin, 2009). A possibility to include additional information into the reconstruction procedure is the use of a Maximum-A-Posteriori (MAP) algorithm. The objective function is modified with the aim to reduce noise and, thereby, smooth the image (Qi and Leahy, 2006).

During the MLEM algorithm contrast increases, but noise increases, too. In order to obtain an optimal image with MLEM, the algorithm can be stopped after a certain number of iterations. Another way to reduce noise is the filtering. For PT-PET the application of a median filtering is highly recommended after each iteration step (Shakirin, 2009). For each voxel its value is replaced by the median of this voxel and the 26 neighboring ones.

For the assessment of the quality of reconstructed images several figures of merit are in use, e.g. the Signal-to-Noise Ratio (SNR) with different definitions in the literature and the Root Mean Square Error (RMSE), cf. equation (2.5), with f being the calculated image and f^* the true one:

$$\text{RMSE} := \sqrt{\frac{1}{M}\sum_{j=1}^{M}(f_j - f_j^*)^2}. \tag{2.5}$$

A parameter to adjust for the reconstruction is the size of the voxels: the lower the voxel size the better the resolution and the visibility of small lesions or deviations, but the higher the noise due to sparsely populated voxels. Furthermore, the voxel size has impact on the runtime of the reconstruction procedure. For three-dimensional PET usually voxel sizes of one quarter of the crystal length of the applied scanner are used (Lauckner, 1999). For in-beam PET the effect of the voxel size was already studied for the PET camera at GSI consisting of crystals with a length of 6.75 mm with the conclusion that 2 mm voxel length still guarantees high image quality (Shakirin et al., 2008).

Modern crystal-based PET scanners provide a sufficient time resolution to make the incorporation of time-of-flight (TOF) information in the reconstruction procedure advantageous. TOF denominates the time difference between the registrations of the two annihilation photons. Thus, an additional information about the annihilation place is provided, since photons travel with the speed of light. With Δt being the coincidence time resolution (CTR), the point of annihilation can be determined with the accuracy Δx:

$$\Delta x = c \cdot \Delta t/2. \tag{2.6}$$

Consequently, for a commercially available PET scanner providing a CTR of 600 ps full width at half maximum (FWHM), a spatial resolution of 9 cm FWHM is obtained. This is obviously not sufficient to directly determine the position where the annihilation has taken place. Nevertheless, the TOF information can be included into the MLEM algorithm (TOF-MLEM) (Groiselle et al., 2004; Shakirin, 2009). Let $\mathbf{p_1}, \mathbf{p_2} \in \mathbb{R}^3$ be the two positions of detection, t_1 and t_2 the points in time of registration at $\mathbf{p_1}$ and $\mathbf{p_2}$, respectively, $\Delta\text{TOF} = t_2 - t_1$, and c the speed of light, then

$$\mathbf{Q} := \frac{\mathbf{p_1} + \mathbf{p_2}}{2} + \frac{\mathbf{p_1} - \mathbf{p_2}}{|\mathbf{p_1} - \mathbf{p_2}|} \cdot c \cdot \frac{\Delta\text{TOF}}{2} \tag{2.7}$$

is the most probable place of annihilation. In the MLEM algorithm without the use of TOF, equation (2.4), the probability function representing the potential origin of the pair of measured photons is a uniform distribution along the corresponding channel. By including TOF, this distribution is altered to a Gaussian distribution centered at point $\mathbf{Q}$ with the density function $\varphi_{Q,\sigma}$. The standard deviation σ is usually set according to the time resolution of the scanner. Based on the MLEM algorithm defined in equation (2.4), the detection probability a_{ij} is changed to $t_{ij}a_{ij}$ in the TOF-MLEM technique where t_{ij} is the function value of the density function $\varphi_{Q,\sigma}$ at C_j, the center of the j-th bin:

$$\text{TOF-MLEM:} \quad f_j^{n+1} = \frac{f_j^n}{\sum\limits_{i=1}^{N} a_{ij}} \sum_{i=1}^{N} \frac{t_{ij}a_{ij}}{\sum\limits_{j'=1}^{M} f_{j'}^n t_{ij'}a_{ij'}} \text{ with } t_{ij} := \varphi_{Q,\sigma}(C_j). \tag{2.8}$$

For diagnostic PET many studies are published which evaluate the impact of the use of TOF-MLEM with respect to MLEM. With TOF information the MLEM converges faster and the images are of higher quality than without the use of TOF (e.g. Surti et al., 2006; Moses, 2003; Lois et al., 2010). Using TOF, the reduction of noise results not only from the favorable redistribution of activity, but also from the suppression of scattered and random events (Moses, 2003). The total impact of TOF on the SNR is the higher, the better the time resolution and the larger the object. As a consequence, TOF is especially beneficial for adipose patients (e.g. Lois et al., 2010). Furthermore, TOF-MLEM is robust to inconsistent data used for the correction of scattering, attenuation, normalization, and respiratory artifacts (Conti, 2010). For the application to in-beam PET, TOF has another crucial advantage: TOF-MLEM has the potential to overcome elongation artifacts caused by the double-head geometry of the PET camera (Crespo et al., 2006; Shakirin, 2009) due to the reduction of random and scatter coincidences. Further results indicate that TOF can compensate for low count rates (Surti et al., 2006), an advantage particularly useful in PT-PET.

For a CTR better than 200 ps FWHM, the Direct TOF algorithm is applicable (Crespo et al., 2007). The Direct TOF procedure consists of only one step in which the recorded events are back projected using the time information. With equation (2.7), the activity is allocated to exactly one voxel, the one containing the position $\mathbf{Q}$. Corrections, e.g. for the geometrical configuration of the scanner, can be applied in the same way as included in MLEM. Due to the available time resolution for commercially available PET scanners, this method was not yet applied in clinical routine, but was studied by simulations (Crespo et al., 2007; Shakirin, 2009). It has the advantage of a fast runtime, and could potentially allow for a reconstruction within a few seconds.

Therefore, with respect to PT-PET, lutetium oxyorthosilicate (LSO) or cerium-doped lutetium yttrium orthosilicate (LYSO) are favorable over BGO due to their better CTRs, which allow TOF-MLEM. For a commercially available LYSO-based scanner a CTR of 600 ps FWHM is provided (Surti et al., 2007). Independently from PT-PET, advances concerning the time resolution of crystals have been achieved. Even a CTR of 100 ps FWHM is possible for a single crystal (Schaart et al., 2010). Beside scintillators, multi-gap Resistive Plate Chambers (RPCs) are currently studied regarding the application to in-beam PET. A simulation study was performed (Diblen et al., 2012) and an experimental analysis with a 4-gap RPC-prototype was conducted (Watts et al., 2013). Multi-gap RPCs consist of a stack of resistive material (glass or ceramic) with gas-filled gaps in-between. If an incident photon interacts in a resistive plate and a secondary electron escapes into the gas and produces an electron avalanche, a signal is induced. RPCs have also been suggested for the construction of full-body PET scanners for diagnostic purposes due to its cheap

material and an already achieved CTR of 300 ps FWHM (Blanco et al., 2003; Georgiev et al., 2013). An even better CTR is expected soon (Watts, 2013). However, RPCs provide only a low detection efficiency compared to scintillators. For a 4-gap RPC a detection efficiency for single photons of 0.66 % is reported (Watts et al., 2013). In order to address this problem, RPC-based photon counters of many stacks are suggested (Blanco et al., 2003; Watts et al., 2013).

2.3 Prompt Gamma Imaging (PGI) for in-vivo dosimetry

Aside from PT-PET, an approach to establish a dose verification of particle therapy is based on PGI. During therapeutic irradiation with ions γ-rays are emitted almost instantaneously. These prompt γ-rays result from deexcitation processes following the interactions of the beam with the nuclei of the target. Since the delay between excitation of the nuclei and emission of the prompt γ-rays is in the range of femto seconds, washout of the activity is not relevant. This is a clear advantage in comparison with PT-PET. Furthermore, the application of PGI to the in-vivo dose verification is independent from the type of accelerator. A convolution technique similar to the one for PET (Parodi and Bortfeld, 2006) which calculates the dose from the measured γ-rays is anticipated for PGI. However, PGI in this context requires dedicated hardware and has not been clinically applied yet.

In order to provide an appropriate detector system, the knowledge of the rate and energy distribution of prompt γ-rays emitted during particle therapy is necessary. Measurements of prompt γ-ray emissions during particle irradiation are ongoing. Therefore, Monte Carlo simulations were performed to compensate for the lack of data. By means of GEANT4 simulations (Agostinelli et al., 2003) and real treatment plans, the energy spectrum of prompt γ-rays was studied for a proton treatment (Müller et al., 2012). With the latest GEANT4 version 10.0p01 the spectrum depicted in figure 2.1 was obtained for the irradiation of a target consisting of polymethyl methacrylate (PMMA) with protons of 150 MeV. These data were provided by Andreas Schumann (OncoRay / HZDR). The number of protons applied in this simulation (10^8) corresponds to a total dose of about 0.1 Gy. Per incident proton on average about 0.1 prompt γ-rays are emitted in an energy range up to 15 MeV. First experimental studies in this context are aimed at the question how the measured γ-rays can be correlated to the applied dose. A relation between the sharp decline of the dose behind the range of the particles and the measured γ-ray emissions was found (Min et al., 2006). Another experimental study reveals correlations between the appearance of prominent lines in the energy spectrum and the end of the range of the beam particles (Verburg et al., 2013), which were earlier found by simulations (Fiedler et

al., 2010b). All studies come to the result, that the energy range for photons emitted during therapeutic particle irradiation reaches from a few keV to several MeV and presents prominent peaks, e.g. at 2.2 MeV, 4.4 MeV, and 6.1 MeV. The peak at 2.2 MeV results from the neutron capture in hydrogen (Firestone, 2004), whereas the prompt γ-rays with 4.4 MeV and 6.1 MeV are emitted when excited ^{12}C and ^{16}O nuclei turn back to their ground states, respectively (Kozlovsky et al., 2002).

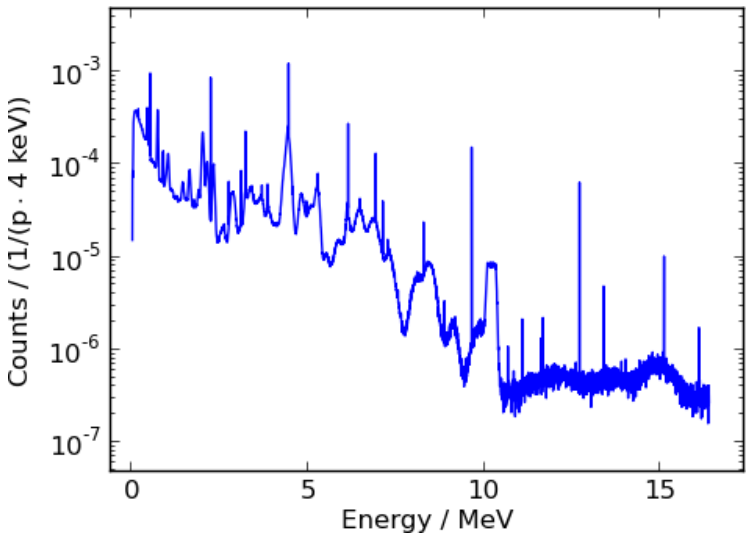

Figure 2.1: Energy spectrum of prompt γ-rays emitted during the irradiation of a PMMA target ($10 \times 10 \times 20$ cm^3) with 10^8 protons of 150 MeV simulated with GEANT4 version 10.0p01 using the *physics list* QGSP_BIC_HP. These data were provided by Andreas Schumann (OncoRay / HZDR).

Photons undergo scattering and absorption processes in material. For the energy range expected for prompt γ-rays emitted during therapeutic particle irradiation the relevant processes are photoelectric effect, incoherent scattering, and pair production of an electron-positron pair. The probabilities for these processes to occur depend on the energy of the photons and on the type of material, cf. table 2.1.

Table 2.1: Cross sections of photon processes dependent on the photon energy (E) and the atomic number (Z) of the nuclides of the target (Bethge et al., 2008).

Process	Function of Z	Function of E
Photoelectric effect	$Z^4 - Z^5$	$E^{-3.5} - E^{-3}$
Incoherent scattering	Z	E^{-1}
Pair production	Z^2	ln E

If the energy of the photon is higher than the binding energy of an electron in the atomic shell, the photon can be absorbed and the electron is released (photoelectric effect). The

photoelectric effect is the dominant process for low energies, depending on the material.

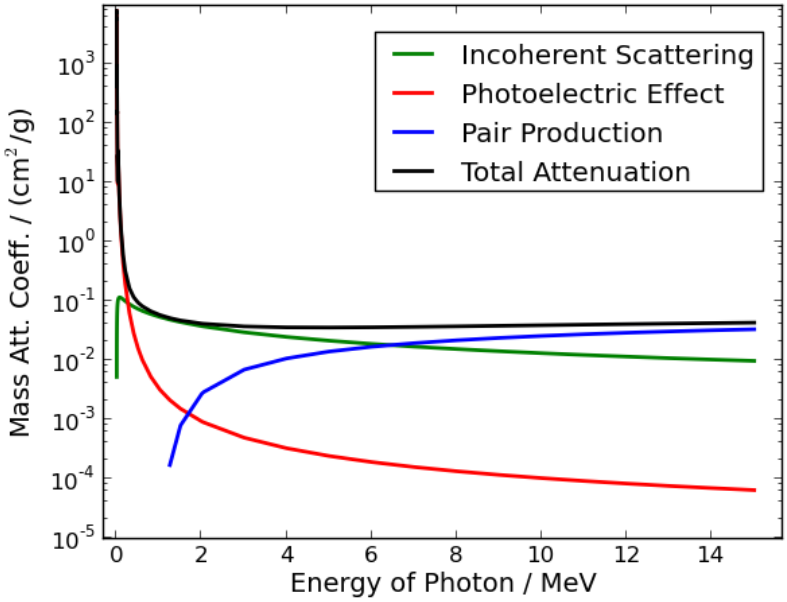

Figure 2.2: Mass attenuation coefficients for photoelectric effect, Compton scattering, pair production, and total attenuation in CZT (Berger et al., 2014).

For photons with an energy of several MeV, the Compton scattering is dominant. For example, for cadmium zinc telluride (CZT), the Compton scattering is the dominating process between 0.3 MeV and 7 MeV, cf. figure 2.2. Incoherent scattering is in the following referred to as Compton scattering: the incident photon is scattered at an electron, which is assumed to be unbound. Using momentum and energy conservation rules the energy of the recoil electron and the scattered photon can be calculated. The Compton scattering is described by equation (2.9). E_0 is the incident energy of the photon, E_1 the energy after the scattering, φ the scattering angle, m_0 the rest mass of an electron, and c the speed of light:

$$\cos(\varphi) = 1 - m_0 c^2 \left(\frac{1}{E_1} - \frac{1}{E_0} \right). \tag{2.9}$$

According to equation (2.9) small scattering angles lead to relatively low energy transfer to the electron. If the photon is scattered backwards, the electron receives the most possible amount of energy. The distribution of the scattering angles depends on the incident energy and can be calculated by the Klein-Nishina formula. From the Klein-Nishina formula it can be deduced that the higher the incident energy, the higher the probability that the scattering angle is small.

The third relevant process is the pair production. A photon is converted into an electron-positron pair. This can happen in the Coulomb field of a nucleus or with minor cross

section in the field of an electron. The latter case is referred to as triplet production, since a considerable amount of energy is transferred to the recoil electron. A precondition for the pair production is that the energy of the incident photon is at least as high as the sum of the masses of electron and positron, i.e. 1022 keV.

Different types of PGI detector systems are used, dependent on the application, in particular, dependent on the energy of the photons. To begin with, the so-called Single-Photon Emission Computed Tomography (SPECT) is well established in nuclear medicine. A radioactive tracer emitting γ-rays is injected to the patient for diagnostic purposes. The detection of the γ-rays is performed with a detector called Gamma or Anger camera. This device is equipped with collimators restricting the direction of the photons to one direction. Due to the high energies of prompt γ-rays produced during therapeutic irradiation compared to nuclear medicine, the application of the conventional Anger camera to the monitoring of particle therapy is not feasible.

A simple but promising approach of PGI for in-vivo dosimetry is based on the slit camera (Smeets et al., 2012; Roellinghoff et al., 2014). The incident photons which pass the slit of a collimator are registered with a scintillator. Another type of PGI-device relies on the Compton effect (Compton camera). If the energy of the incident photon before and after scattering is known, the scattering angle can be deduced, cf. equation (2.9). This camera can consist of one layer for the incoherent scattering (scatter layer) and one detector layer which is dedicated to the absorption of the scattered photon (absorber). With L_1 and L_2 being the energy depositions measured in the scatter and absorber layer, respectively, equation (2.9) is transformed to

$$\cos(\varphi) = 1 - m_0 c^2 \left(\frac{1}{L_2} - \frac{1}{L_1 + L_2} \right). \tag{2.10}$$

A Compton camera with more than one scatter layer is also investigated (e.g. Richard et al., 2011). If in both scatter layers of this Compton camera system a Compton scattering occurs, an arbitrary inelastic interaction, but not necessarily a complete absorption, is required in the absorber layer to provide sufficient information for the derivation of the scattering angle. Evidently, the probability for these interactions in all three layers to occur is lower than one Compton scattering plus an absorption in the corresponding layers if comparable detectors are used.

Knowing the scattering angle, a cone with all possible paths of the incoming photons is derived. By the superposition of the deduced cones for all events the emission distribution is reconstructed. Up to now, no standard reconstruction procedure exists for the Compton camera. Both analytical and algebraic methods, e.g. MLEM are used. One

MLEM approach considers all processes that lead to a measurement as independent from each other (Schöne et al., 2010), i.e., each element of the system matrix results from the multiplication of all transition probabilities. For each event, the corresponding part of the system matrix is precalculated. The acceleration of the reconstruction algorithm, in particular with respect to the calculation and storage of the system matrix, is a major challenge for the Compton camera reconstruction. GPU acceleration is pursued in this context (Dimmrock et al., 2010). Analytic techniques are also followed, dedicated to a specific camera design (Gillam et al., 2008) or studied more generally (Maxim et al., 2009). A comparison between analytical and iterative reconstruction was performed for the same setup with the conclusion that both methods could be feasible (Lojacono et al., 2013).

At OncoRay / HZDR a prototype of a Compton camera is under construction (Kormoll et al., 2011; Kormoll, 2013; Hueso-González et al., 2014). This prototype is intended for in-vivo dose verification of therapeutic irradiation at the proton facility in Dresden. This device consists of one or two pixelated CZT detectors as scatter planes of size ($2 \times 2 \times 0.5$ cm^3) and an LSO detector ($5.2 \times 5.2 \times 2\,cm^3$) that is used as absorber. The spatial resolution of the CZT detector is given by the distance of the readout strips (1.05 mm). The LSO scintillator array consists of separate $4 \times 4\,mm^2$ crystals (Hueso-González et al., 2014). The responding crystal is identified by the light readout scheme. An alternative to the LSO detector is the application of an BGO absorber to reduce the number of random events which occur due to the intrinsic radioactivity of the ^{176}Lu component in the LSO crystals. Experimental results obtained with a point source and, secondly, at a bremsstrahlung beamline with an energy range similar to the γ-ray spectrum during therapeutic irradiation with particle beams are promising (Hueso-González et al., 2014). The achievable spatial resolution of the Compton camera with a CZT scatter layer was already studied and first simulations analyzing the efficiency of this Compton camera system were performed (Kormoll, 2013). The application of two Compton camera arranged in 90 degrees around the Region Of Interest (ROI) is assumed to be reasonable concerning the reconstruction of the image.

Another research group investigates a Compton camera prototype in combination with a beam tagging device (hodoscope) to facilitate reconstruction (Roellinghoff et al., 2011). In other applications of the Compton camera, the incident energy of the photons is known. This applies to the use in homeland security for the detection of radioactive sources. Another example for a known energy is nuclear medicine. A Compton camera system dedicated to SPECT was developed which relies on a gaseous detector enabling the detection of the recoil electrons (Kabuki et al., 2010) in addition to the detection positions in the layers. If the track of the recoil electron is known, the cone containing the feasible

directions of the incident photon is reduced to an arc (Kabuki et al., 2010). The tracking of the trajectories of the recoil electron is not possible for every material and small energies. Another prototype aimed at particle therapy monitoring consist of several thin silicon layers to enable electron tracking (Thirolf et al., 2014). A further approach (Kim et al., 2012) is not based on the detection of the scattered photons but exclusively on the detection of the recoil electrons resulting from incoherent scatterings of the incident photons. Compton cameras have been successfully used for a long time in astronomy. Mounted on a satellite, Compton camera telescopes, e.g. COMPTEL (Schönfelder et al., 1993) performed measurements of extraterrestrial γ-radiation.

Since not every coincident energy deposition in the layers of the Compton camera results from Compton scattering and absorption, respectively, the selection of events is required. The aim is to reject a lot of events which are not valid while keeping most of the valid events. If the energy of the incident photons is known, an energy window can be set around this value. Thus, a lot of invalid events are not considered for reconstruction. In the context of particle therapy, the wide range of energies makes this task difficult. One approach to reduce noise is based on the ratio of the energy depositions in the detector layers. For the Compton camera with the two scatter layers and the hodoscope (Roellinghoff et al., 2011) upper thresholds are introduced for the energy deposition in the scattering layers (Richard et al., 2011). By applying upper limits of 2 MeV, 92 % of the invalid events are rejected and only 5 % of the valid ones. Evidently, these filters depend on the geometry and material of the camera, the shape and position of the source, intrinsic energy thresholds of the detector layers, and, therefore, have to be optimized for another setup. Another filter criteria is based on equation (2.10): since cosine maps real values to [-1,1], the following inequality needs to be fulfilled, otherwise the event associated with L_1 and L_2 cannot result from a valid Compton event (Kormoll, 2013):

$$|1 - m_0c^2 \left(\frac{1}{L_2} - \frac{1}{L_1 + L_2} \right)| \leq 1. \tag{2.11}$$

In astronomy the use of pair production events has a long tradition (Schönfelder, 2004). Pair production cameras are based on the tracking of electron and positron resulting from a pair production. From the paths of electron and positron the direction of the incident photon can be deduced via back projection. For γ-rays of more than 30 MeV a pair production telescope is the device of choice (Schönfelder, 2004), e.g. the *Fermi Gamma-ray Space Telescope* (Michelson et al., 2010). In addition to the use of Compton events, pair production events are also taken into account by the planned space telescope MEGA (Kanbach et al., 2005). Up to now, no pair production camera was applied to the dose verification of particle therapy. It must be stated that the preconditions in astronomy, i.e. high energies, long recording time, and low count rates are not comparable with the

prompt γ-rays emitted during therapeutic irradiation. A simulation study with the focus on achievable angular resolution was performed for the relevant photon energies in particle therapy (Golnik et al., 2011) with the conclusion that the angular resolution of a pair production camera in this energy range is intrinsically bad.

3 Modeling of the production of positron emitters and prompt γ-rays

For the monitoring of particle therapy with PT-PET, the knowledge of the depth-dependent yields of β^+-emitters produced during the irradiation is crucial. In this chapter the abilities of the multi-purpose Monte Carlo simulation codes PHITS and GEANT4, and the one-dimensional deterministic code HIBRAC are compared to each other regarding the reproduction of measured depth-dependent yields of the most abundant positron emitters. Aside from protons, ^{7}Li, ^{3}He, and ^{12}C beams are considered.

PHITS is also evaluated with respect to the prompt γ-rays emitted during irradiation. Since experimental studies in this field are ongoing, reliable simulations of the prompt γ-rays are especially important. The knowledge of the energy spectrum and rate of prompt γ-rays is necessary for the optimization of dedicated PGI-hardware and, moreover, for the development of the convolution algorithm mapping dose to activity and vice versa. The prompt γ-ray emissions simulated with PHITS are compared to experimental data and GEANT4 simulations.

3.1 Particle transport simulation codes

Today, many codes are available for the simulation of the transport of particles through matter. The most frequently applied ones are GEANT4 (Agostinelli et al., 2003), GATE (Jan et al., 2011), FLUKA (Ballarini et al., 2004), SHIELDHIT (Hansen et al., 2012), and PHITS (Sato et al., 2013). All these mentioned simulation tools are Monte Carlo codes. In contrast to this, HIBRAC is a deterministic code and considers only the beam direction, i.e. no lateral movements (Sihver et al., 1996; Sihver and Mancusi, 2009).

PHITS (Particle and Heavy-Ion Transport code System) is chosen in this thesis for the modeling of β^+-emitters since, first of all, PHITS has been applied in various fields of research, e.g. shielding of accelerators (e.g. Sato et al 2005), space radiation dosimetry (e.g. Sihver et al., 2010), and radiotherapy (e.g. Sato et al., 2009). Furthermore, PHITS was applied successfully to the simulation of secondary neutron production during proton irradiation (Schardt et al., 2010b). Simulations of the production of the two most abun-

dant positron emitters ^{11}C and ^{15}O during proton irradiation of a water and a PMMA target have recently been performed with PHITS (Seravalli et al., 2012). In contrast to accurate simulation results obtained with other Monte Carlo codes, PHITS underestimated the production yields (Seravalli et al., 2012). However, in that study only the default parameter settings were used. Concerning the modeling of the production of β^+-emitters resulting from the irradiation of targets with ions different to protons, this is the first analysis with PHITS. Apart from the modeling of the production of β^+-emitters, PHITS is used in this work for the simulation of the photon emissions during proton irradiation. Up to now, no publication describes the use of PHITS for this application.

HIBRAC is a one-dimensional deterministic particle transport code (Sihver et al., 1996, 1998; Sihver and Mancusi, 2009) written in FORTRAN. It was intended and is optimized for the treatment planning of ion beam therapy. Results or parts of the code have been applied for the treatment planning systems in some ion beam facilities, e.g. Institute of Modern Physics, Chinese Academy of Sciences (IMP) in Lanzhou / China, HIMAC in Japan, and at GSI in Darmstadt (Sihver and Mancusi, 2009). The cross section models and the reaction kinematics used in HIBRAC were adopted to the Monte Carlo simulation code providing the distribution of annihilation points for the treatment monitoring at GSI (Hasch, 1996). Since HIBRAC is a compact code which is based on conceptional models, easy to modify, and fast, it is chosen here for the modeling of the β^+-emitter production.

GEANT4 is an open source code and used by a large community (Agostinelli et al., 2003). Since GEANT4 and derivative codes have been widely applied for the simulation of prompt γ-rays as well as for the modeling of the production of β^+-emitting nuclei during the therapeutic irradiation with protons and other light ions, GEANT4 is used in this thesis for an additional comparison. GATE, based on GEANT4, provides a comfortable use and advanced features for the simulation of standard PET cameras and simple readout of secondary isotopes (OpenGATEcollaboration, 2014). With GATE more accurate results are obtained than with PHITS for the production of ^{11}C and ^{15}O during proton irradiation (Seravalli et al., 2012). For carbon and helium beams the yields of β^+-emitting nuclei were simulated with MCHIT (Pshenichnov et al., 2006; 2007), which is also a GEANT4 application. In that work it is concluded that GEANT4 models the β^+-activity with a deviation of 30 to 50 % for energies common to therapeutic irradiation with ion beams. The same order of discrepancy was found by another study benchmarking the positron emitter production rate during carbon ion irradiation against experimental data (Böhlen et al., 2010).

3.1.1 Models in PHITS

PHITS includes several total reaction cross section models, nuclear reaction models, stopping power models, and evaporation models. These models are of relevance for the outcome of the simulation of β^+-emitters produced during the irradiation of a target.

The total reaction cross section, i.e. the probability for an interaction between the beam particle and the atoms of the target, determines the life time of the beam particle, and, therefore, its mean free path. The nuclear reactions resulting in specific types of fragments scale with the total reaction cross section. In PHITS, the total reaction cross section models TRIPATHI (or NASA) (Tripathi et al., 1999) and SHEN (Shen et al., 1989) are available, where the SHEN model is implemented with a slight error (Sihver et al., 2012b). According to a benchmarking with experimental data related to radiation protection in space, the TRIPATHI model is among the best total reaction cross section models (Sihver et al., 2012a).

PHITS 2.30 provides different nuclear reaction models: JAM (Nara et al., 1999), the Quantum Molecular Dynamics model (QMD) (Niita et al., 1995), and three Bertini models. These Bertini models comprise the Free Bertini, the old Cugnon model (Cugnon, 1980), and the new Cugnon model (Cugnon et al., 1981). In order to simulate the statistical decay of excited nuclei, i.e. the emission of light fragments, evaporation models are incorporated in PHITS. In PHITS version 2.30 the Statistical Decay Model (SDM), the Dresner model (DRES) (Dresner, 1963), and, as default, the Generalized Evaporation Model (GEM) (Furihata, 2000) are implemented.

For the simulation of ionization processes of particles in matter the models SPAR (Armstrong and Chandler, 1973) and ATIMA (Geissel and Scheidenberger, 1998; Scheidenberger and Geissel, 1998) are included. SPAR is set as default model. The stopping power model is responsible for the modeling of the energy transfer and, thus, for the range of the particles which is essential for the in-vivo dose verification. As addressed before (Seravalli et al., 2012), the accurate simulation of the stopping power and consequently of the simulated range is a matter of the ionization potential varying between PHITS and other Monte Carlo codes.

Recently, PHITS was optimized regarding the modeling of the γ-decay (Japan Atomic Energy Agency, 2014). The corresponding model in PHITS 2.64 is called ENSDF-Based Isomeric Transition and isomEr production Model (EBITEM) where ENSDF is a public database (National Nuclear Data Center, 2014).

3.1.2 Abilities of HIBRAC

HIBRAC calculates depth dose, dose average LET, energy straggling, and momentum loss of ions traveling through matter (Sihver et al., 1996; Sihver and Mancusi, 2009). It is based on semi-empirical total cross section and fragmentation cross section formulas for proton-nucleus and nucleus-nucleus reactions (Sihver and Mancusi, 2009). HIBRAC calculates projectile fragments up to the mass number $A_{\text{projectile}}$ - 1, where the cross sections of fragmentation reactions are deduced by scaling the corresponding proton-nucleus fragmentation cross sections (Tsao et al., 1993; Sihver et al., 1993; Sihver and Mancusi, 2009). These proton-nucleus reference cross sections are derived from a validated semi-empirical code for the production of target fragments during proton irradiation and are considered in terms of reversed kinematics as projectile fragmentation cross sections of an ion beam hitting a hydrogen target. The reference data are scaled by using the weak factorization property of projectile fragmentation (Olson et al., 1983). The scaling parameter is of Bradt-Peters type (Sihver and Mancusi, 2009). As shown by experiments, the weak factorization property is not feasible for the use of a hydrogen target as a basis (La Tessa et al., 2007). Therefore, further corrections are applied in HIBRAC.

The contributions of two generations of projectile fragments are considered, whose remaining energy is calculated by means of empirical approximations (Tsao et al., 1995). HIBRAC returns the fluence of projectile fragments summarized for each atomic number $Z = 1,..., Z_{\text{projectile}}$. For carbon beams in the relevant energy range the total and likewise the partial charge changing cross sections for particles with $Z = Z_{\text{projectile}} - 3,..., Z_{\text{projectile}} - 1$ agree quite well with experiments (Toshito et al., 2007). However, due to a lack of experimental data regarding the production of fragments with an atomic number of one or two, the potential inaccuracy of HIBRAC is remarked (Sihver et al., 1998). In the current HIBRAC version target fragments are not calculated (Sihver and Mancusi, 2009).

3.2 The production of β^+-emitting nuclei during particle irradiation

The positron emitter production is studied for protons, ^{12}C, ^{3}He, and ^{7}Li ions as projectiles. The beam energies and the target material are chosen according to available experimental data. With PHITS, GEANT4, and HIBRAC the depth-dependent yields per incident particle (IP) of ^{11}C, ^{15}O, ^{10}C, and ^{13}N, which are the most abundant β^+-emitters during therapeutic irradiation of human tissue, are simulated. Accurate simulations of ^{11}C are most important for off-line PET or in-room PET since after the irradiation the vast majority of β^+-emitters with half-lives shorter than the half-life of ^{11}C ($T_{\frac{1}{2}} = 20$ min) have

already decayed.

3.2.1 Experimental data

Depth-dependent yields of β^+-emitting nuclei deduced from experimental data are used for a comparison with the simulated yields. The corresponding measurements were conducted at GSI with a PET camera during and directly after the irradiation with proton beams (Parodi et al., 2002), ^{3}He beams (Fiedler et al., 2006), ^{7}Li beams (Priegnitz et al., 2008), and ^{12}C beams (Priegnitz, 2012). The number of the specific nuclides were derived by means of a fitting procedure (Parodi et al., 2002; Priegnitz et al., 2012). These experimental yields were used earlier for a comparison with GEANT4 simulations (Pschenichnov et al, 2007; Priegnitz, 2012), SHIELDHIT simulations (Fiedler, 2008), and POSGEN simulations (Priegnitz, 2012).

3.2.2 PHITS simulations

PHITS version 2.30 is applied. To guarantee that the beam is stopped the size of the target is set to $10 \times 10 \times 40\,\mathrm{cm}^3$ with the beam in *z*-direction. The obtained depth-dependent yields are histogrammed in bins of 1 mm size. The number of incident particles is set to 10^7 for proton beams and to 10^6 for ^{12}C, ^{3}He, and ^{7}Li beams. The type of the output file and the parameters are specified in way that PHITS provides the number of the relevant nuclides as a function of the depth where they stop. Both available total cross section models SHEN and TRIPATHI, are tested. Concerning the nuclear reaction model, QMD, JAM, and the three Bertini models are applied. Additionally, the available evaporation models as well as the two stopping power models ATIMA and SPAR are tested.

3.2.3 HIBRAC simulations

To start HIBRAC, only the energy, the mass number, and the atomic number of the projectile and the specification of the target material are required. Since HIBRAC calculates the transport of particles in direction of the beam and neglects lateral movements, neither target geometry, nor beam expansion need to be defined. Since the original HIBRAC version (Sihver and Mancusi, 2009) cannot be used directly for the simulation of specific positron emitters produced during particle irradiation several changes to the code are necessary.

First of all, in contrast to the original HIBRAC version, each projectile fragment that is of interest is saved individually. In the original version projectile fragments are grouped according to their atomic numbers. Furthermore, instead of the fluence of the projectile fragments, the positions, where the projectile fragments are stopped are calculated. That

means, when a fragmentation process takes place, the range of this particle is calculated and the yield for the corresponding bin is updated. Since HIBRAC uses different bin sizes over the range of the particles, changes of the bin size between the bin of production and the bin that is finally reached by this particle are taken into account.

Another modification of the HIBRAC code is the incorporation of the target fragmentation. The modified code provides the relevant fragments depending on the projectile and the composition of the material. The target fragmentation itself is calculated by exchanging the involved projectile and target nuclei. It is assumed that the energy transfer between projectile and target fragment is zero, and, consequently, the movement of the target fragments is not considered. The following types of fragments are calculated:

- First generation of projectile fragments;
- First generation of target fragments;
- Second generation of projectile fragments, i.e. fragments of projectile fragments;
- Second generation of target fragments, i.e. target fragments originating from a hit of a primary projectile fragment with the target.

In the original HIBRAC implementation quadrium ions (^{4}H) appear unintentionally as projectile fragments and are followed by secondary target fragments induced by interactions of the ^{4}H ions with the target material. Due to the short half-life of quadrium ($T_{\frac{1}{2}} < 10^{-21}$s), the production of this isotope is discarded.

3.2.4 GEANT4 simulations

In this thesis the focus is put on the analysis of PHITS and HIBRAC. GEANT4, which has been approved for this application, is used for an additional comparison. Therefore, the simulations with GEANT4, version 9.3 are restricted to the recommended models and parameter settings of the GATE-collaboration (OpenGATEcollaboration, 2014) for particle therapy. For carbon ion beams the nuclear reaction QMD is recommended over the Intra-Nuclear Cascade model (INC) which is consistent with a previous simulation study of the production of β^+-emitters (Böhlen et al., 2010). For lithium and helium beams both models are tested. For the GEANT4 simulations the same target dimensions, number of beam particles, and the same bin size for the yields is used as for PHITS. For the recent simulation study of the positron-emitter production during proton therapy (Seravalli et al., 2012) the GEANT4 application GATE, version 6.1 (Jan et al., 2011) was applied. Here, GEANT4 is used, since GATE turned out not to be suitable for ^{3}He beams due to the missing implementation of the necessary class *IonInelastic* for ^{3}He in GATE 6.1.

3.2.5 Results

In figure 3.1 the depth-dependent yields of ^{15}O during the irradiation of a PMMA target with ^{12}C ions obtained with PHITS using the different nuclear reaction models, total cross section models, stopping power models, and evaporation models are depicted. Visible differences can be observed for the different nuclear reaction models. The total cross section models SHEN and TRIPATHI on the other hand lead to the same production rate. Between the range obtained with the stopping power models SPAR and ATIMA, no difference is evident for this example and agrees with the experimentally found peak. However, the calculation of the range depends on the applied ionization potential where different values are used for PMMA in the Monte Carlo codes PHITS and GATE (Seravalli et al., 2012). Remarkably, the choice of the evaporation model is important. Considerable deviations in the yields obtained with different evaporation models can be observed with PHITS. The impact of these evaporation models is independent of the combination of the nuclear reaction model with an evaporation model. Surprisingly, the PHITS simulation without the use of any evaporation model leads to the best agreement with the experimental data for this example.

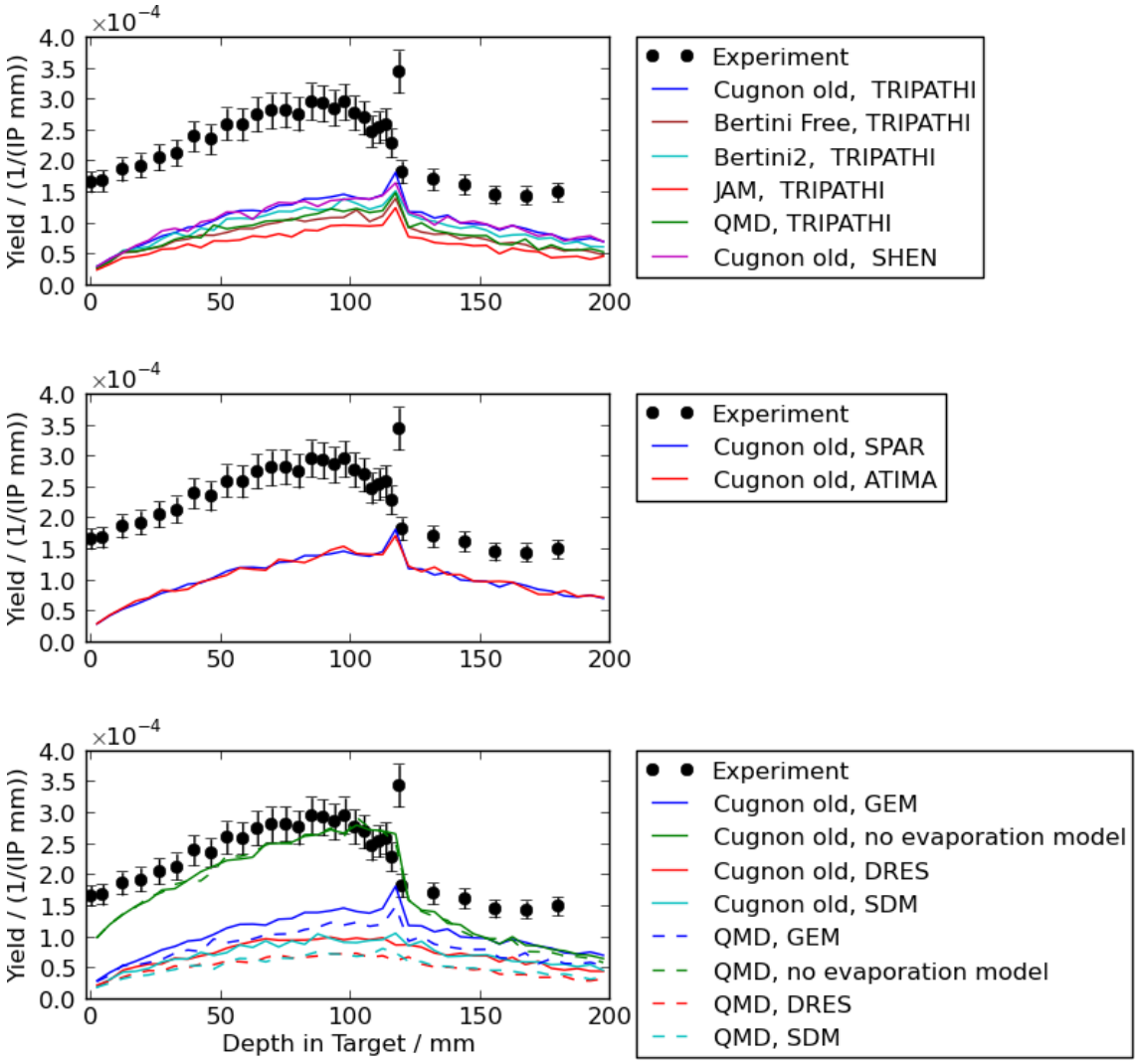

Figure 3.1: Depth-dependent yields of ^{15}O during the irradiation of a PMMA target with ^{12}C ions of 266 *A*MeV simulated with PHITS using different nuclear reaction and total cross section models (top), different stopping power models (center), and different evaporation models (bottom) in comparison to experimental data (Priegnitz et al., 2012).

Figure 3.2 depicts the cross sections for $^{12}C(p, pn)^{11}C$ and $^{16}O(p, pn)^{15}O$ reactions used in HIBRAC in comparison with published experimental data (National Nuclear Data Center, 2013). A good agreement between these experimental and the measured values is found, except for the cross section of reaction $^{16}O(p, pn)^{15}O$ in the energy range 40 to 60 MeV which is overestimated by HIBRAC.

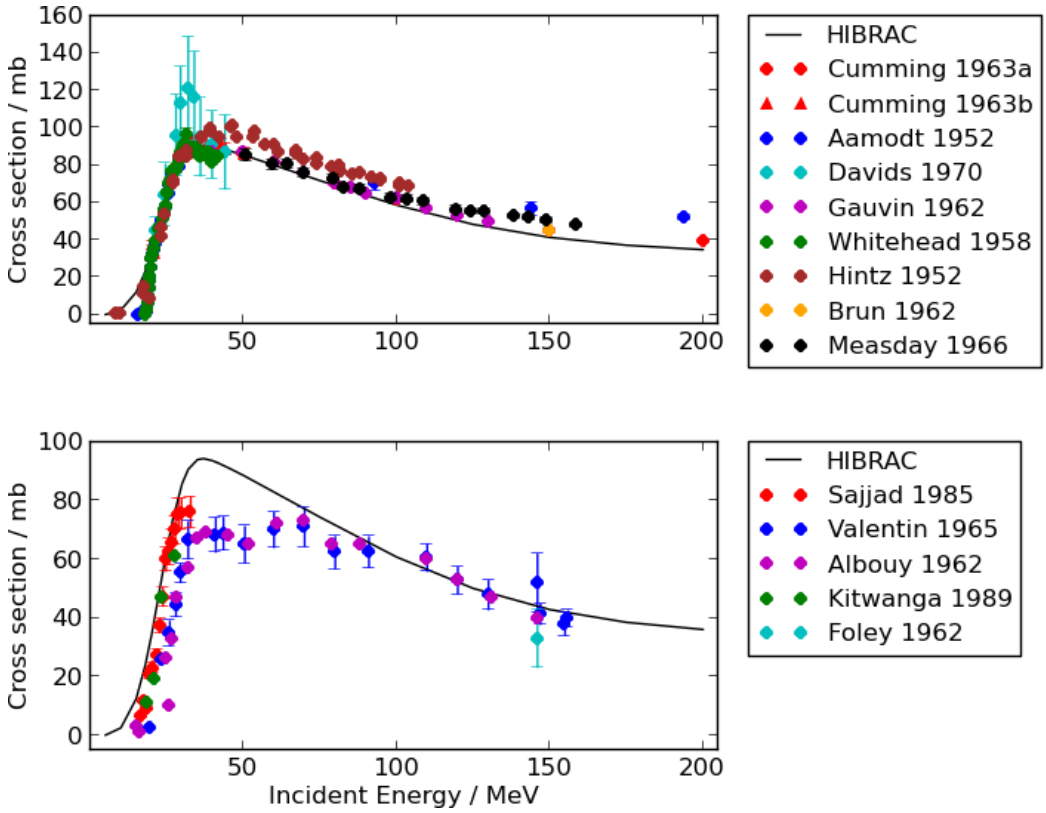

Figure 3.2: Comparison between the fragmentation reaction cross sections included in HIBRAC and experimental cross sections (National Nuclear Data Center, 2013) for the reactions $^{12}C(p, pn)^{11}C$ (top) and $^{16}O(p, pn)^{15}O$ (bottom).

Figure 3.3 shows the ^{11}C yields produced during carbon irradiation of a PMMA target as simulated with HIBRAC together with experimental data. The yields originating from the first and second projectile and target fragmentations are plotted individually. The peak resulting from projectile fragmentation is well reproduced. On the other hand, the plateau, which originates from target fragments is underestimated. It should be mentioned that HIBRAC simulates a small rate of secondary projectile fragments of ^{11}C for ^{12}C projectiles. This can be explained by the fact that ^{12}N can result from a charge-changing reaction of the incident projectile followed by a fragmentation reaction with ^{11}C as projectile fragment. The charge-changing reaction of ^{12}C to ^{12}N can be confirmed by published experimental data concerning the nuclear reactions $^{12}C(p, n)^{12}N$ (National Nuclear Data Center, 2014).

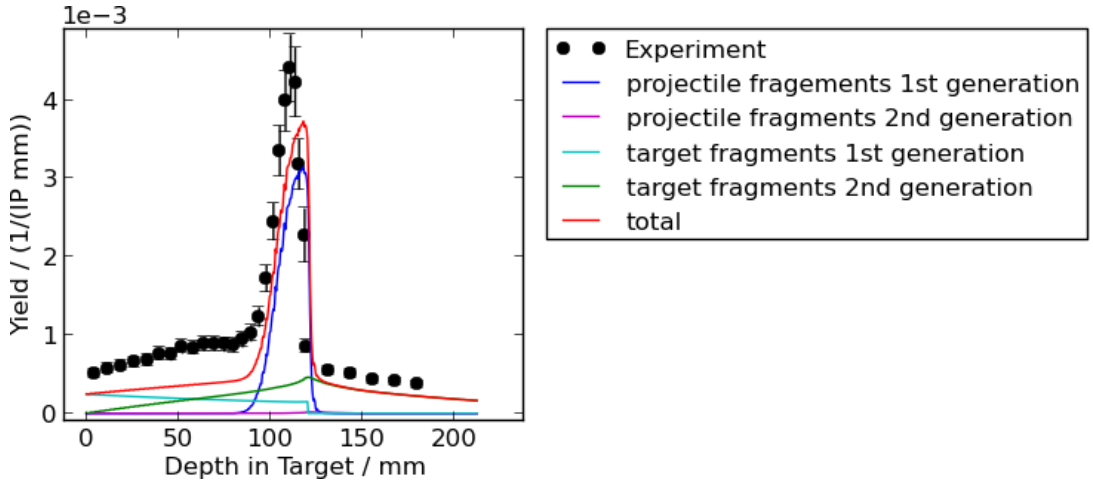

Figure 3.3: Depth-dependent yields of ^{11}C during the irradiation of a PMMA target with ^{12}C ions of 266 *A*MeV simulated with HIBRAC and compared to experimental data (Priegnitz et al., 2012).

The figures 3.4, 3.5, and 3.6 show depth-dependent yields of β^+-emitters for proton, ^{3}He, ^{7}Li, and ^{12}C beams, respectively, which are simulated with GEANT4, PHITS, and HIBRAC, and compared to measured data. For PHITS the default parameter settings are used. For the proton irradiation an accurate reproduction of the ^{11}C and ^{15}O yields is obtained with GEANT4 and HIBRAC, cf. figure 3.4. The deviation at the end of the range between the experimental data and the HIBRAC and GEANT4 results is probably due to the spatial resolution of the PET scanner used for the experiments. In contrast to GEANT4 and HIBRAC, PHITS generally underestimates the production rates of the considered β^+-emitters. For the production of ^{11}C yields during ^{3}He and ^{7}Li irradiation, the HIBRAC and PHITS results are considerable less accurate than the yields obtained with GEANT4, cf. figure 3.5. Regarding the ^{11}C yields during the irradiation of the water target with ^{12}C ions, cf. figure 3.6, the projectile fragments are most accurately reproduced with HIBRAC and the target fragments with GEANT4.

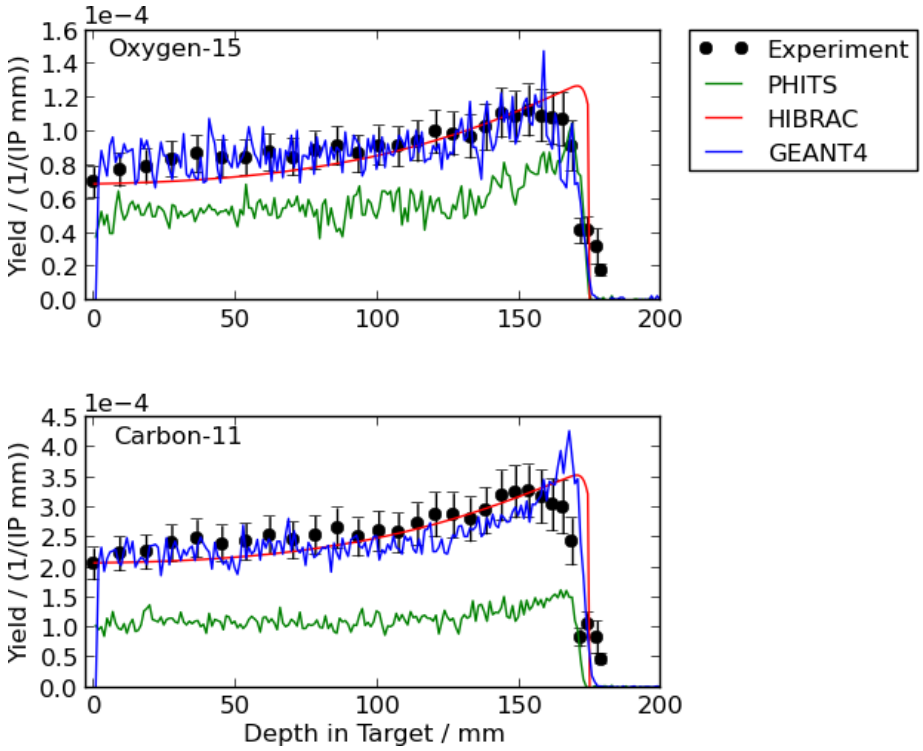

Figure 3.4: Depth-dependent yields of ^{15}O and ^{11}C during the irradiation of a PMMA target with protons of 175 MeV. The yields obtained with the simulation codes PHITS, HIBRAC, and GEANT4 are compared to experimental data (Parodi et al., 2002).

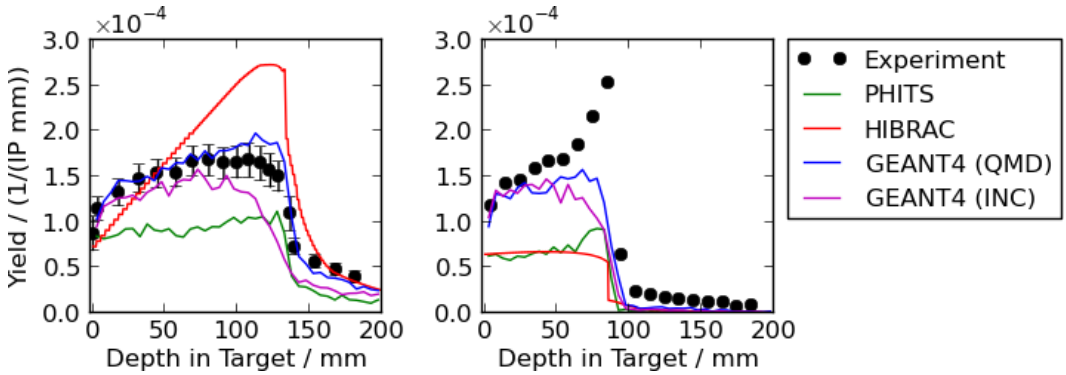

Figure 3.5: Depth-dependent yields of ^{11}C during the irradiation of a water target with ^{7}Li ions of 162 *A*MeV (left) and ^{3}He ions of 130.3 *A*MeV (right). The yields obtained with the simulation codes PHITS, HIBRAC, and GEANT4 are compared to experimental data (Fiedler et al., 2006; Priegnitz et al., 2008).

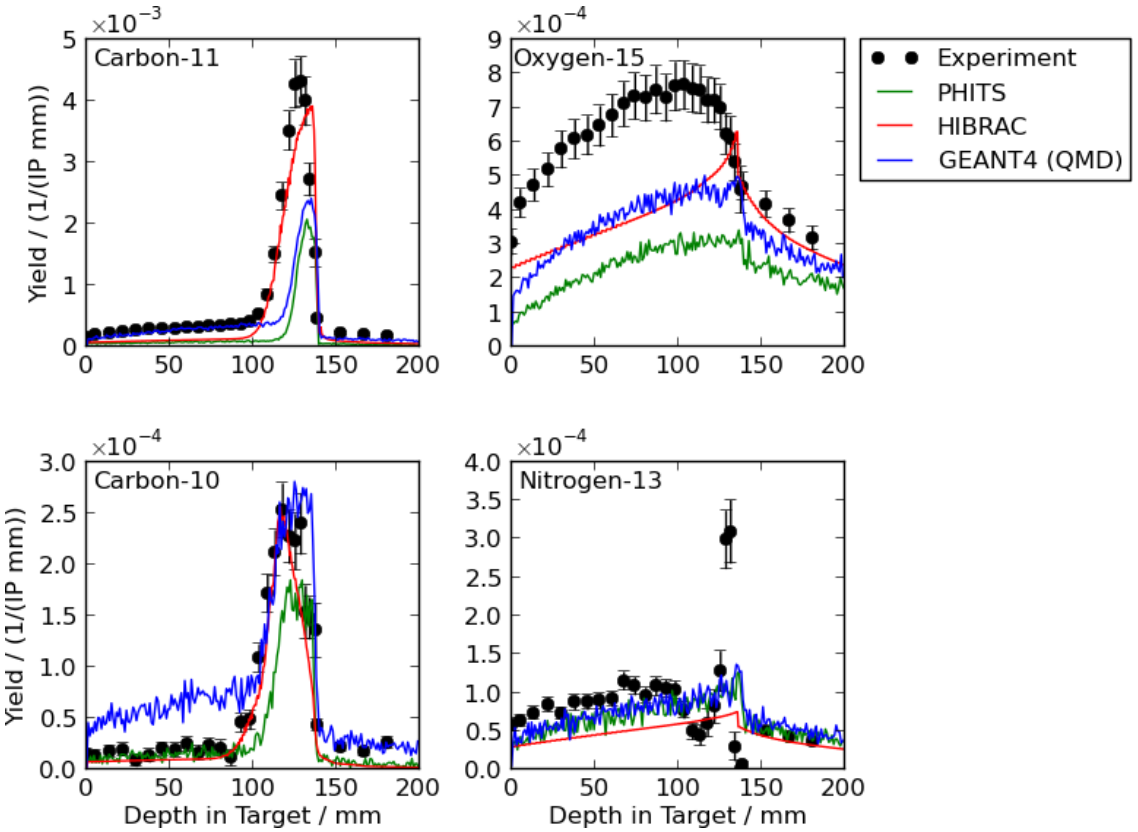

Figure 3.6: Depth-dependent yields of ^{11}C (top, left), ^{15}O (top, right), ^{10}C (bottom, left), and ^{13}N (bottom, right) during the irradiation of a water target with ^{12}C ions of 266 *A*MeV. The yields obtained with the simulation codes PHITS, HIBRAC, and GEANT4 are compared to experimental data (Priegnitz et al., 2012).

Figure 3.7 shows the deviations from the experimental data for the production of ^{11}C for the three different simulation codes. The deviations from the experimental data regarding the total amount and each sampling point of the depth-dependent yields of ^{11}C are given. The PHITS simulations are obtained with the default settings. For the GEANT4 simulations the INC is used for proton beams and the QMD for the other three types of ions. According to these results, GEANT4 shows considerably better agreement with the experiments than PHITS. Moreover, the comparability of HIBRAC with GEANT4 simulations for proton beams is confirmed.

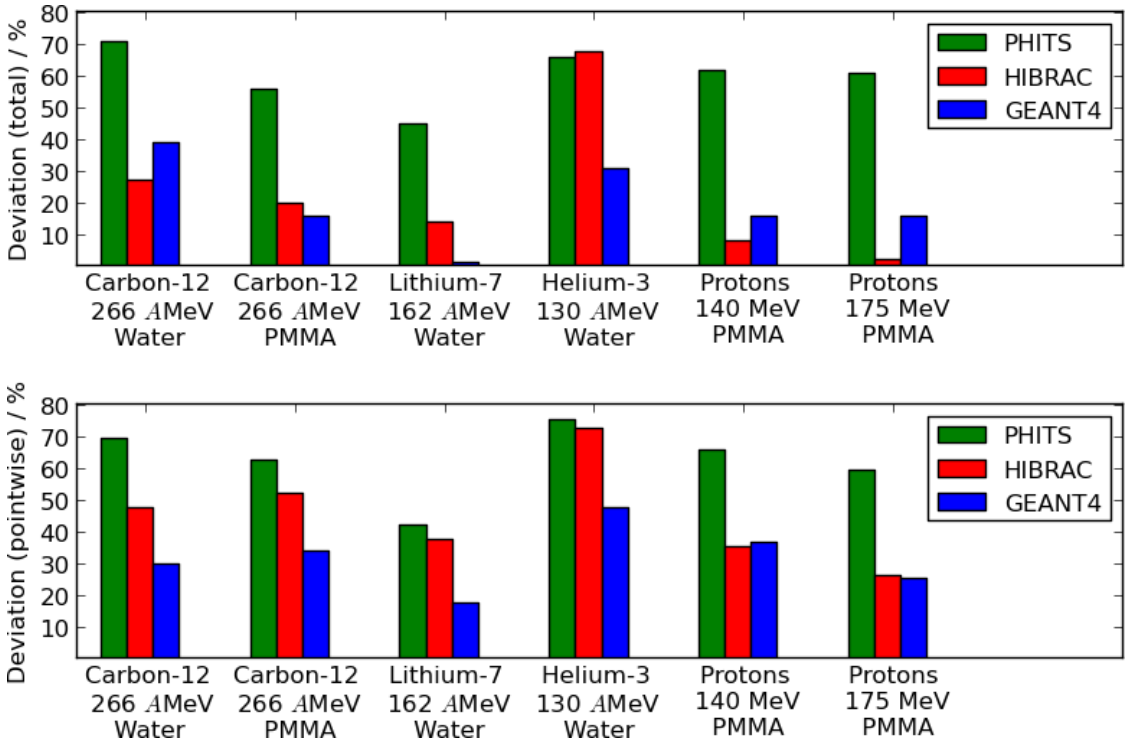

Figure 3.7: Evaluation of PHITS, HIBRAC, and GEANT4 simulations: deviation from the measured total yield (top) and mean pointwise deviation from the measured depth-dependent yields (bottom) of ^{11}C produced during the irradiation with ^{12}C, ^{7}Li, ^{3}He, and proton beams.

For the applicability of a simulation code to PT-PET, its runtime is crucial. Thus, HIBRAC, GEANT4 version 9.5, and PHITS version 2.30 are tested regarding their time consumption on the same personal computer. Exemplarily, the calculation of the production of the positron-emitters ^{13}N, ^{11}C, ^{10}C, and ^{15}O during the irradiation with protons of 175 MeV of a PMMA target is chosen. None of the codes is executed in parallel mode. For PHITS and GEANT4 10^7 incident particles are used, to achieve sufficient data, cf. figure 3.4. Between HIBRAC and the two Monte Carlo tools, the runtime differs by a factor of 30 and 50, respectively, cf. table 3.1.

Table 3.1: Comparison of the runtime required to simulate the depth-dependent yields of ^{13}N, ^{11}C, ^{10}C, and ^{15}O during the irradiation of a PMMA target with protons of 175 MeV.

HIBRAC	GEANT4	PHITS
0.13 h	3.65 h	6.42 h

3.3 Simulation of the prompt γ-ray emissions with PHITS

The abilities of PHITS version 2.64 using the EBITEM model are tested with respect to the modeling of prompt γ-ray emissions. For this purpose, energy-spectra of γ-ray emissions during proton irradiation are simulated with PHITS by adopting an experimental setup. Within the corresponding experimental study at Kernfysisch Versneller Instituut (KVI) in Groningen, the Netherlands, a proton pencil beam with 150 MeV was directed on a PMMA target ($10 \times 10 \times 15\,\mathrm{cm}^3$). During the irradiation the γ-rays emitted from the target were detected with a germanium detector placed perpendicularly to the beam direction. These experiments were conducted by other members of OncoRay and HZDR. The PHITS simulations cover all photons escaping the target and, secondly, the energy deposition in the detector. Beside the comparison to the preliminary experimental data obtained at KVI, the results achieved with PHITS are also compared to GEANT4 simulation results.

In the simulation study with PHITS all photons crossing the surface of the PMMA target are stored. Figure 3.8 shows the obtained energy spectrum in comparison to GEANT4 simulation results, which are provided by Andreas Schumann (OncoRay / HZDR). In general, a good agreement between the positions of the peaks in the two spectra up to an energy of 7 MeV can be observed. Remarkably, the spectrum obtained with PHITS does not show the peaks at 511 keV and 2.2 MeV which should be prominent. The peak at 511 keV is associated with the annihilation photons and the one at 2.2 MeV with the neutron capture in hydrogen. In contrast to PHITS, GEANT4 does not calculate the Doppler-broadening accurately. Due to the Doppler broadening, lines of a photon spectrum corre-

sponding to nuclear reactions should actually appear broadened. For example, the peak at 4.4 MeV is partially broadened but is narrowed erroneously to a line in the spectrum obtained with GEANT4. The apparent discrepancies in the rate of prompt γ-rays with energies higher than 7 MeV between PHITS and GEANT4 require a detailed study of the underlying models which are responsible for the modeling of γ-rays in that energy region.

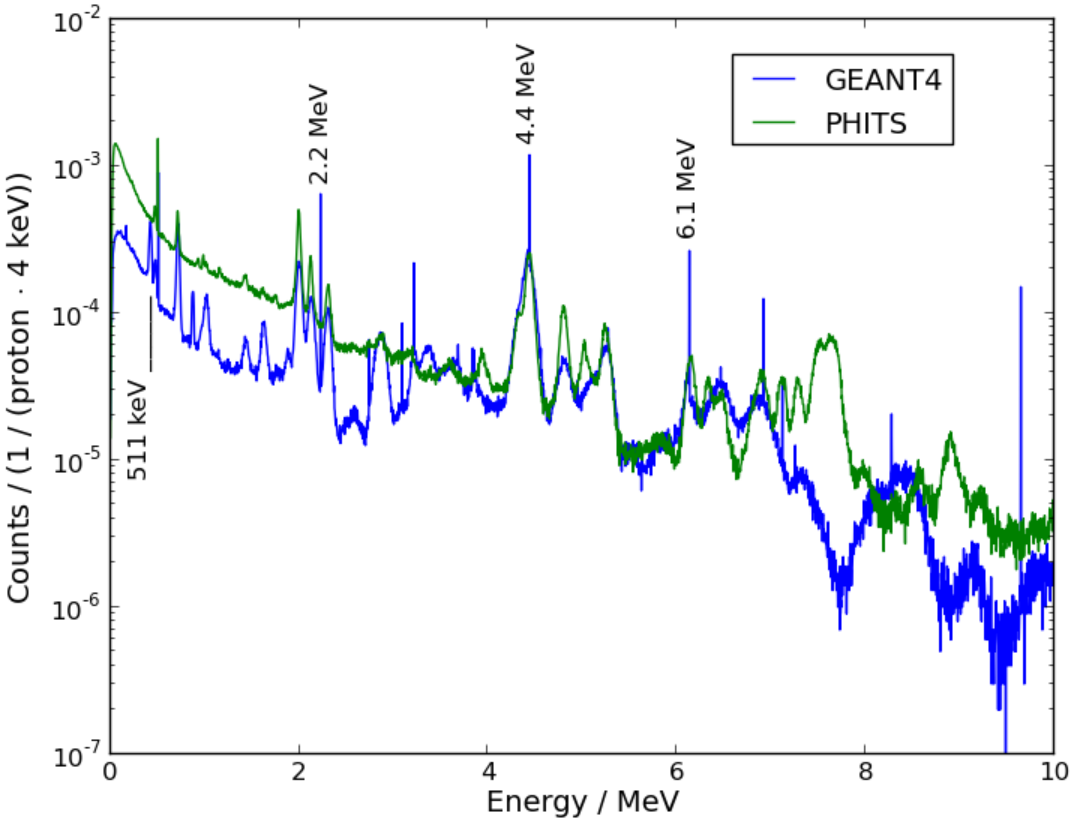

Figure 3.8: Prompt γ-ray emissions during proton irradiation of a PMMA target. The PHITS and GEANT4 simulations are performed with 10^7 protons and all γ-rays escaping the target are shown in bins of 4 keV. The GEANT4 simulation results are provided by Andreas Schumann (OncoRay / HZDR).

Secondly, in order to provide a quantitative comparison between PHITS simulations and experimental data, the energy deposition in the germanium detector is calculated with PHITS. For this reason, the position and the geometry of the germanium detector is modeled with PHITS according to the experimental setup. The hereby obtained simulated energy depositions are depicted in the histogram in figure 3.9 in comparison to GEANT4 results and preliminary measured data. The experimental data as well as these GEANT4 simulations are also shared by Andreas Schumann (OncoRay / HZDR). With PHITS, the

energy depositions in the germanium detector are overestimated by 50 %. The values obtained with PHITS are even higher than with GEANT4, except for the energy range from 3 to 6 MeV for which comparable yields have been simulated with GEANT4 and PHITS. Fortunately, photons in this energy range are most relevant for the application of a Compton camera.

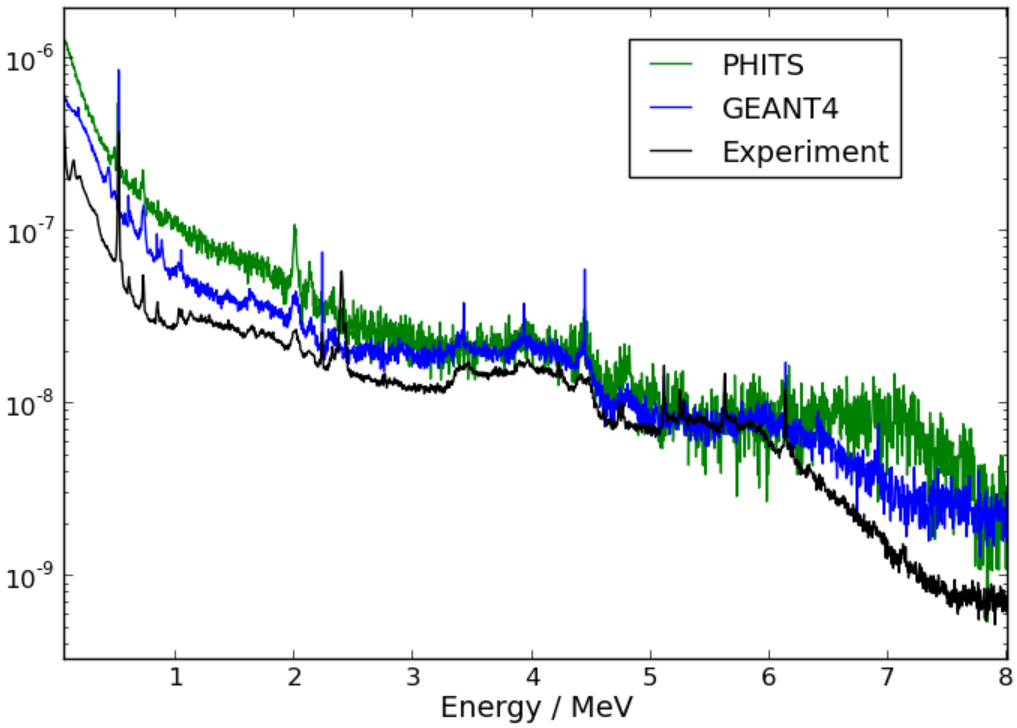

Figure 3.9: Energy deposition in the germanium detector during proton irradiation of a PMMA target as calculated with PHITS in comparison to GEANT4 results and preliminary measurements performed at KVI. The GEANT4 simulation results as well as the experimental data set are provided by Andreas Schumann (OncoRay / HZDR).

4 GEANT4 simulations for the optimization of a Compton camera prototype

Particle therapy monitoring by means of a Compton camera is an approach that is pursued intensively at OncoRay in collaboration with the HZDR. At the moment, a Compton camera prototype is being developed (Kormoll et al. 2011; Kormoll, 2013; Hueso-González et al., 2014) with the intention to install it at the new proton facility in Dresden for in-vivo dose verification of patient treatment. To achieve this goal, substantial optimization work is ongoing, concerning the detector design, the readout electronics, and the reconstruction algorithm.

Monte Carlo simulations essentially support this project. Simulations allow for a systematic investigation of the influence of parameters like the geometrical setup, the detector material, and the energy of the incident photons on the detection efficiency of the camera. Another major reason for the use of advanced simulation tools, as e.g. the Monte Carlo code GEANT4, is the possibility to track each particle and all processes taking place along its way through matter. This also includes particles of further generations. Therefore, these simulations provide more insight into the interactions than can be obtained by experiments. For example, the deviation originating from the use of the positions of detection instead of the points of scattering and absorption is studied. Furthermore, the number of possible processes which occur in a Compton camera is too high to estimate the rates of the different sequences of interactions analytically, i.e. by means of known cross sections, without applying simplifications (Kormoll, 2013). Thus, another aim of the simulations in this context is the classification of the occurring coincident energy depositions into valid Compton events and invalid events which cannot be used for a reconstruction. For instance, if a photon is scattered more than once in the scatter plane, the scatter angle is not reconstructed correctly and this event is not a valid Compton event in the sense of imaging. A further task is the evaluation and establishment of filtering mechanisms improving the rate of valid Compton events, i.e. to reduce background due to invalid events at the expense of valid events. Recommendations for suitable criteria for the rejection of events are developed using simulation results. Furthermore, the impact of the energy resolutions of the detector layers on the angular resolution can be analyzed for the actual distribution of scattering angles can very easily by means of simulations.

In addition to this, the possibility of extending the Compton camera to make use electron-positron pairs following a pair production is evaluated. This is conducted with respect to the number of detected pair production events and the achievable angular resolution of the back projected photon direction.

The Monte Carlo simulations in this chapter are intended to model reality as accurate as possible. This concerns the detector design, the photon source, the energy of the γ-rays, and the modeling of detector response. To verify the simulations, simulated data are compared to available experimental results.

Modeling of photon processes with GEANT4

The simulations are performed with the Monte Carlo code GEANT4 version 9.5. GEANT4 is a widely used toolkit for the simulation of particles traversing matter (Agostinelli et al., 2003). Physical processes can be included in the simulation by declaring them in so-called *physics lists*. The physics list *QGSP_BIC* provided by GEANT4 was chosen. Thereby, the possible interactions of a photon and secondary particles traversing various materials can be modelled. In order to simulate the processes that are important for this application as exactly as possible, the standard models included by QGSP_BIC for photoelectric effect, Compton scattering, pair production, as well as ionization and bremsstrahlung induced by electrons are replaced with the corresponding *Livermore low-energy electromagnetic models*, which model photon processes down to 250 eV (Incerti, 2014):

- *G4LivermorePolarizedPhotoElectricModel*,
- *G4LivermorePolarizedComptonModel*,
- *G4LivermorePolarizedGammaConversionModel*,
- *G4LivermoreIonisationModel*, and the
- *G4LivermoreBremsstrahlungModel*.

The *G4LivermorePolarizedComptonModel* takes into account the Doppler-broadening for Compton scatterings. Validations of the photon interaction models implemented in GEANT4 against reference libraries were performed proving a good agreement between all considered cross section libraries and the implemented models of the three photon processes that are relevant regarding this application, i.e. photoelectric effect, pair production, and Compton scattering (Cirrone et al., 2010).

4.1 Simulation of Compton events

4.1.1 Considered sources and setups

Since the detector response of the Compton camera is sensitive to the direction of the incident photons, the dimension of the source and the distance between the source and the camera are of importance. Two shapes of sources are used for the simulation study. The first source is a point source and the second one a spherical source with 10 cm diameter, which roughly approximates one irradiation field in cancer therapy. In the following, these two sources are situated in a straight line in front of the Compton camera leaving 10 cm of air between the source and the camera by default. With respect to the intended application to in-vivo dosimetry, a distance of at least 10 cm between the Compton camera and the origin of the prompt γ-rays is required. The simulated sources emitted prompt γ-rays isotropically. Different energies of the γ-ray sources are chosen in the relevant energy range between 0.5 and 10 MeV. Thereby, energy dependency of the detector response is studied. To model γ-ray emissions with energies similar to those occurring during a patient irradiation, the spectrum shown in figure 2.1 is also used as input. The spherical source with the γ-ray emissions from this simulated spectrum is referred to as *patient source* in the following.

In this thesis different configurations of a Compton camera prototype are considered with the focus on the detector materials cadmium zinc telluride (CZT), lutetium oxyorthosilicate (LSO), and BGO. Material and dimensions of the detector layers are in line with available detectors at OncoRay / HZDR. Two types of setups are considered: *scatter-absorber* systems and *scatter-scatter* systems, following the terminology of the recent design study of these prototypes (Kormoll, 2013). The former consists of two layers, one dedicated to incoherent photon scattering and the measurement of the energy deposition of the recoil electron and the second detector plane is dedicated to the absorption of the scattered photon. The latter is built from three layers, where two of them are destined for scattering. Three *scatter-absorber* camera configuration are used for the simulations, cf. table 4.1. For the first configuration two CZT-detectors are simulated, one as scatter and one as absorber layer with 4 cm in-between (center to center). Each CZT detector has a size of $2 \times 2 \times 0.5\,\mathrm{cm}^3$. The other two designs also consist of a scatter layer made from CZT but have LSO or BGO, respectively, as absorber with the dimension $5.2 \times 5.2 \times 2\,\mathrm{cm}^3$. The absorber is placed 8 cm behind the scatter layer in one line (center to center). All designs are aligned in *z*-direction, cf. figure 4.1.

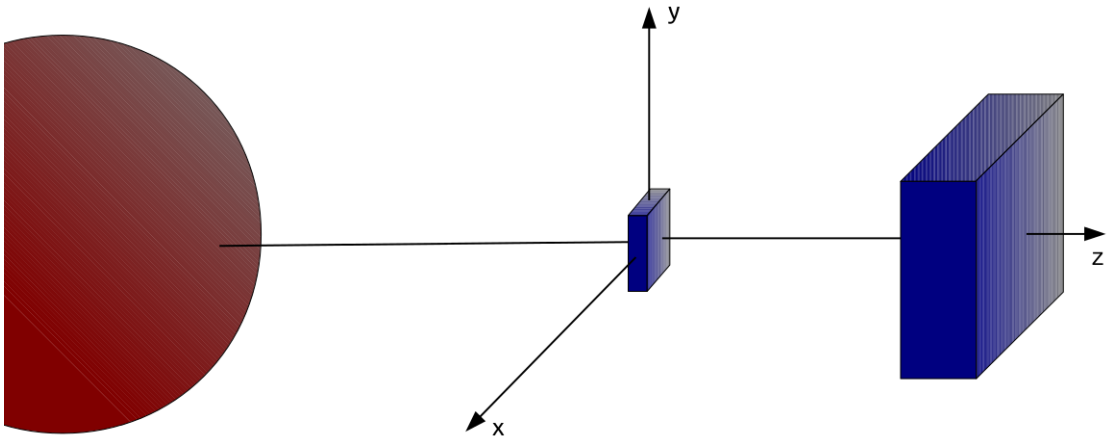

Figure 4.1: Setup of the considered CZT-LSO or the CZT-BGO Compton camera with the spherical source.

Table 4.1: Properties of the *scatter-absorber* systems under study.

Detector	Scatter layer	Absorber layer	Distance
CZT-CZT	CZT: $20 \times 20 \times 5\,\mathrm{mm}^3$	CZT: $20 \times 20 \times 5\,\mathrm{mm}^3$	40 mm
CZT-LSO	CZT: $20 \times 20 \times 5\,\mathrm{mm}^3$	LSO: $52 \times 52 \times 20\,\mathrm{mm}^3$	80 mm
CZT-BGO	CZT: $20 \times 20 \times 5\,\mathrm{mm}^3$	BGO: $52 \times 52 \times 20\,\mathrm{mm}^3$	80 mm

The *scatter-scatter* system considered is illustrated in figure 4.2. Two CZT-detectors ($2 \times 2 \times 0.5\,\mathrm{cm}^3$) are used as scatter layers and three BGO detectors ($5.2 \times 5.2 \times 2\,\mathrm{cm}^3$) form the absorber. The distances are 4 cm between the CZT detectors and 8.5 cm between the second CZT detector and the central BGO detector. This detector arrangement is referred to as CZT-CZT-BGO and is based on an experimental setup.

4.1.2 Modeling of the detector response

In reality, every charged particle can induce a signal in a detector layer of the Compton camera. From an arbitrary registered energy deposition it cannot be concluded which kind of process has taken place. Consequently, in this simulation study an *event* is defined as a coincident energy deposition in at least two detector layers, regardless of the type and origin of the inducing particles. Events in a *scatter-absorber* system consist of energy depositions in both detectors and are therefore called *scatter-absorber* events. Concerning the *scatter-scatter* system, coincident energy depositions in all three layers are referred to as *scatter-scatter* events. If only in two of the three layers of a *scatter-scatter* detector system an interaction is registered, this event is considered also as a *scatter-absorber* event, with the scattering assumed in the layer closest to the source. The time resolution of the setup under consideration does not permit the measurement

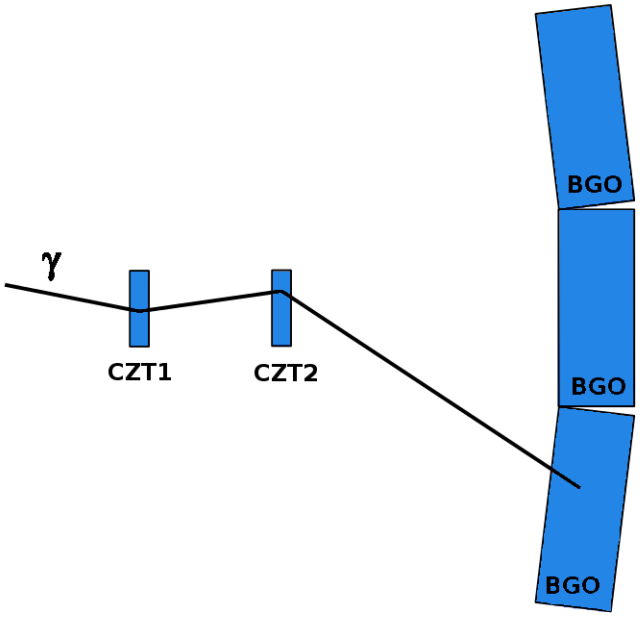

Figure 4.2: Setup of the CZT-CZT-BGO camera with two Compton scatterings and the absorption of the incident photon.

of the time difference between the interactions of a photon in different layers. Therefore, an event can result from any order of interactions, i.e., backscattered events are not excluded.

For the simulation of events, realistic lower energy thresholds are considered dependent on the detector material. For CZT and BGO thresholds of 100 keV and for LSO 50 keV are used as default values. Energy resolution is taken into account by blurring the exact energy depositions according to table 4.2: Gaussian distributions of the energy resolutions are assumed with a standard deviation being a function of the exact deposited energy. The energy resolutions for LSO and BGO are derived by measurements performed by Christian Golnik, Fernando Hueso-González, Thomas Kormoll (OncoRay / TU Dresden), and Katja Römer (HZDR).

Next, it has to be determined how to simulate the detection positions in each of the detector layers. Possibly, several particles deposit energy at different locations until they are stopped or escape from a detector layer. If for example a Compton scattering occurs, the resulting recoil electron deposits energy by multiple scatterings. For the simulation, the center of gravity, i.e. the mean of all energy-weighted locations of energy deposition, is considered as the detection position. This assumption agrees with the measuring points in reality.

Evidently, the idealized character of simulations has to be taken into account. In particular, the following aspects need to be mentioned. First, each emitted photon is tracked individually by the performed GEANT4 simulations. This is in contrast to experimental measurements, since measurements can contain false coincidences, i.e., two particles of independent origin interact simultaneously and are registered as one event. Furthermore, it can occur that an event does not trigger a measurement due to the dead time of the detector. Additionally, the use of LSO is accompanied by another difficulty: this material is intrinsically radioactive. This is not a negligible reason for false coincidences and, therefore, background. Moreover, since this simulation study is not focused on the readout electronics, neither the trigger regime, nor electrical fields in the detector are taken into account. Furthermore, inhomogeneities of the detector material are not considered.

Table 4.2: Energy resolution of the detectors under consideration as a function of the deposited energy L. The energy resolution for CZT was used before (Kormoll et al., 2011) and the energy resolutions of the LSO and the BGO detector are derived by measurements; courtesy of Christian Golnik, Fernando Hueso-González, Thomas Kormoll (OncoRay / TU Dresden), and Katja Römer (HZDR).

Detector	Energy resolution / FWHM
CZT	$6\,\text{keV} + 0.15\,\text{keV}\,\sqrt{L\,/\,\text{keV}}$
LSO	$\left(\frac{11.912}{\sqrt{0.001\,L\,/\,\text{keV}}} + 1.365\right) L \cdot 10^{-2}$
BGO	$9.6\,\text{keV} + 3.43\,\text{keV}\,\sqrt{L\,/\,\text{keV}}$

4.1.3 Classification of events and filter criteria

A *scatter-absorber* event is considered as *valid Compton event* if exactly one Compton scattering takes place in the scatter layer followed by the complete absorption of the scattered photon in the absorber layer, no secondary particle escapes from the detector layer it is produced in, and no interaction of the incident photon in the air takes place. *Scatter-scatter* events are considered as *valid* if the photon undergoes exactly one Compton scattering inside the two scatter layers and an arbitrary inelastic interaction in the absorber in the correct order, without escape of secondary particles from the first two layers or interactions in the air. For *scatter-scatter* events this definition of valid Compton events equals the one in a previous publication (Richard et al., 2011). Concerning the simulation study analyzing the feasibility of a Compton camera with CZT as scatter layer (Kormoll, 2013), this approach is an extension, because in that study the movement of secondary particles has been neglected, i.e., it is assumed that they always stop inside the detector

layer they originate from.

It is studied whether it is possible to select events according to certain characteristics with the aim to reject a large number of invalid events while keeping the majority of the valid Compton events. In the following, various approaches dedicated to a possible reduction of background are discussed. In case of a known photon source, all events with a measured energy deposition outside a narrow interval containing the initial energy can be discarded. For the wide energy spectrum of incident photons present during therapeutic irradiation with particle beams, a selection of events is more difficult and advanced filter criteria need to be established.

The following filter criteria are considered for a *scatter-absorber* system using the available data, i.e. the energy deposition in the scatter layer (L_1), the energy deposition in the absorber layer (L_2), and the depth-of-interaction in the scatter layer:

Condition 1 $L_1 + L_2 \leq T$: the first idea is to apply an upper energy threshold for the total energy deposition $L_1 + L_2$. Since for photons with an energy larger than 7 MeV the pair production is the dominant process in CZT (Berger et al., 2014), 7 MeV could be used as upper threshold if a CZT detector is considered as scatter layer.

Condition 2 $|1 - m_0c^2 \left(\frac{1}{L_2} - \frac{1}{L_1+L_2}\right)| \leq 1$ is a necessary condition for an event to be valid, due to equation (2.10) and the cosine function mapping into the interval $[-1, 1]$. All other events with energy depositions L_1 and L_2 cannot originate from a valid Compton event and should not be considered for reconstruction (Kormoll, 2013). If the position of the source is known, the range of feasible scattering angles can be used as an even more restrictive condition regarding feasible values of $|1 - m_0c^2 \left(\frac{1}{L_2} - \frac{1}{L_1+L_2}\right)|$.

Condition 3 $L_1 \neq 511$ keV and $L_2 \neq 511$ keV: if the simulated energy deposition in one detector layer equals 0.511 MeV, this event is almost surely invalid. The reason is that this energy deposition results most likely from an annihilation photon. Therefore, a simple method to reduce background is to reject all events with an energy deposition of 0.511 MeV in one of the layers. Obviously, the energy resolution has to be taken into account to define an appropriate energy window.

Condition 4 According to the ratio between L_1 and L_2: in a recent publication dealing with a *scatter-scatter* Compton camera (Richard et al., 2011) the distribution of energy depositions in the two scatter layers of a Compton camera was studied for valid and invalid Compton events. Upper thresholds for the

energy deposition in both scatter layers result from this analysis. Here, this strategy is adopted for the *scatter-absorber* detector.

Condition 5 Threshold for the depth-of-interaction in the scatter layer: Secondary charged particles, e.g. electrons following Compton scatterings, photoelectrons and electrons and positrons following a pair production, deposit energy along their way out. Therefore, the escape of charged particles and their interactions in the absorber are more probable for detection positions in the last part of the scatter layer. Using this criterion, events with a detection position deeper than a certain threshold are discarded.

Condition 6 $L_1 + L_2 = E_{\text{Peak}}$: this idea is based on the prominent lines in the assumed spectrum of emitted photons during irradiation. If the sum of the energy depositions equals the energy of a peak (E_{Peak}), the probability that the measured energy is the incident energy of the photon is high. This is just due to the fact that a high percentage of γ-rays are emitted with energy E_{Peak}. If there is no escape of energy from the Compton camera, the probability is high that such an event is a valid Compton event. Evidently, in practice the question is whether there is an adequate number of photons emitted with E_{Peak} and registered with a total measured energy deposition in an energy window around E_{Peak}.

4.1.4 Results

Influence of energy resolution on uncertainty of the scattering angle

Since the scattering angle φ is deduced from the measured energy depositions L_1 and L_2, cf. equation (2.10), the energy resolution influences the precision of the calculated scattering angle and, therefore, the quality of the reconstructed image. One possibility to analyze the influence of the energy resolution is the application of the standard error propagation (Kormoll et al., 2011)

$$(d\varphi)^2 = T_1^2 \left(\frac{dL_1}{L_1}\right)^2 + T_2^2 \left(\frac{dL_2}{L_2}\right)^2 \tag{4.1}$$

where T_1 and T_2 are dependent on the scattering angle φ, L_1, and L_2. The uncertainty of the exact scattering angle φ ($d\varphi$) is given as a function of φ (Kormoll et al., 2011).

In contrast to this previous study (Kormoll et al., 2011), in this work, the influence of the energy distribution on the angular uncertainty is studied for the specific setups CZT-LSO and CZT-BGO and the actual distributions of scattering angles using the *patient source*.

Thus, explicit values of the average deviation from the correct angle induced by the energy resolution are obtained for the existing hardware systems and a realistic distribution of incident photons. In order to neglect further uncertainties, only valid Compton events are considered for this analysis.

In figure 4.3 the influence of the energy resolution on the calculated scattering angle is quantified for the CZT-LSO setup and the *patient source*. The deviation between exact and blurred scattering angle is derived by calculating the scattering angle first with the values of the simulated energy depositions, and secondly with the energy depositions blurred according to the energy resolutions of CZT and LSO. The first (top left) image depicts the mean deviations between exact and blurred scattering angle. The results for CZT given as a function of the true scattering angle are comparable with the already published results (Kormoll et al., 2011). However, the actual distribution of scattering angles, which is depicted in the lower left image in figure 4.3, needs to be considered in order to provide a quantification of this uncertainty. Therefore, the deviations from the true scattering angle are also depicted (bottom right) after the normalization according to the distribution of scattering angles, which is shown in the lower right image of figure 4.3. Since scattering angles larger than 40 degrees are rare, the deviations arising from these events do not have much influence on the mean deviation. The deviation resulting from the energy blurring in the CZT is the same for both setups, the CZT-LSO and the CZT-BGO, on average 0.08 degrees. It is obvious, that the energy resolution of the absorber has more impact on the angular resolution than the energy blurring of the CZT detector. For the CZT-LSO setup the mean deviation is 0.74 degrees for the LSO, and, if the CZT-BGO setup is used, a deviation of 0.88 degrees resulting from the energy resolution of the BGO detector has to be expected. Hence, the improvement of the energy resolution of the absorber is more important than to achieve a better energy resolution of the scatter layer.

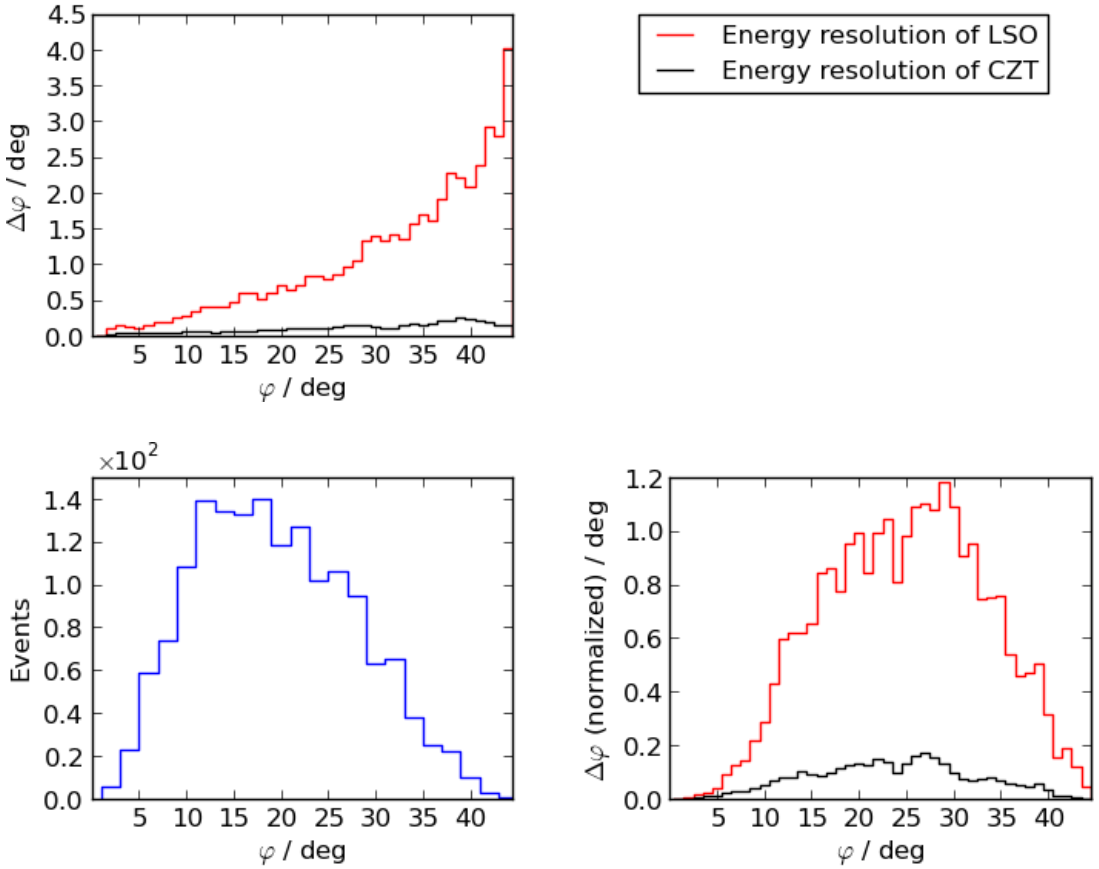

Figure 4.3: Uncertainty of the calculated scattering angle caused by the energy resolution of each of the detector layers (CZT and LSO). The upper left image depicts the average deviation for each scattering angle. The lower right image shows the normalized deviation from the exact scattering angle for the actual distribution of scattering angles, which is shown in the lower left figure. The *patient source* is used. The influence of the energy resolution of the CZT detector on the uncertainty of the calculated scattering angle is depicted in black and for the LSO detector in red. Only valid Compton events are considered.

Modeling of the spatial uncertainty induced by the detection positions

The measured interaction points in the detection layers do not agree with the actual positions of the desired photon processes, i.e. Compton scattering and absorption, respectively, but with the centers of gravity of all energy depositions in the corresponding layer. The impact of this fact on the spatial uncertainty with respect to the reconstructed track of the photon is quantified in the following for the *scatter-absorber* setup CZT-LSO. After a Compton scattering has taken place, energy is deposited by the Compton electron and possibly by bremsstrahlung induced by the decelerating Compton electron. For this reason, the relevant deviation in the scatter layer corresponds to the distance between the center of gravity and the position of the Compton scattering. Regarding the absorber, the relevant processes are pair production, photoelectric effect, and Compton scattering, where only the two former result in an absorption of the incident photon. The secondary particles resulting from these processes and, potentially, from a precedent Compton scattering, ionize the atoms of the detector. Therefore, in the case of the absorber, the relevant deviation corresponds to the shortest distance between the center of gravity and the straight line that is defined by the direction and entering position of the photon incident on the absorber. Furthermore, the influence of Compton scattering in the absorber on this deviation is studied. In the GEANT4 simulations performed to evaluate this uncertainty, exclusively valid Compton events are taken into account in order to avoid further inaccuracies.

The results of this simulation are shown in figure 4.4. As expected, the deviation between the center of gravity and the point of the incoherent scattering in the CZT increases with the energy of the incident photon due to the length of the mean free path of the Compton electron, and reaches circa 0.5 mm for a photon of 10 MeV incident energy. For a point source the deviation is slightly smaller than for the spherical source because large scatter angles in the CZT come along with high energy transfer to the recoil electron. The spatial deviation arising from th use of the center of gravity of all interactions in the absorber is about 1 mm, cf. figure 4.4. This deviation is depicted for all valid Compton events and for those valid Compton events without an incoherent scattering in the absorber. For photons with an energy below 5 MeV, Compton scatterings in the absorber have considerable influence on this spatial uncertainty.

From this study it can be concluded, that the error caused by the use of the center of gravities should be taken into account, in addition to the intrinsic spatial resolutions of the detector layers, when analyzing the angular resolution of the camera.

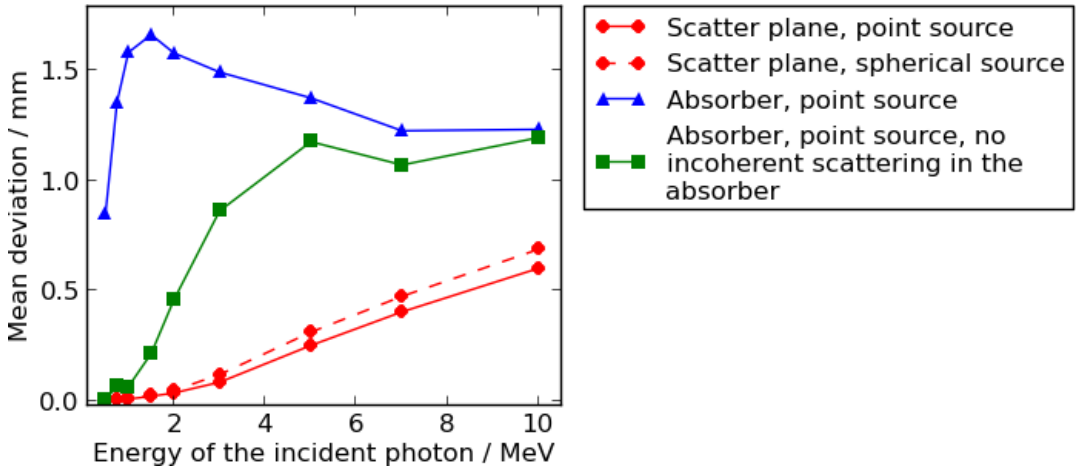

Figure 4.4: Uncertainty arising from the use of the center of gravity in the scatter layer and absorber layer, respectively. The CZT-LSO detector system is used.

Detection probabilities

The simulated detection probabilities are shown in figure 4.5 for different setups and various energies of the incident photons. The detection probabilities for the CZT-LSO setup are higher than for the CZT-CZT due to differences in the dimensions of the detectors and the attenuation properties of the detector material. The detection probabilities increase with the energy. This can be explained by the energy dependence of the cross sections of the different photon interactions and the energy-dependent mean free paths of secondary particles, in particular electrons. When the spherical source is used instead of the point source, about 50 % less events are obtained. The reason for this observation is that the probability for a photon to induce an event in the detector is dependent on its distance and alignment to the detector, especially regarding the range of possible scattering angles. For the CZT-BGO system the same detection probabilities are obtained as for the CZT-LSO camera. To estimate the number of events achievable in reality, the *patient source* is applied in these simulations. Per γ-ray emission $3.3 \cdot 10^{-6}$ events are registered with the CZT-CZT setup and $1.2 \cdot 10^{-5}$ in the CZT-LSO setup with the camera systems placed in 10 cm distance in front of the source. Figure 4.6 shows the detection probabilities for the *scatter-absorber* events and the *scatter-scatter* events registered with the CZT-CZT-BGO system. The number of events corresponding to energy depositions in both CZT detectors is lower for this setup than for the CZT-CZT camera, since all events with energy depositions in both CZT layers and one of the three BGO detectors are not considered as *scatter-absorber* events.

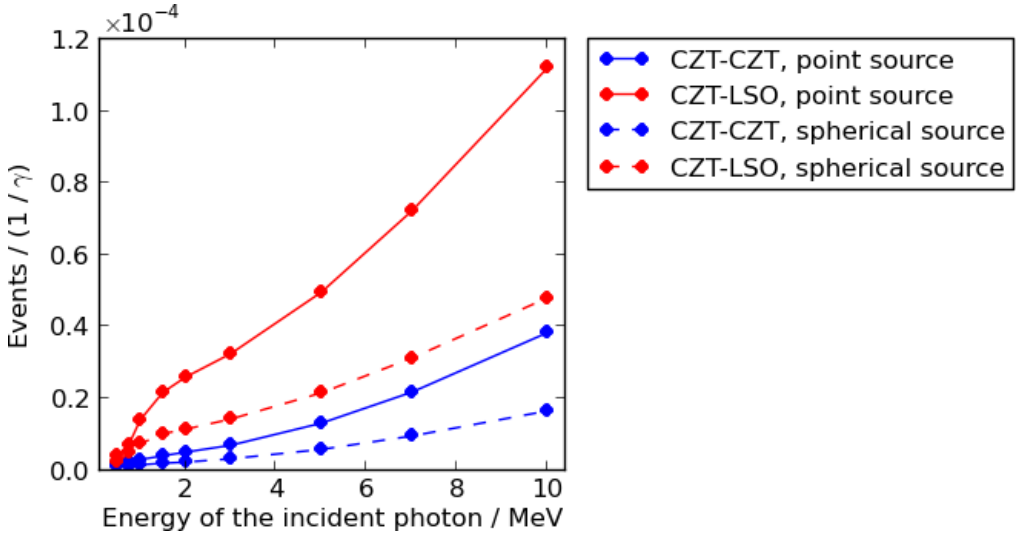

Figure 4.5: Detection probabilities for two *scatter-absorber* Compton camera configurations and two differently shaped sources per isotropically emitted photon.

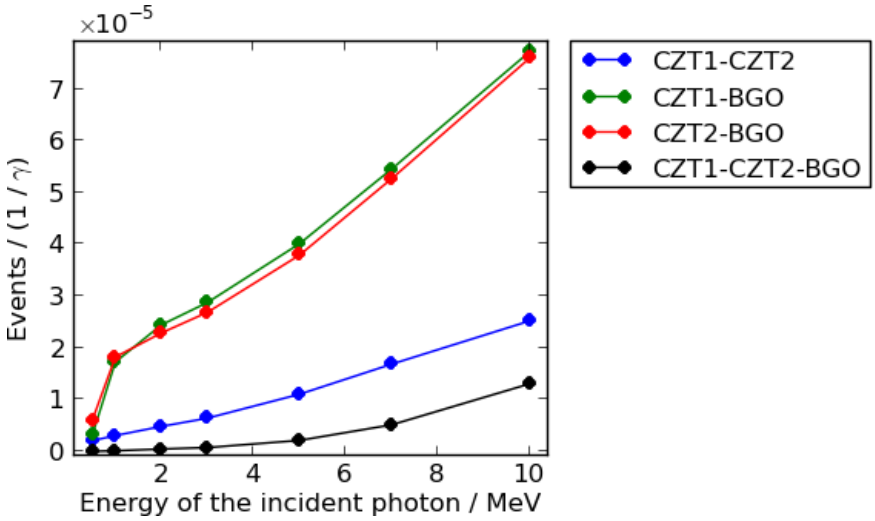

Figure 4.6: Number of *scatter-scatter* events and the three types of *scatter-absorber* events registered with the CZT-CZT-BGO camera system, cf. figure 4.2, per isotropically emitted photon. A point source is used.

Percentage of valid Compton events

Figure 4.7 shows the percentage of valid Compton events for the three *scatter-absorber* setups and the CZT-CZT-BGO setup for different energies of the incident photons. As a result it can be stated that the CZT-LSO and the CZT-BGO setup provide a higher percentage of valid events than the CZT-CZT camera. With the BGO absorber, a slightly higher percentage of valid events than with LSO is obtained, cf. figure 4.7. Differences in the cross sections of the photon processes (Berger et al., 2014) in BGO and LSO result in a less rate of backscattering and escape from the absorber.

Regarding the CZT-CZT-BGO setup, the percentage of valid *scatter-scatter* Compton events is higher than the rates of *scatter-absorber* events for incident energies up to 3 MeV and lower for photons with an energy above 3 MeV. The former fact can be explained by the allowed escape of energy from the absorber and the latter from the rate of secondary interaction products (i.e. photons, electrons, and positrons) escaping from a scatter layer and interacting in the absorber which increase with the energy. In every case the percentage of valid Compton events is maximal, if the incident photon has an energy of about 1 MeV. For the *patient source* the obtained percentage of valid events is 10.9 % and 1.5 % for the CZT-LSO and the CZT-CZT setup, respectively.

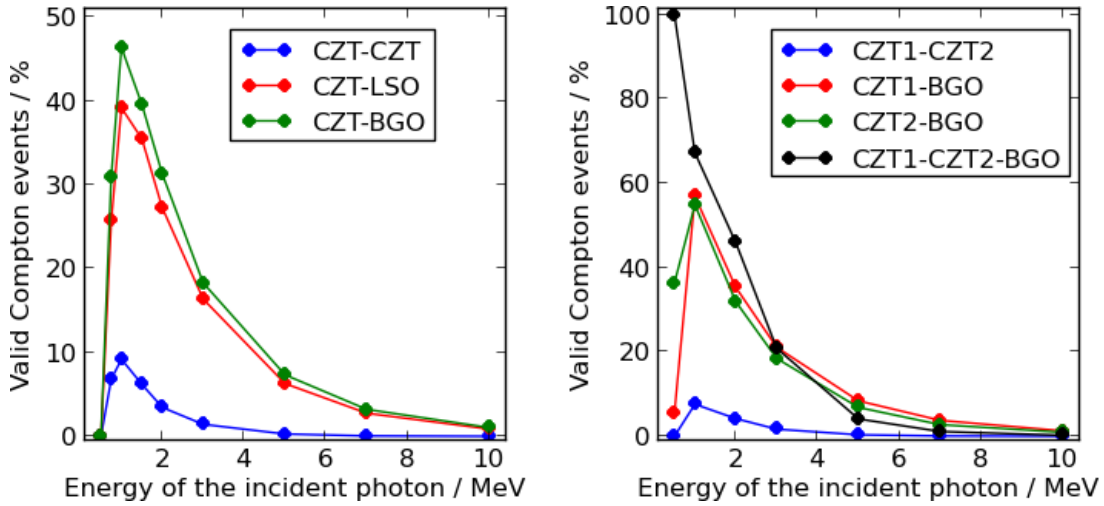

Figure 4.7: Percentage of valid Compton events (in terms of all events) for the three *scatter-absorber* Compton cameras under consideration (left) and the CZT-CZT-BGO setup, cf. 4.2 (right). The point source is used.

The main reasons for the appearance of invalid *scatter-absorber* events are

1. Backscattering: the photon traverses the scatter layer without any interaction, interacts in the absorber and the scattered photon itself or secondary particles deposit finally energy in the scatter layer;

2. Pair production in the scatter layer: a pair production in the scatter layer takes place, and secondary particles, i.e. electron, positron or annihilation photons, leave the scatter layer and deposit energy in the absorber;

3. Multiple Compton scattering: after more than one Compton scatterings in the scatter layer the scattered photon interacts in the absorber;

4. Escape from the scatter layer: after a Compton scattering the recoil electron or bremsstrahlung induced by the recoil electron escape from the scatter layer;

5. Escape from the absorber layer: a Compton scattering in the scatter layer takes place, the scattered photon interacts in the absorber, but the primary photon or secondary particles escape from the absorber.

For *scatter-scatter* systems the criteria listed above are applicable analogously with one exception: a *scatter-scatter* event can be valid if there is energy escape from the absorber.

In figure 4.8 the rates of the main types of invalid events are depicted for the CZT-LSO Compton camera. Evidently, these rates are strongly dependent on the energy of the incident γ-rays.

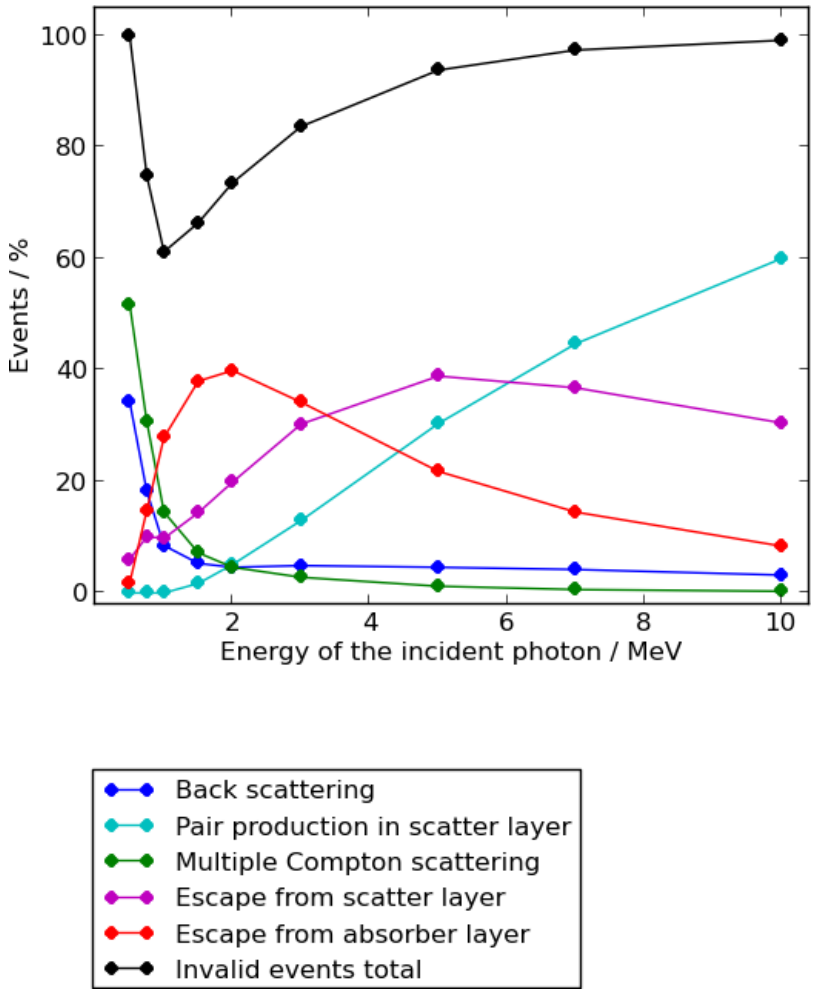

Figure 4.8: Main types of invalid events (in terms of all events) for the CZT-LSO setup used with the point source. The rate is given as a function of the energy of the incident photon.

Backscattering decreases distinctly between 0.5 and 1 MeV. This phenomenon can be explained by the energy thresholds which lead to the neglect of a lot of valid events with an energy deposition in the scatter layer lower than the energy threshold. In contrast to

this, many of the photons with initial energies of 0.5 MeV or below that are scattered backwards from the absorber layer and are absorbed at last in the scatter layer where they deposit sufficient energy to be registered. The rate of pair productions in the scatter layer resulting in events increase with the energy because of the cross section for pair production and the energy-dependent mean range of the electron and positron resulting from a pair production. Escape of secondary particles following a Compton scattering in the scatter plane causes a large number of invalid events. Most of these events result from an interaction of these secondaries in the absorber material and no photon interaction takes place in the absorber. Predominantly, these particles are the recoil electron and bremsstrahlung photons induced by radiation stopping of the recoil electron. Figure 4.9 shows the energy distribution of the Compton electrons escaping the scatter layer. If a Compton electron escapes from the CZT, on average about half of the initial energy of the γ-ray is transported out of this detector. Furthermore, the angle between the direction of the escaping Compton electrons and the *z*-direction (orientation of the camera) is depicted in figure 4.9: a large amount of Compton electrons move with a small angle regarding the *z*-direction and, therefore, hit the absorber.

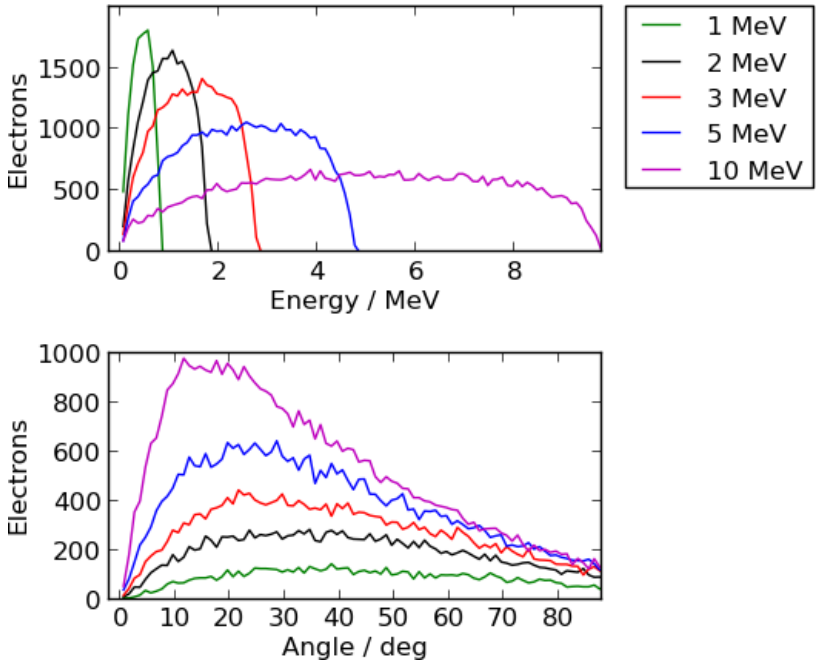

Figure 4.9: Recoil electrons resulting from a Compton scattering which escape from the CZT-detector: energy distribution (top) and angle with respect to the orientation of the camera (bottom). A point source with 10^9 isotropic photon emissions with various energies is simulated. The bin sizes are 0.1 MeV and 1 degree, respectively.

Escape from the absorber reaches a maximum at 2 MeV, cf. figure 4.8. The decrease for photon energies above 2 MeV is due to the increasing number of invalid events resulting from secondary particles which escape from the scatter layer and the increasing rate of pair production events.

Table 4.3 lists the simulated rates of the different types of invalid events for the *patient source*. Just as observed for the monoenergetic photons, most invalid events result from pair production in the scatter layer, escape of secondary particles from the scatter layer or escape from the absorber. Beside the already discussed types of invalid events, events originating from photoelectrons escaping from the scatter layer and their absorption in the absorber layer and interactions of the photon in the air are studied for the *patient source*. The rate of events originating from a photoelectric effect in the scatter layer and an escaping photoelectron is 0.5 %. The rate of events which would be valid Compton events if the corresponding photons had not interacted with the atoms of the air is 0.02 % and is, therefore, negligible.

Table 4.3: Number of events, percentage of valid Compton events, and percentages of the different types of invalid events for the *patient source* used with the CZT-LSO setup.

Events / $(1/\gamma)$	$1.2 \cdot 10^{-5}$
Valid events	10.9 %
Backscattering	7.7 %
Pair production in scatter layer	28.3 %
Escape from scatter layer	29.8 %
Multiple Compton scattering	3.7 %
Escape from absorber	21.7 %
Photoelectric effect in scatter layer	0.5 %
Interaction in air	0.02 %

Event selection

The high rate of invalid events leads to the question whether the mentioned filter criteria (*Condition 1 - 6*, cf. section 4.1.3) could enhance the percentage of valid Compton events. The outcome of each strategy is discussed for the *patient source* and the CZT-LSO Compton camera system. Results are summarized in table 4.4 giving on the one hand the percentage of falsely discarded valid events, and on the other hand, the percentage of valid events with respect to all remaining events.

Using *Condition 1* with 7 MeV as an upper threshold for the summed energy deposition in scatter and absorber plane, the percentage of valid Compton events is increased from 10.9 to 11.8 % while only 1.5 % of the valid events are discarded, cf. table 4.4. Fig-

Table 4.4: Impact of event selection strategies. The CZT-LSO configuration together with the *patient source* is used. The depth-of-interaction in the scatter layer is referred to as DOI in this table and the value of ε_1 is set to 0.5 FWHM of the energy resolution of the detector layers, respectively, and ε_2 to 140 keV.

Condition	Discarded valid events	Valid events
no selection	0 %	10.9 %
Condition 1: $L_1 + L_2 \leq 7$ MeV	1.5 %	11.8 %
Condition 2: $\lvert 1 - m_0c^2 \left(\frac{1}{L_2} - \frac{1}{L_1+L_2}\right) \rvert \leq 1$	0 %	12.5 %
Condition 3: $L_1 \cap L_2 \notin [511\,\text{keV} \pm \varepsilon_1]$	3.2 %	11.5 %
Condition 4: $L_1 < L_2$	2.8 %	19.0 %
Condition 5: DOI < 4 mm	21.1 %	14.2 %
Condition 6: $L_1 + L_2 \in [4.44\,\text{MeV} \pm \varepsilon_2]$	92.1 %	19.5%
Conditions 1 - 5:	27.0 %	30.0 %

ure 4.7 suggests to only consider total energy depositions with an even lower upper energy threshold. There are two problems with respect to this approach: photons with a low energy are more likely already scattered inside the patient than photons with high energy. Furthermore, the energy resolution of the detectors improves with the energy of the photons due to the decreasing influence of Doppler broadening.

Condition 2 is useful and should always be applied since the percentage of valid Compton events is increased to 12.5 % without discarding any valid event. If the position of the source is known, the interval of feasible scattering angles can be used as an even more restrictive selection criterion. This range is evidently specific for each detector geometry, the position of the source, and the lower energy thresholds of the detectors. For the CZT-LSO setup no scattering in an angle larger than 52 $^\circ$ occurs for the *patient source*. Using this additional criterion the percentage of valid events can be increased to 18.2 %.

In order to study differences in the ratio of L_1 to L_2 between valid and invalid events, two-dimensional histograms, cf. figure 4.10, are plotted. From these plots it can be concluded that for the majority of valid events the inequality

$$L_2 > L_1 \tag{4.2}$$

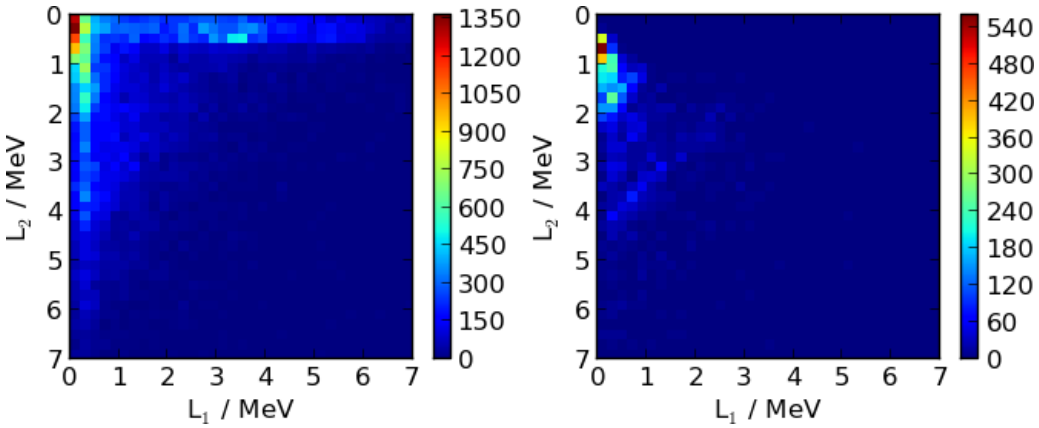

Figure 4.10: Distribution of the energy deposition between the scatter layer (L_1) and the absorber (L_2) for the CZT-LSO Compton camera using the *patient source* for all events (left) and valid Compton events (right).

holds. Applying this selection criteria (*Condition 4*), the percentage of valid events is increased substantially from 10.9 % to 19.0 % while only 2.8 % of the valid events are rejected.

Figure 4.10 also motivates *Condition 3*. In the left image of figure 4.10 the energy deposition of 511 keV in the absorber layer is prominent, which corresponds to invalid events. By neglecting events with energy depositions in one layer in the range [511 keV $\pm\,\varepsilon$], with ε being 0.5 FWHM of the energy resolutions, respectively, for the *patient source* and the CZT-LSO Compton camera 3.2 % of valid events are discarded and the percentage of valid events rises slightly to 11.5 %.

Figure 4.11 shows the detection probabilities of events, valid Compton events and percentage of valid Compton events as a function of the depth-of-interaction inside the CZT detector. Actually, the probability that an event is a valid Compton event decreases with the depth-of interaction. If events are selected according to an upper limit for the detection position, the number of valid events is reduced proportionally, whereas the percentage of valid Compton events is augmented considerably. For instance, for a threshold of 4 mm 14.2 % of the events are valid (cf. table 4.4) instead of 10.9 %. Therefore, it is necessary to study how accurate the depth-of-interaction can be determined in reality.

Exemplarily, *Condition 5* is tested for $E_{\text{Peak}} = 4.44\,\text{MeV}$, i.e. the most prominent peak in the simulated spectrum of prompt γ-rays. Out of $1.19 \cdot 10^{-1}$ expected γ-ray emissions per proton, there are $1.08 \cdot 10^{-2}$ photon emissions in the energy range $4.44\,\text{MeV} \pm 0.14\,\text{MeV}$. For irradiation with 10^{10} protons circa 660 events are registered with a total energy deposition in the range $4.44\,\text{MeV} \pm 0.14\,\text{MeV}$. Considering these events, the percentage of

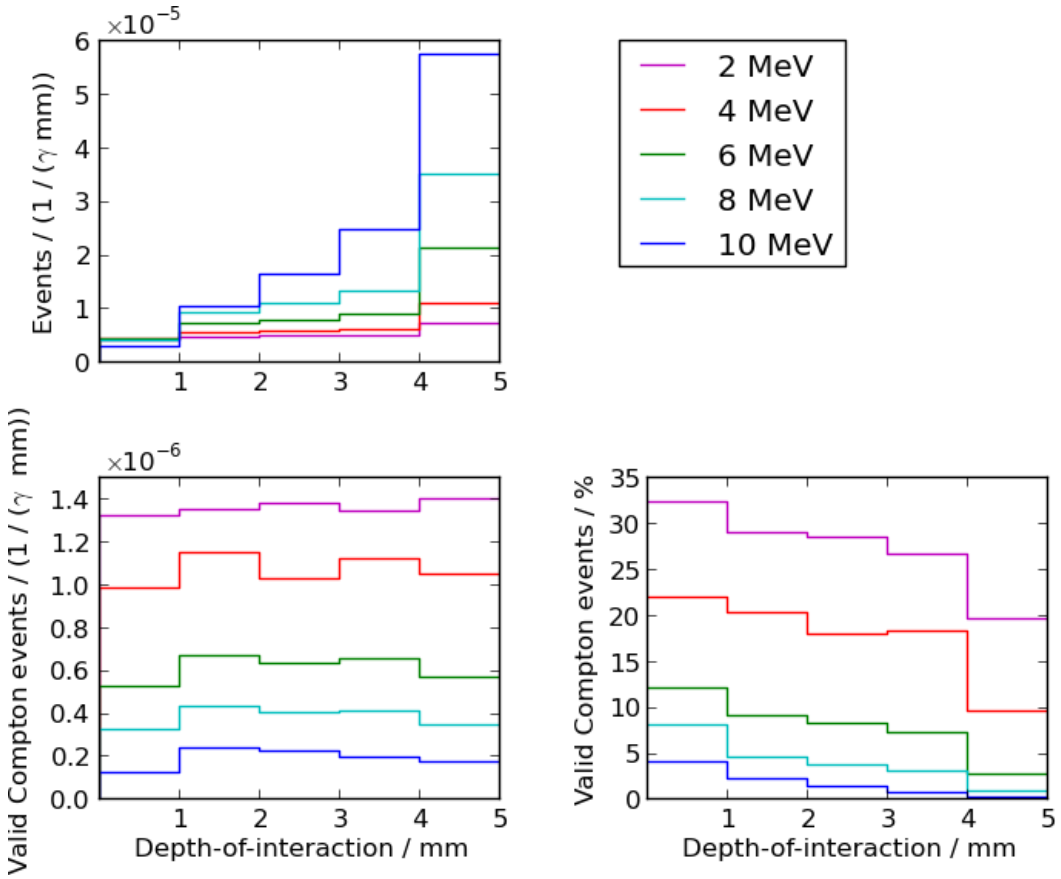

Figure 4.11: Simulated detection probability (top), number (bottom, left), and percentage of valid Compton events (bottom, right) as a function of the depth of the detection position (center of gravity) in the scatter layer. The CZT-LSO setup and a point source with different energies of the incident photon are used.

valid events is 19.5 %, but more than 90 % of valid events are neglected. Since up to now it is not determined how many events and which percentage of valid Compton events are required for a sufficient image reconstruction, the success of this event selection strategy cannot be evaluated definitely.

Finally, the combination of all promising selection criteria (1 - 5) is analysed. The sets of events discarded by the different approaches hardly overlap. By applying all promising conditions at the same time, a potentially acceptable rate of 30.0 % of valid Compton events can be achieved (cf. table 4.4).

Variations of the CZT-LSO detector setup

In the following, it is analysed how changes to the setup influence the detection probabilities and the percentage of valid events. Modifications of the geometry of the CZT-LSO prototype and the position of a point source are tested with respect to:

1. the distance of the source to the camera;
2. the distance between scatter and absorber layer;
3. the thickness of the CZT-detector;
4. the lateral transition of the source;
5. the rotation of the absorber layer by 45 degrees around the center of the scatter layer;
6. the lower energy thresholds of both detector layers;
7. the addition of a thin silicon detector in-between the scatter and absorption detector.

Depending on the patient and the location of the tumor the distance between Compton camera and the region of interest can vary with a minimum assumed at 10 cm distance. Obviously, this distance has influence on the detection probabilities. By enlarging the distance, the detection probabilities are reduced in the square, cf. figure 4.12. The fraction of valid Compton events remains approximately constant for the spectrum and studied distances between source and Compton camera of 10, 20, and 30 cm, cf. figure 4.12. For photons with 1 MeV the percentage of valid events decreases with the distance, while for 5 MeV photons the rate increases.

The larger the distance between scatter layer and absorber, the less is the probability that the absorber is hit and, therefore, the number of events decreases considerably,

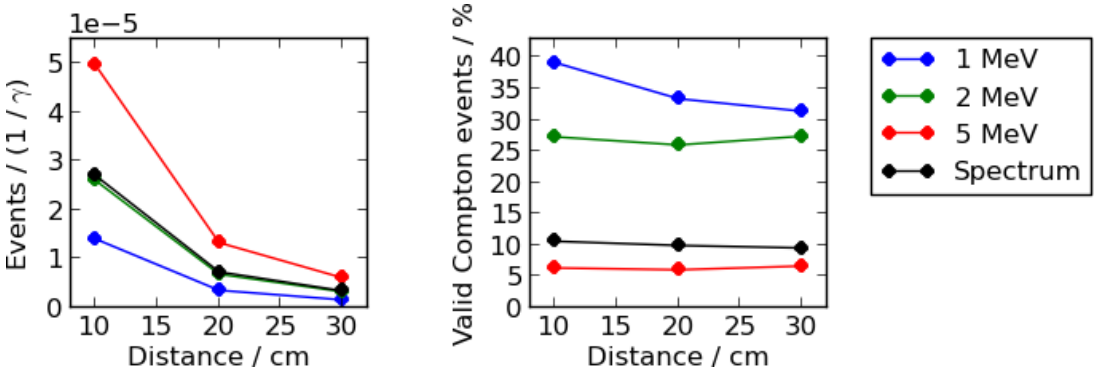

Figure 4.12: Simulated detection probability and percentage of valid Compton events for different distances between source and the camera. The point source and the CZT-LSO setup are used.

cf. figure 4.13. The variation of the distance between scatter and absorber layer influences the quality of the events due to the change of feasible scatter angles. For larger distances, only small scatter angles are feasible for a source centered in one line in front of the camera. For low energies, e.g. 1 MeV (cf. figure 4.13), the percentage of valid Compton events decreases when extending the distance due to the lower energy threshold causing the discard of many events with a small energy deposition in the scatter plane that is related to a Compton scattering with a small angle. The effect also causes the decrease of the percentage of valid events for 1 MeV photons when extending the distance to the source, cf. figure 4.12, since the distribution of feasible scattering angles is in this case also shifted towards smaller angles which are not very abundant for photons with 1 MeV due to the lower energy threshold. For energies from 5 MeV upwards the reduced rate of backscattered photons for an increased distance between scatter and absorber layer has a positive effect on the outcome. For the spectrum the rate is reduced slightly if the distance is increased from 6 to 10 cm.

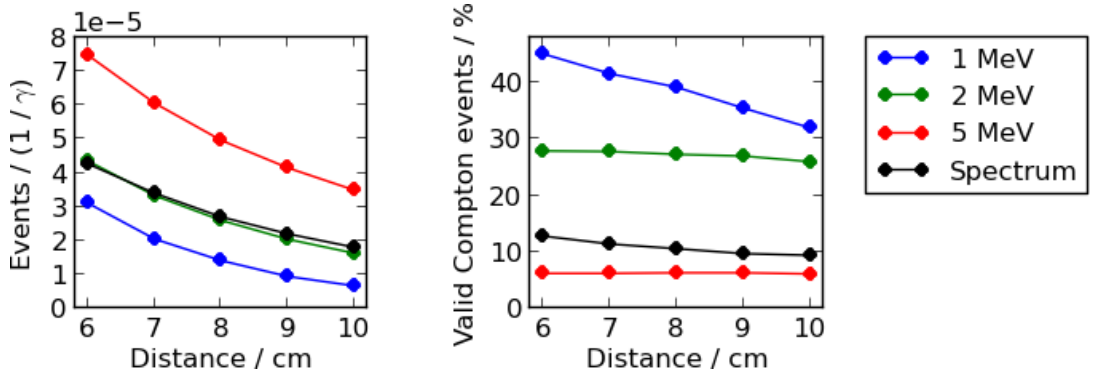

Figure 4.13: Number of events and percentage of valid Compton events for different distances between scatter and absorber plane. The CZT-LSO camera and a point source was used.

The choice of the thickness of detectors is always a balancing between efficiency and spatial resolution. Here, the influence of the depth is analyzed with respect to the quality of events. The thickness of the scatter layer was altered between 3 and 7 mm. With increasing thickness the percentage of valid events rises slightly, cf. figure 4.14. For the spectrum, the percentage of valid events is 2.2 % higher for 7 mm than for 3 mm. The reason for this is that the lower rate of energy escape from the scatter layer has more impact than the increasing rate of multiple Compton scatterings in the thicker CZT detector.

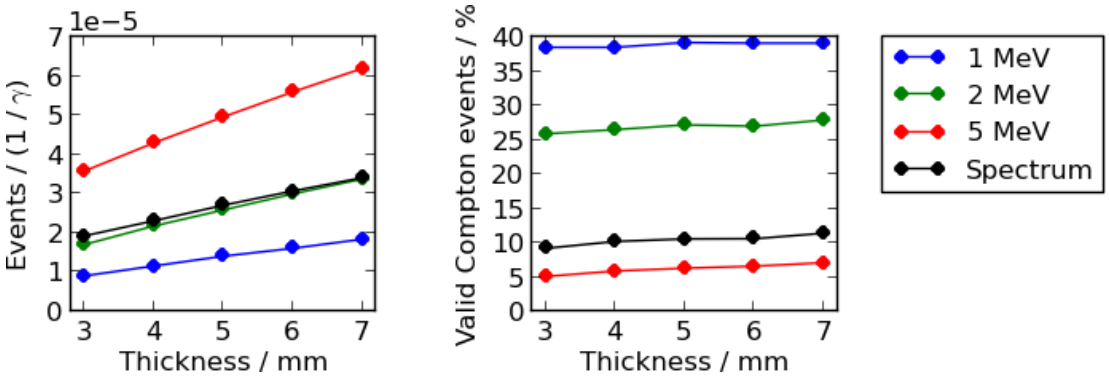

Figure 4.14: Number of events and percentage of valid Compton events for different thicknesses of the CZT-detector of the CZT-LSO camera. A point source is used.

Variation of the lower energy thresholds for both detector layers are tested. Thresholds between 10 and 200 keV are applied. The impact concerning the percentage of valid events is evidently dependent on the position of the source and the geometry of the detector. For the CZT-LSO setup and the point source placed in a central position in front of it, the percentage of valid events increases the lower the energy threshold in the CZT and the higher the energy threshold in the LSO. This observation is due to the neglection of valid events with a small energy deposit in the CZT and the rejection of many invalid events originating from low energetic secondary particles in the LSO. Setting the thresholds to 50 keV in the CZT and to 200 keV in the LSO instead of 100 keV and 50 keV, respectively, the percentage of valid Compton events increases from 10.6 % to 15.3 %. In reality, a lower energy threshold of 50 keV is rather not practical for the CZT detector, but this brief study shows how a tuning of lower energy thresholds influences noise.

When the scattering angles are small, in addition to the problem of the neglection of valid events due to the energy threshold in the scatter detector, another problem is the high rate of energy escape from the absorber resulting from the relatively high energy of the scattered photon. There are two possibilities to alter the distribution of Compton scattering angles. The first one is the change of the position of the source and the second one is the rotation or translation of the absorber. As an example, the source is translated 10 cm

to one side, cf. figure 4.15, and in another simulation, the absorber is rotated 45 degrees around the center of the scatter plane, cf. figure 4.16.

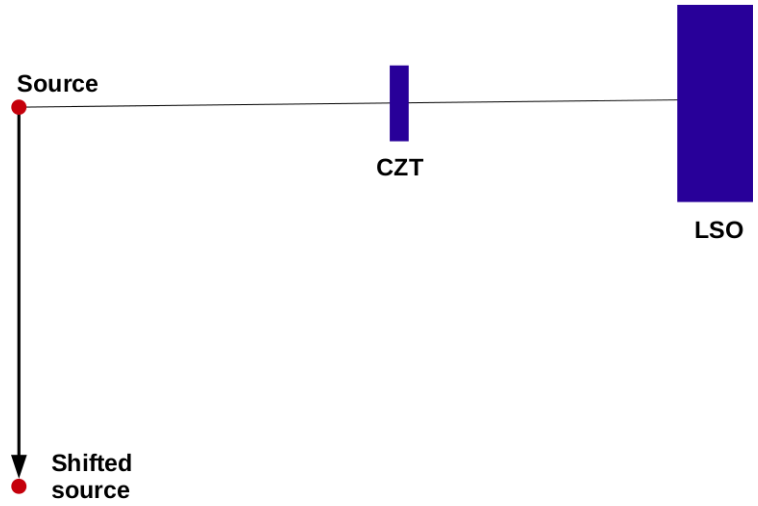

Figure 4.15: CZT-LSO camera with a laterally shifted source.

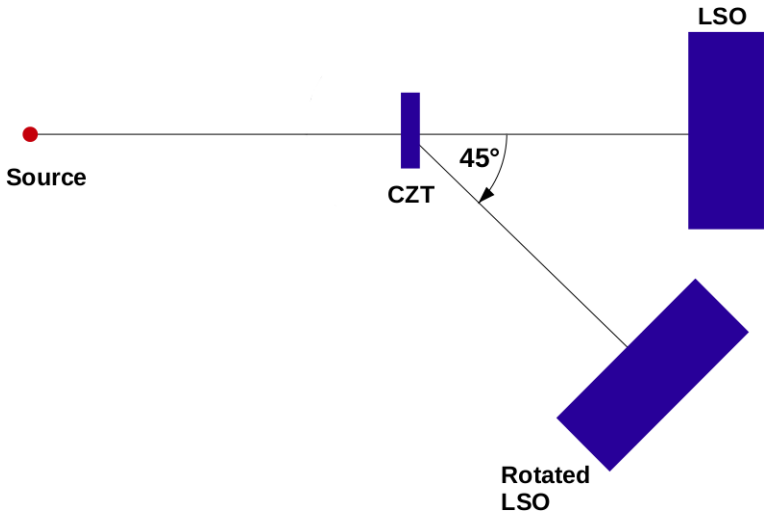

Figure 4.16: Modified CZT-LSO camera: the LSO block is rotated around the center of the CZT detector by 45 degrees.

The outcome depends on the initial energy, cf. figure 4.17. For energies of 5 MeV the rotation or translation of the source is disadvantageous, the percentage of valid events decreases from 6.3 % to 3.8 %. This is caused by a higher disturbance of pair production events in the scatter plane with secondaries hitting the absorber. The opposite is true for small energies and the realistic spectrum. For 1 MeV the percentage of valid events is increased from 39.2 % to 54.2 % and 56.8 % for the rotation of the absorber and the lateral translation of the source, respectively. The percentage of valid Compton events

rises from 10.6 % to more than 20 % for the spectrum for both the rotation of the absorber and the translation of the source.

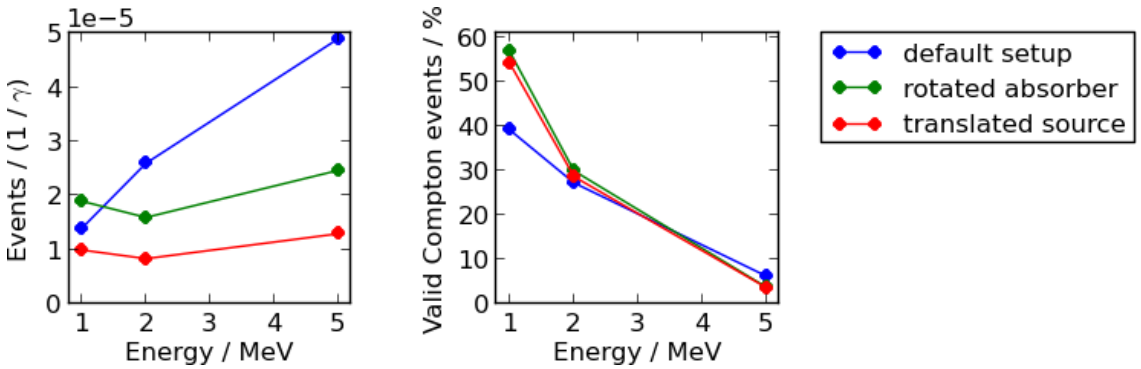

Figure 4.17: Number of events and percentage of valid Compton events for the default setup, the rotated absorber (figure 4.16), and the translated source (figure 4.15) as a function of the energy of the incident photons.

With a thin silicon detector added between the CZT and the LSO, cf. figure 4.18, charged particles escaping from the CZT can be tracked while photons usually do not interact in the silicon detector. This camera is called CZT-Si-LSO in the following. Since charged particles are associated with invalid events, in particular escaping Compton electrons and electrons and positrons following a pair production, events with an energy deposition in the silicon can be discarded. For the silicon a lower energy threshold of 10 keV is assumed. For the spectrum, the percentage of valid events is increased from 10.6 % to 14.8 % for a point source.

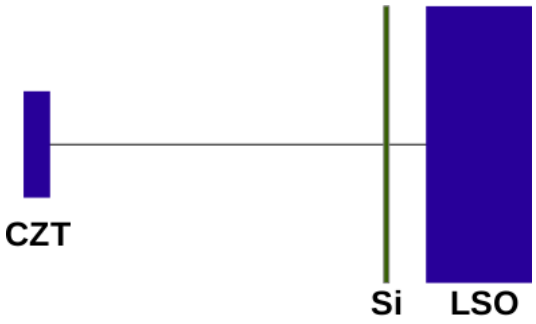

Figure 4.18: CZT-Si-LSO camera: CZT-LSO detection system with a thin silicon layer between the CZT and the LSO detector.

Combinations of detectors to one or several Compton cameras

Due to the availability of many BGO detectors, the question is how CZT and BGO detectors could be combined best, i.e., how larger dimensions influence the detection probabilities and the percentage of valid events and whether a large number of cameras with small dimensions is in favor of a small number of cameras with large dimensions. The scatter layer is varied by applying four CZT detectors ($2 \times 2 \times 0.5\,\mathrm{cm}^3$) instead of one. As absorber one, four, or sixteen BGO detectors ($5.2 \times 5.2 \times 2\,\mathrm{cm}^3$) are used. More precisely, the setups 1 CZT + 1 BGO (standard, Setup A), 1 CZT + 4 BGO (Setup B), 4 CZT + 4 BGO (Setup C), and 4 CZT + 16 BGO (Setup D) are considered, cf. figure 4.19. Since from four CZT detectors and four BGO detectors either Setup C or four times the Setup A can be constructed, a conclusion to the above question can be derived. The same applies to four CZT detectors and sixteen BGO detectors which can be used to build Setup D or four times Setup B. In the table 4.5 the number of events and the rate and number of valid events for the mentioned detector configurations are shown for the *patient source*. Since from a practical point of view the load to each of the detector layers can be crucial, the number of hits, i.e. single energy depositions in the scatter and absorber layer, respectively, is listed in table 4.6.

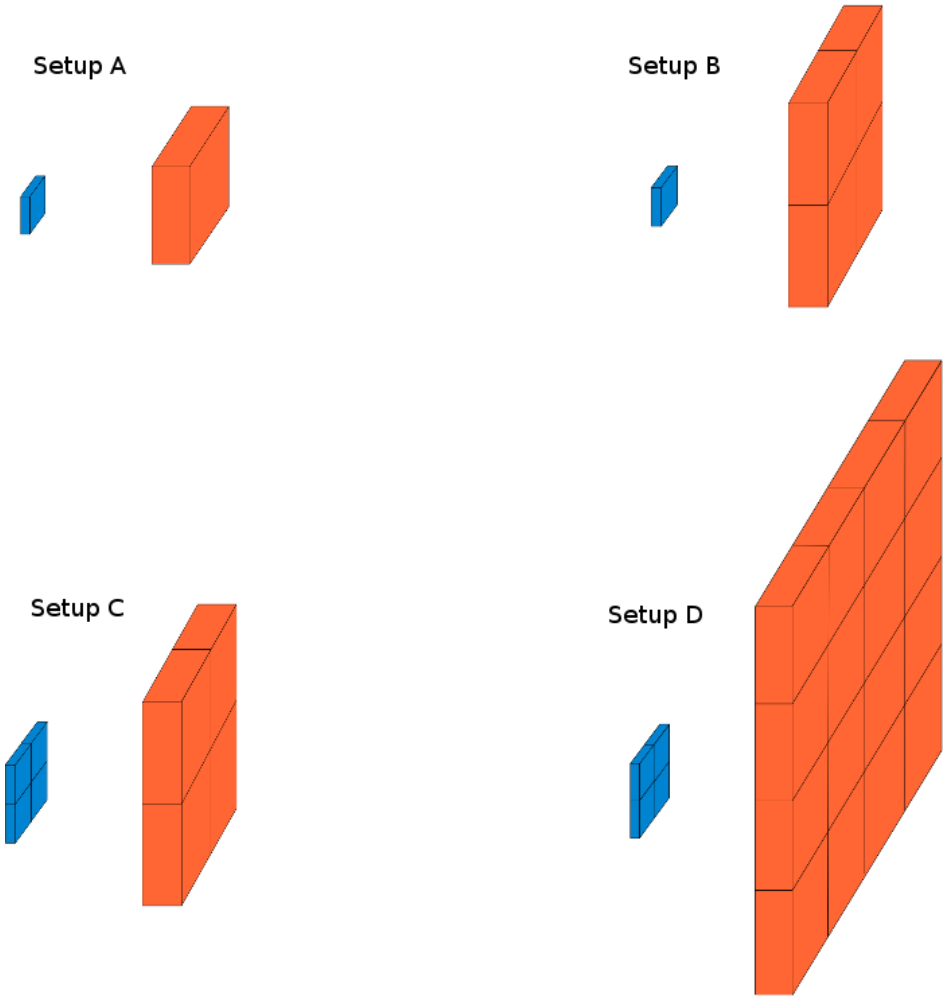

Figure 4.19: Variation of the CZT-BGO Compton camera. The CZT detectors are depicted in blue, the BGO detectors in orange: 1 CZT + 1 BGO (top, left), 1 CZT + 4 BGO (top, right), 4 CZT + 4 BGO (bottom, left), and 4 CZT + 16 BGO (bottom, right).

Table 4.5: Detection probabilities, rate and number of valid events for different Compton camera setups consisting of CZT and BGO detectors, cf. figure 4.19. The *patient source* is used.

Setup	Events / $(1/\gamma)$	Valid events / %	Valid events / $(1/\gamma)$
Setup A (1 CZT + 1 BGO)	$1.19 \cdot 10^{-5}$	13.3 %	$1.58 \cdot 10^{-6}$
Setup A $\times$ 4	$4.76 \cdot 10^{-5}$	13.3 %	$6.32 \cdot 10^{-6}$
Setup C (4 CZT + 4 BGO)	$1.18 \cdot 10^{-4}$	20.8 %	$2.46 \cdot 10^{-5}$
Setup B (1 CZT + 4 BGO)	$3.09 \cdot 10^{-5}$	20.6 %	$6.35 \cdot 10^{-6}$
Setup B $\times$ 4	$1.24 \cdot 10^{-4}$	20.6 %	$2.54 \cdot 10^{-5}$
Setup D (4 CZT + 16 BGO)	$2.18 \cdot 10^{-4}$	27.8 %	$6.06 \cdot 10^{-5}$

Table 4.6: Hits (number of energy depositions) registered in the scatter detector (CZT) and absorber layer (BGO) for different Compton camera setups, cf. figure 4.19. The *patient source* is used.

Setup	Hits in CZT / $(1/\gamma)$	Hits in BGO / $(1/\gamma)$
Setup A (1 CZT + 1 BGO)	$2.49 \cdot 10^{-4}$	$2.18 \cdot 10^{-3}$
Setup A $\times$ 4	$9.96 \cdot 10^{-4}$	$8.72 \cdot 10^{-3}$
Setup C (4 CZT + 4 BGO)	$1.00 \cdot 10^{-3}$	$8.40 \cdot 10^{-3}$
Setup B (1 CZT + 4 BGO)	$2.53 \cdot 10^{-4}$	$8.93 \cdot 10^{-3}$
Setup B $\times$ 4	$1.01 \cdot 10^{-3}$	$3.57 \cdot 10^{-2}$
Setup D (4 CZT + 16 BGO)	$1.01 \cdot 10^{-3}$	$3.19 \cdot 10^{-2}$

Table 4.5 indicates that an enlarged absorber has more impact on the percentage of valid events than an enlarged scatter layer, cf. Setup B and Setup C. In terms of the efficiency and the number and percentage of valid events, it is beneficial to build from a given number of these CZT and BGO detectors large-area cameras instead of many small ones, cf. table 4.5. Setup C is in favor of four times Setup A and Setup D gives a higher efficiency and higher percentage of valid events than four times Setup B. With respect to the load on the absorber, large-area detectors are also slightly advantageous, cf. table 4.6. For a definite answer to the questions for an optimal arrangement of the detectors to few large or several small cameras, additionally the image quality of the reconstructed images needs to be taken into account.

4.2 Comparison with experimental data

Several experiments have been conducted to assess the Compton Camera prototypes (Kormoll, 2013; Hueso-González et al., 2014). Here, a measurement with a sodium-22 source and the experiment at the Tandetron accelerator at HZDR are chosen for a comparison with simulation results regarding the obtained energy depositions in each detector. These experiments were performed by the In-vivo dosimetry group (OncoRay), in particular by Christian Golnik.

4.2.1 Experiment with a sodium-22 source

The isotope ^{22}Na decays to an excited state of ^{22}Ne which turns to the ground state of ^{22}Ne by emitting a photon with 1275 keV. 90 % of the decays from ^{22}Na to the excited state of ^{22}Ne are β^+-decays, the remaining 10 % are electron captures. For this experiment a point-like ^{22}Na source with an activity of $2.96 \cdot 10^5$ Bq is placed 10 cm in front of the Compton camera. The CZT-BGO setup with 8.5 cm in-between the detector layers is used. Lower energy thresholds of 50 keV and 150 keV are applied for CZT and BGO, respectively. In order to reduce the rate of random coincidences in the experimental data only events with a total energy deposition between 1020 keV and 1530 keV are taken into account. Furthermore, the criteria concerning the feasible scattering angles, cf. *Condition 2* is used.

For the GEANT4 simulations the total number of ^{22}Na decays is assumed to be $3.7 \cdot 10^9$ according to the duration of the measurement. The same selection criteria used for the measured data as well as the lower energy thresholds are applied to filter the simulated data. In contrast to the previous simulations, the width and height of the CZT detector is reduced from 2 cm to 1.6 cm to take into account the sensitive area of this CZT detector.

In general, a good agreement between simulated and measured data is obtained, cf. figure 4.20, except for the following facts:

- The number of simulated and experimental events differs by a factor of 3. As a consequence, the in-vivo dosimetry group (OncoRay) reexamined the efficiency of the applied Compton camera prototype and determined a loss of two thirds of the events for this experiment, which explained the observed difference.
- In contrast to the simulations, the experimental data contain random coincidences: there is a considerable amount of energy depositions of circa 511 keV in both detector layers. If a photon with 1275 keV interacts in one of the detector layers and an annihilation photons resulting from the β^+-radiation of the ^{22}Na source is absorbed simultaneously in the other one, these random events occur.

- In the histogram of the simulated energy depositions in the CZT a peak is clearly visible that is not present for the measurements. This peak results from backscattered photons, i.e. those photons which are first scattered backwards in the BGO and are then absorbed in the CZT. Due to the applied anode trigger regime the energy of the photons is not registered accurately enough to recognize this peak in the experimental data.

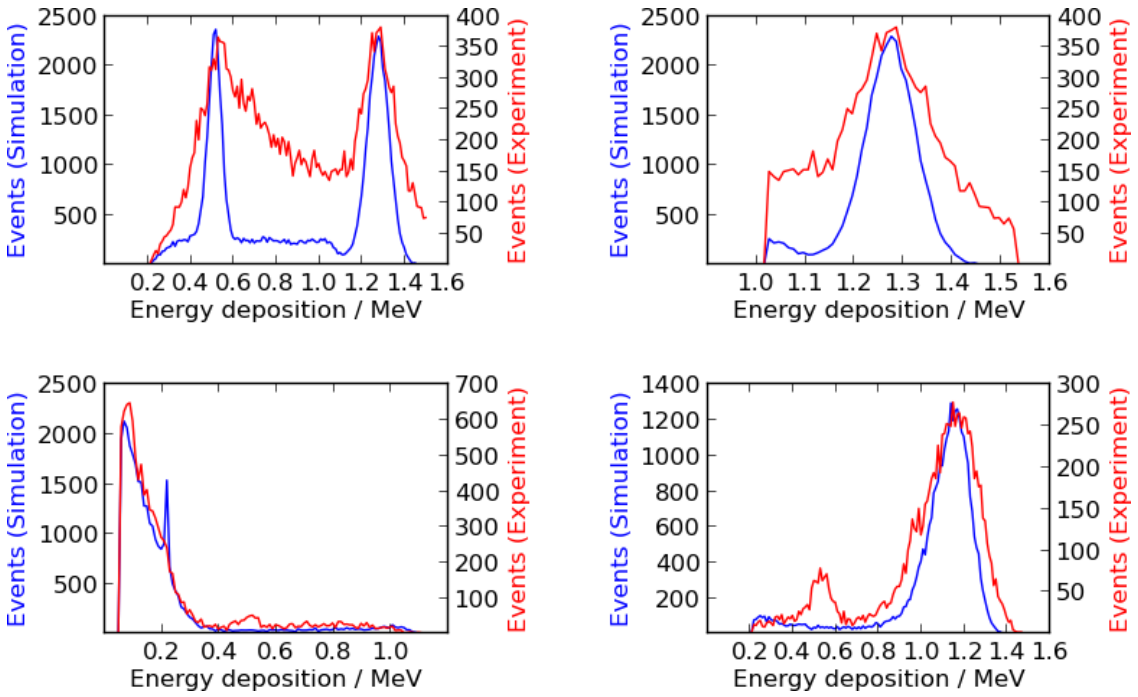

Figure 4.20: Comparison of measured (red) and simulated (blue) energy depositions registered in the CZT-BGO setup with 8.5 cm between the detector layers for a ^{22}Na point source placed in 10 cm distance to the camera. Top left: sum of energy depositions in CZT and BGO without energy window. Top right: sum of energy depositions in CZT and BGO. Bottom left: energy depositions in the CZT detector. Bottom right: energy depositions in the BGO detector. The bin size of the histogram is 10 keV. Except for the first image (top left), the summed energy is restricted to [1.020 MeV, 1.530 MeV].

4.2.2 Experiment with 4.44 MeV photons

Another measurement with the Compton camera prototype was performed at the Tandetron at HZDR. At the Tandetron, a proton beam is directed on a nitrogen-titanium target resulting in 4.44 MeV photon emissions from the nuclear reaction $^{15}\mathrm{N}(p,\ \alpha\gamma)^{12}\mathrm{C}$. The fluence of the 4.44 MeV photons was monitored by an additional germanium detector. During the measuring time of 64589 s a presumed number of $5.319 \cdot 10^8$ γ-ray emissions occur, which is used for the simulations. The CZT-BGO configuration with a distance of 7.5 cm between the detector layers is used. BGO was applied instead of LSO since the

intrinsic radioactivity of LSO would have compromised the measurements due to the low count rate at the Tandetron. For the CZT and BGO lower energy thresholds of 50 keV and 200 keV, respectively, were assumed. As selection criteria for the simulated and the experimental data, *Condition 2* and an energy window of [2.734 MeV, 5.328 MeV] were applied.

The comparison between measurements and simulation for the Tandetron experiment is shown in figure 4.21, revealing the following:

- The measured detection probability is about three times lower than the simulated one, as observed for the ^{22}Na experiment.
- Concerning the total energy depositions, the 4.44 MeV peak and the two other peaks corresponding to the single and double escape of annihilation photons following a pair production are clearly visible in the simulated data but not in the measured data.
- Considering the data without energy restriction (top left), the relatively high number of energy depositions lower than 1.7 MeV is apparent. Their origin is certainly due to the natural background irradiation of ^{40}K, which led to 40 % of the single counts during the experiment.
- Both for the simulated and the measured data, a lot of energy depositions of about 511 keV are visible for the CZT and the BGO, which are due to the absorption of an annihilation photon resulting from a pair production in the other detector. For the measured energy depositions in the CZT this peak is shifted to the left hand side. For the simulated data the peak at 3.4 MeV in the CZT detector corresponding to a pair production in this detector with escape of both resulting annihilation photons is striking, but not remarkable in the experimental data.

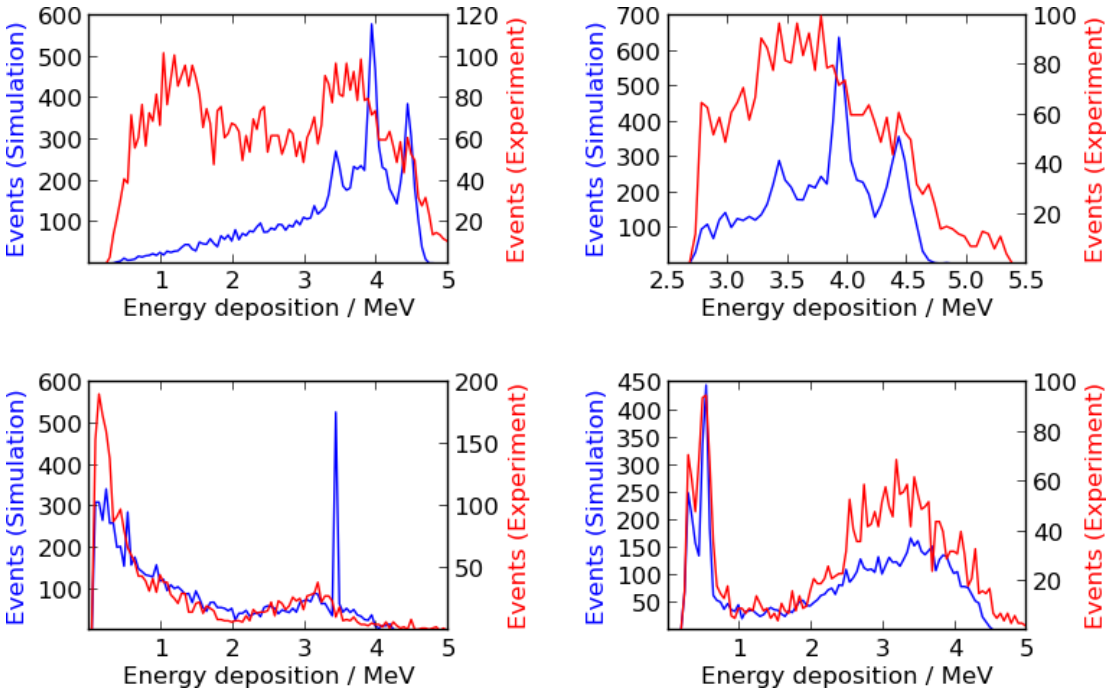

Figure 4.21: Comparison of measured (red) and simulated (blue) energy depositions registered with the CZT-BGO setup with 7.5 cm between the detector layers for γ-ray emissions with 4.44 MeV. Top left: sum of energy depositions in CZT and BGO without energy window. Top right: sum of energy depositions in CZT and BGO. Bottom left: energy depositions in CZT. Bottom right: energy depositions in BGO. The bin size of the histogram is 50 keV. Except for the first image (top left) the summed energy is restricted to [2.734 MeV, 5.328 MeV].

4.3 Simulation of pair production events

Due to the expected energy range of prompt γ-rays, cf. figure 2.1, a considerable number of pair productions occurs in the Compton camera instead of Compton scatterings. In this section it is investigated whether positrons and electrons resulting from a pair production can also be used for the successful reconstruction of the direction of the incident photon. Thus, the total efficiency of this PGI device could be enhanced. Simulations with GEANT4 are performed to assess the efficiency of this detection system used as pair production camera in comparison with the use as Compton camera. Since apart from the efficiency, the angular resolution is a crucial property of PGI devices, this is also evaluated taking into account the uncertainty concerning the kinetic energy of electron and positron and the influence of the geometry of the setup.

4.3.1 Working Principle of Pair Production Cameras

The working principle of a pair production camera relies on the conversion of photons to electron-positron pairs. These pair productions predominantly take place in the nuclear field. Pair productions in the field of an electron (triplet production) occur with a considerable lower cross section compared to pair production in the field of a nucleus (Berger et al., 2014) and are neglected in the following. If the position where the pair production occurs, and the tracks and kinetic energies of the resulting electron and positron are known, the direction of the photon can be back projected by means of energy and momentum conservation rules (Zoglauer, 2005; Golnik et al., 2011), cf. equations (4.3) and (4.4).

$$E_\gamma = E_{e^+} + E_{e^-} + E_Q + 2m_0c^2 \tag{4.3}$$

$$\boldsymbol{p}_\gamma = \boldsymbol{p}_{e^-} + \boldsymbol{p}_{e^+} + \boldsymbol{Q} \tag{4.4}$$

E_γ, E_{e^-}, E_{e^+}, and $\boldsymbol{p}_\gamma$, $\boldsymbol{p}_{e^-}$, $\boldsymbol{p}_{e^+}$ are the energies and momenta of the incident photon, electron, and positron, respectively. E_Q and $\boldsymbol{Q}$ denominate the energy and the momentum transferred to the nucleus, respectively.

In practice the recoil of the nucleus $\boldsymbol{Q}$ and the corresponding energy E_Q are unknown, only the energies deposited in the detectors and the tracks of electron and positron can be registered. Consequently, the direction $\boldsymbol{d}_\gamma^{BP}$ is deduced by adding the directions of electron and positron ($\boldsymbol{d}_{e^-}$ and $\boldsymbol{d}_{e^+}$) weighted with the magnitudes of the momenta (p_{e^+} and p_{e^-}) which are calculated from the measured kinetic energies (E_{e^-} and E_{e^+}), cf. equation (4.5):

$$\boldsymbol{d}_\gamma^{BP} = p_{e^-}\boldsymbol{d}_{e^-} + p_{e^+}\boldsymbol{d}_{e^+} \tag{4.5}$$

$$\text{where } p_{e^+} = \frac{1}{c}\sqrt{2m_0c^2E_{e^+} + E_{e^+}^2} \tag{4.6}$$

$$\text{and } p_{e^-} = \frac{1}{c}\sqrt{2m_0c^2E_{e^-} + E_{e^-}^2}. \tag{4.7}$$

4.3.2 Methods

The following analysis is focused on events originating from a pair production in the scatter layer and an absorption of the resulting electron and positron in the absorber, as depicted in figure 4.22 for the CZT-LSO camera. These events are referred to as pair production events.

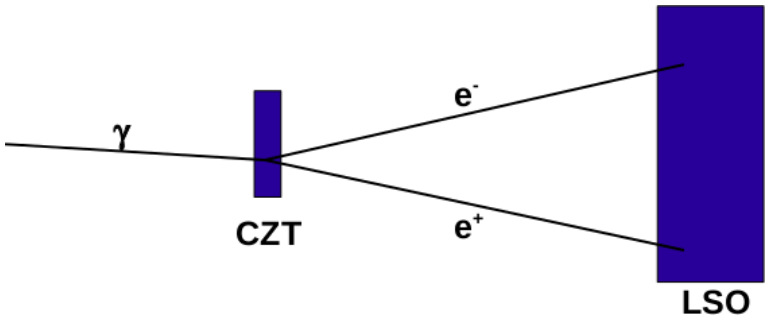

Figure 4.22: A pair production event in the CZT-LSO camera.

A requirement for the utilization as pair production camera is the capability of the absorber to register electron and positron simultaneously and to provide for each lepton the detection position and the deposited energy, i.e., a pixelated detector with a readout channel for each pixel would be necessary. With the current Compton camera prototype the individual tracking of electron and positron is not possible due to the design of the LSO block detector (Hueso-González et al., 2014). Nevertheless, in this simulation study an event is considered as pair production event if in two different crystals of the size $4 \times 4 \times 20\,\text{mm}^3$ energy is deposited exceeding the lower threshold. This concept enables the automatic discrimination between pair production events and Compton events.

In addition to the CZT-LSO camera, the CZT-Si-LSO camera with a 0.1 mm thick silicon detector placed in front of the absorber, cf. figure 4.18, is used. The silicon detector serves for the detection of charged particles. Photons usually do not interact in the silicon detector while electrons and positrons interact inelastically with a very high probability. Therefore, the silicon layer is intended to filter random events. Since silicon detectors can achieve a high energy resolution (Tindall et al., 2008), energy blurring induced by this detector is neglected in the following.

The efficiency of the combined Compton - pair production camera is studied for point

sources in 10 cm distance with energies up to 15 MeV. In addition to that, the *patient source*, which represents a therapeutic scenario (cf. section 4.1.1), is used.

For the back projection of a pair production event, the detection position in the CZT detector and the two ones in the LSO detector are calculated as follows: for the position in the CZT where the pair production occurs the center of gravity is used. For the interactions of electron and positron in the LSO detector the centers of gravity are calculated separately for both leptons. Then the direction of the photon is derived by adding up the two direction vectors of electron and positron weighted with the corresponding energy, cf. equation (4.5), where the energy deposited in the CZT layer is assumed to result equally from interactions of electron and positron. This vector is projected onto a virtual plane which is perpendicular to the camera orientation in 10 cm distance and contains the actual position of the source. The Field-Of-View (FOV) of the prototype with respect to pair production events is strongly limited by its geometry, cf. figure 4.23. To take into account the influence of the source position on the imaging quality, in addition to the central position, the source is shifted laterally by 1 and 2 cm and the corresponding back projections are performed. Furthermore, an LSO absorber with an enlarged dimension ($104 \times 104 \times 20$ mm^3 instead of $52 \times 52 \times 20$ mm^3) was considered to alter the FOV.

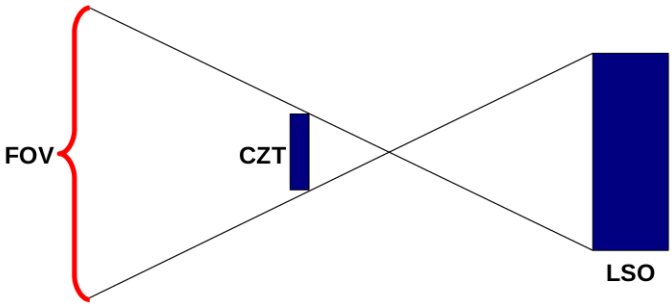

Figure 4.23: The CZT-LSO camera with indicated Field-Of-View (FOV) for the utilization as pair production camera.

For the evaluation of the angular resolution of this pair production camera the 68 %-confinement angle is chosen as a figure of merit. The 68 %-confinement angle was used before (Kanbach et al., 2005; Golnik et al., 2011). This angle denominates the angle containing 68 % of all back projected photon directions. For the MEGA-prototype a 68 %-confinement angle of 16 degrees for photons of 10 MeV was obtained (Zoglauer, 2005).

For the back projection according to equation (4.5), in principle, the correct kinetic energies of the electron and the positron are required. If the electron or the positron escapes from the absorber, or if annihilation photons do not escape, the measured energy depositions do not equal the kinetic energies. Furthermore, inelastic interactions of electron

and positron in the air and the energy resolutions of the detectors result in further uncertainties. The impact of the unknown kinetic energies on the back projection result is analyzed by varying the assumed kinetic energies of electron and positron for the back projection. More precisely, first the simulated energy depositions are used as kinetic energies taking into account the energy resolution of the detectors. Secondly, the energy resolution is ignored. Then, exclusively events with complete absorption of electron and positron and escape of both annihilation photons are considered. Furthermore, the energy is assumed to be equally distributed between electron and positron. Finally, to avoid the uncertainty induced by interactions in air and the spatial uncertainty of the detection positions, the exact initial energies of electron and positron are extracted from GEANT4 and the momenta of electron and positron at the moment of the escape from the CZT are directly used for the back projection, i.e. the only deviation is induced by the interactions (multiple scatterings) in the CZT.

The recoil of the nucleus is not taken into account by GEANT4. With an additional calculation the recoil of the nucleus can be modeled and its influence on the angular resolution of the pair production camera can be studied (Golnik et al., 2011).

4.3.3 Results

If a pair production takes place in the CZT detector, not all electron-positron pairs reach the absorber. Table 4.7 lists the number of pair productions in the CZT and the resulting processes, taking into account the energy thresholds of the detectors. First, the number of energy depositions resulting from a pair production in the CZT (1) and the number of escaping electron-positron pairs resulting from this pair production (2) are given. In the case of the CZT-Si-LSO camera the number of electron-positron pairs which also interact in the silicon layer is indicated. Furthermore, the number of these electron-positron pairs with sufficient energy deposition in the LSO is listed (3). These events are considered here as pair production events. In the next step, those events of (3) where the electron-positron pair is completely absorbed in the LSO (4) and those with escape of both annihilation photons (5) and those without escape of secondary particles are extracted (6). Obviously, for almost every pair production occurring in the CZT detector the kinetic energy of the electron and the positron is not given by the measured energy depositions.

Table 4.7: Different processes following a pair production in the CZT layer. For these simulations 10^9 photons with an energy of 10 MeV are emitted isotropically from a point source in 10 cm distance.

	CZT-LSO	CZT-Si-LSO
(1) pair production in CZT	217159	217129
(2): (1) and e^- and e^+ escape from CZT	33465	33511
and interact in Si (CZT-Si-LSO camera)		4907
(3): (2) and e^- and e^+ interact in LSO	3330	2656
(4): (3) and e^- and e^+ are absorbed in LSO	2276	1670
(5): (4) and annihilation photons escape	702	512
(6): (5) and no escape of other secondaries	249	218

Graph 4.24 depicts the efficiencies of the use as pair production camera and Compton camera as a function of the initial photon energy. For photons with energies higher than 8 MeV, the probability that a pair production event takes place is higher than the probability of a valid Compton event.

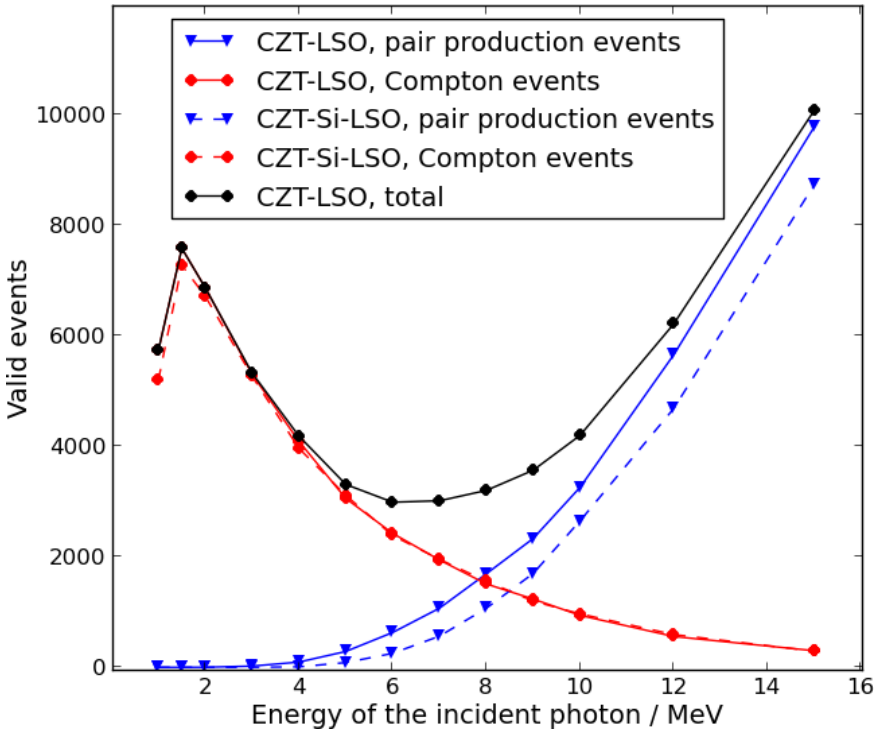

Figure 4.24: Number of pair production events and valid Compton events. For these simulations the CZT-LSO and the CZT-Si-LSO setup are used and 10^9 photons with an energy between 1 MeV and 15 MeV are emitted isotropically from a point source in 10 cm distance.

The overall gain in efficiency is demonstrated by table 4.8 providing the number of pair production events in comparison with valid Compton events for the *patient source* for 10^{10} incident protons. For both, the CZT-LSO and the CZT-Si-LSO camera, the number of valid Compton events is one magnitude higher than the number of pair production events, i.e. the total efficiency of a combined Compton - pair production camera can be expected to be only about 10 % higher compared to the Compton camera alone for a realistic spectrum of photons.

Table 4.8: Number of valid Compton events and pair production events. The *patient source*, cf. figure 2.1, for 10^{10} incident protons is used.

Setup	Valid Compton events	Pair production events
CZT-LSO	$1.7 \cdot 10^3$	$1.2 \cdot 10^2$
CZT-Si-LSO	$1.6 \cdot 10^3$	$0.9 \cdot 10^2$

Figure 4.25 shows images obtained by back projecting the pair production events that are registered in the CZT-LSO setup. The source is placed in central position and shifted laterally by 1 and 2 cm. The sources with the 1 cm and the 2 cm shift are not reproduced accurately, the hot spots do not appear at the correct positions. This result indicates the limited imaging capabilities of this pair production camera that are due to its geometry and the large impact of the multiple scattering in the CZT which leads to a considerable randomization of the tracks of electron and positron.

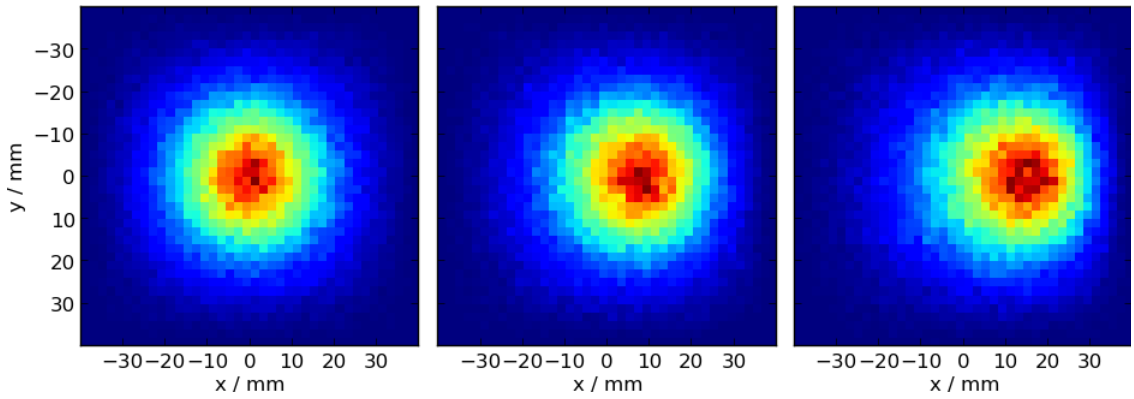

Figure 4.25: Results of the back projection of pair production events which are registered with the CZT-LSO camera. The tracks of electron and positron are back projected onto a virtual plane in 10 cm distance from the CZT. The point source is placed in a straight line in front of the camera (left), shifted by 1 cm laterally (center), and shifted by 2 cm laterally (right).

Figure 4.26 shows the distribution of the deviation between the back projected and the actual direction of the photons for different assumptions. The corresponding 68 %-confinement angles are provided in table 4.9. For this study the CZT-LSO and a point source with 10 MeV in a distance of 10 cm is used emitting photon beams to the center of the CZT detector. It can be observed that the uncertainty resulting from the unknown kinetic energies has negligible impact on the outcome. Neither the exclusive use of events fulfilling (6) in table 4.7, nor the use of the accurate energies and the momenta of the leptons escaping from the CZT and, thereby, only including the influence of multiple scattering in the CZT detector, do not lead to an improvement. Even if the energies of electron and positron are assumed to be equal, the same accuracy is obtained. However, the insignificant influence of the energies of electron and positron on the angular resolution agrees with the fact that in astronomy usually approximations of equation (4.5) are used for the back protection (Zoglauer, 2005).

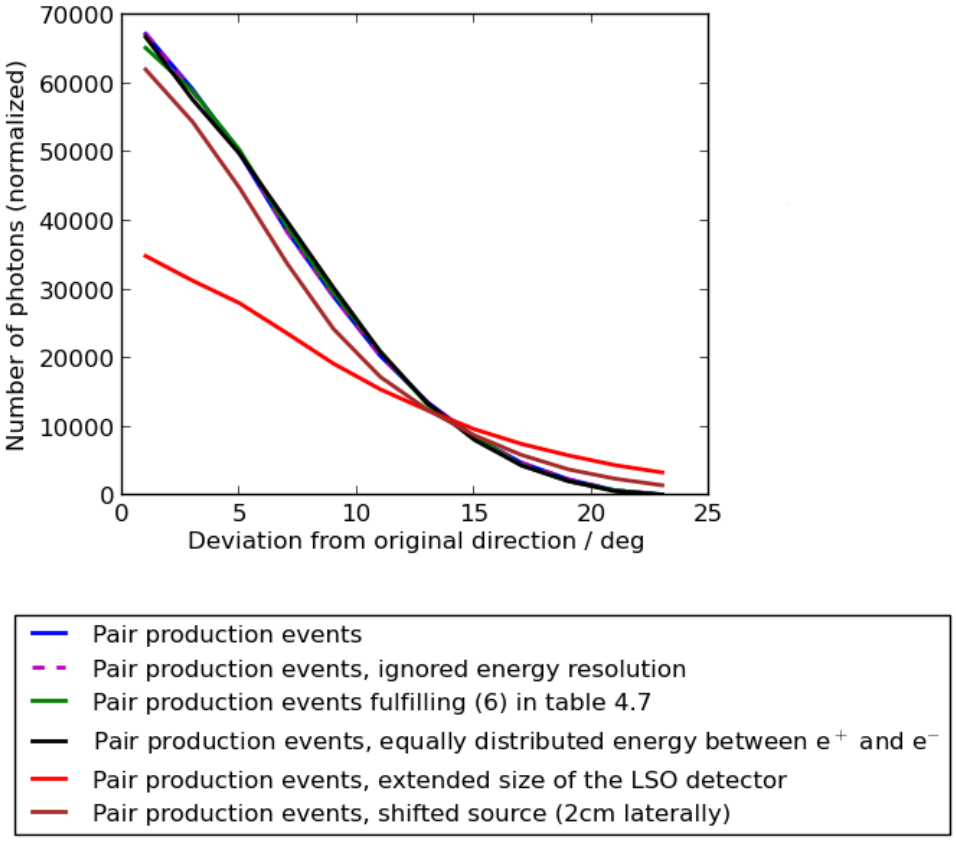

Figure 4.26: Distribution of the deviation between the back projected direction of the photon and the original one for pair production events. The CZT-LSO setup and a point source with 10 MeV in central position is used. The photons are directed to the center of the CZT detector. The values are corrected for the solid angle of the bins.

Table 4.9: The 68%-confinement angles for back projected pair production events. The CZT-LSO setup is used, "extended size of LSO" means its width and height is extended (to $104 \times 104 \times 20$ mm^3). The point source is placed in 10 cm distance in front of the camera, in central position and shifted laterally by 1 cm and 2 cm, respectively. The photons of 10 MeV are directed to the center of the CZT detector.

	Angle / deg
Pair production events	11.134
Pair production events, ignored energy resolution	11.130
Pair production events fulfilling (6) in table 4.7	11.008
Pair production events, equally distributed energy between e^+ and e^-	10.978
Pair production events, exact energies of e^+ and e^- and momenta of e^+ and e^- escaping the CZT detector	11.124
Pair production events, extended size of the LSO detector	17.101
Pair production events, shifted source (1 cm laterally)	11.338
Pair production events, shifted source (2 cm laterally)	12.723

Table 4.9 and figure 4.26 show that the position of the source, as well as changes to the geometry have considerably more influence on the angular resolution than the uncertain energy distribution between the leptons. This can be explained by the limitations of possible directions of electron and positron caused by the camera design.

The obtained angular resolution seems not to be sufficient for the application of this camera to the in-vivo monitoring of particle therapy. Assuming the spatial resolution to be a Gaussian distribution, the 68 %-confinement angle of 11 degrees is equivalent to a spatial resolution of about 2.3 cm FWHM for a source in 10 cm distance from the CZT detector. This value is certainly not enough to detect range deviations of a few millimeters. It should be considered that since 10 MeV is already a very optimistic energy value for prompt γ-rays and since the recoil of the nucleus is omitted here, the realistic angular resolution is therefore even worse.

5 On the application of Time-of-flight capable detectors for in-beam PET

To perform in-beam PET a detection system with specific properties is required. Concerning the geometrical configuration, a standard full-ring PET scanner is not applicable, cf. section 2.2. Double-head configurations are feasible as for instance installed at the GSI carbon ion facility (Enghardt et al., 2004). However, the limited solid angle coverage is followed by a low detection probability and artifacts compromising the image quality. For this reason, a PET camera with a sufficiently high time resolution which can improve the image quality substantially through the incorporation of TOF information into the MLEM procedure (Crespo et al., 2007; Shakirin, 2009) is desired. Especially, TOF-MLEM is advantageous in the presence of limited angle artifacts and a low number of coincidences, cf. section 2.2. The second relevant property is the dimension of the PET camera. Evidently, the heads of the scanner should be large enough to cover the ROI, but to avoid interferences with other equipment in the treatment bunker the PET camera should be of compact size. Furthermore, the applicability to clinical routine implies the safety of patients and clinical staff, i.e. the detector must neither be inflammable, poisonous, nor radioactive. Finally, the PET camera should consist of material which provides a detection probability sufficient for the inherently low activity in this application.

With RPCs a high time resolution is achievable. Further advantages of RPCs are the low production costs compared to scintillators and the possibility to build large-area detectors. RPCs are already suggested for whole-body diagnostic PET (Blanko et al., 2003; Crespo et al., 2012; Georgiev et al., 2013). The time resolution achievable by RPCs makes TOF-MLEM image reconstruction feasible, and, the potentially reachable CTR of 200 ps FWHM would even enable the image reconstruction with the Direct TOF procedure. Therefore, the evaluation of the abilities of an RPC-based PET camera dedicated to in-beam PET is reasonable. RPCs suffer from a low efficiency but, on the other hand, TOF-MLEM is known to compensate at a certain rate artifacts and low detection probabilities, cf. section 2.2. In this chapter an RPC-based PET camera dedicated to in-beam monitoring of particle therapy is studied with respect to efficiency, image quality, and its capability to detect range deviations. Distributions of annihilation points derived from real treatment plans are the basis for the simulations of detector response. The impact of the

incorporation of TOF information on the MLEM algorithm in terms of convergence and image quality is demonstrated for the considered RPC-based PET camera. Furthermore, the Direct TOF algorithm is applied in order to assess in which extent it is an alternative to the iterative algorithm TOF-MLEM for RPC-based detectors. Since scintillator-based PET cameras have been applied successfully to in-beam PET, a PET camera consisting of LYSO blocks, with a design based on a commercially available PET scanner, is used for a comparison with the investigated RPC-based PET camera.

5.1 Methods

5.1.1 Considered detectors

The detector configurations applied in this thesis are in line with the considerations of the Workpackage 2 of the ENVISION project. Parameters as geometry, materials, spatial resolutions, CTRs, as well as parts of the simulation code applied in this work were shared by the WP2-collaborators, this concerns the definitions of the detectors and the readout of the single events in the GATE simulations, and the criteria to filter the coincidences. Collaborators were David Watts (formerly TERA foundation), Irene Torres-Espellardo (formerly Institut de Fisika Corpuscular (IFIC)), and Faruk Diblen (formerly University of Ghent). Further details and results obtained in the framework of the Workpackage 2, e.g. regarding the RPC-based prototype and the evaluation of the sensitivity and the scatter fraction of RPC-based and crystal-based PET systems, can be found in recent publications (Diblen et al., 2012; Watts et al., 2013).

RPC-based PET camera

An RPC is a gas detector, consisting of thin resistive plates, e.g. glass or ceramic, which are altered by gaps filled with gas. Incoming photons interact in the plates and if a Compton scattering takes place, the Compton electron leaves the plate with a certain percentage. Due to a strong electric field, an electron avalanche is produced in the gas gap in direction towards the anode where a signal is induced. Using several resistive plates (multi-gap RPC) an even higher time resolution than with a single gap can be achieved (Cerron Zeballos et al., 1996). For clinical application, either for diagnostic PET or for PT-PET, RPCs are restricted to harmless gases, i.e. argon, CO_2, or Freon.

The in-beam PET camera based on RPCs that is investigated in the following is an optimized version of the experimental detector-module studied at TERA (Watts et al., 2013) and was recommended by David Watts. Each of the two parts of the detector consists of 7 heads, cf. figure 5.1, where each of these heads is built up from 60 modules of multi-gap RPCs. The detector modules are build up from 5 layers of glass which are 0.15 mm

thick and have a total dimension of 12 cm $\times$ 60 cm $\times$ 1.95 mm. The 0.3 mm thick gaps in-between the glass plates are filled with Freon ($C_2F_4H_2$). The modules are separated by 2.05 mm empty space. Consequently, in total, the height of one head consisting of 60 modules is 24 cm. The heads are arranged in two parts of a ring with 76.67 cm diameter so that each part covers an angle of 126 degrees. The spatial resolution is assumed to be a Gaussian distribution with 2 mm FWHM in *x*- and 4 mm FWHM in *y*-direction. A CTR of 300 ps FWHM was reported for photons (Blanco et al., 2003). Expecting further improvements, for the simulations in this thesis CTRs of 100 and 200 ps FWHM are applied.

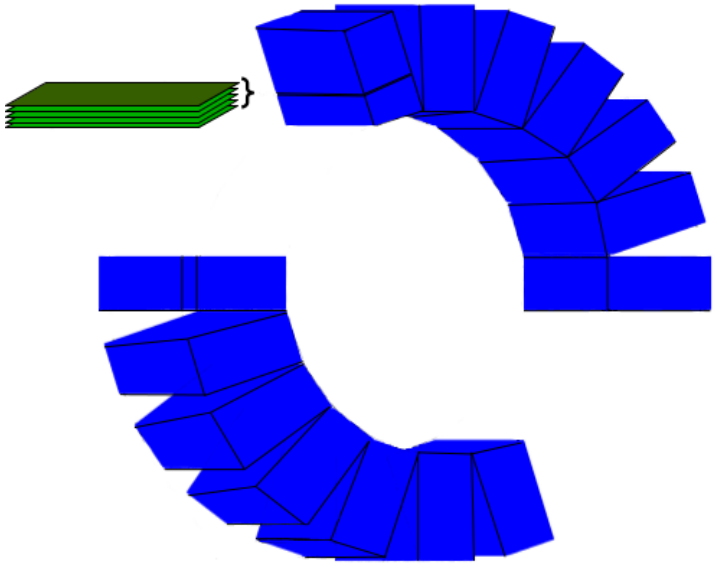

Figure 5.1: RPC-based partial-ring PET camera under consideration. Both parts of the detector consist of 7 heads, where each of these heads is built up from 60 modules of multi-gap RPCs with 5 resistive plates.

Crystal-based PET camera: reference detector

PET cameras made of scintillators are proven feasible for PT-PET (e.g. Enghardt et al., 2004). To compare the results obtained with the RPC-based PET camera to a crystal-based one, a camera relying on the currently available Philips GeminiTF is considered. The GeminiTF is built up from LYSO-crystals ($4 \times 4 \times 22$ mm^3) and reach a CTR of 585 ps FWHM (Surti et al., 2007). The crystals are mounted on 28 modules with 23×44 crystals per module. Since the original axial length of 18 cm can be shorter than irradiation fields, it is extended to 40 cm in this study, i.e. the modules are extended from 23×44 to 23×98 crystals. Thus, the axial length is still considerably smaller than the axial dimension of the investigated RPC-based camera. The diameter of the crystal-based scanner is 90 cm. To obtain a partial-ring scanner with similar solid angle coverage as the RPC-based PET

camera under investigation, 8 of the 28 paddles of crystal blocks are removed for the simulations. Beside the currently achievable CTR of 600 ps FWHM, CTRs of 400 and 200 ps FWHM were tested to take into account future developments.

5.1.2 Patient data to be used as a basis in the simulations

To evaluate the two types of detector systems with respect to in-beam PET application it is mandatory to study real patient data. For this reason, simulated data based on real treatment plans from the pilot study at the carbon ion facility at GSI were used as a basis for the simulation.

Within the pilot study at GSI, patients with head and neck tumors were treated with carbon ion beams (^{12}C) (Jäkel et al., 2005). In order to evaluate the PT-PET measurements conducted at GSI, Monte carlo simulations of the β^+-activity were performed according to the treatment plan (Enghardt et al., 2004). This simulation was performed with an inhouse code (Hasch, 1996; Pönisch et al., 2004). It calculates first the production of β^+-emitting nuclei arising from the irradiation. In the next step, the decay of these nuclei, the propagation and annihilation of the positrons, and, finally, the detection of the annihilation photons were modeled with that code. Then, the reconstructed images obtained on the one hand from the PT-PET measurements and on the other hand by means of these predictions were compared to each other. In this chapter, the distributions of annihilation points (annihilation maps) modelled with the simulation code described above are used, since these distributions represent realistic sources. The annihilation maps are provided by Dr. Fine Fiedler (HZDR).

Randomly, data of two patients with tumors at the skull base are chosen. The first one (Patient 1) was diagnosed with a chordoma and treated with 0.829 Gy in a unique field in each fraction. Another patient (Patient 2) suffered from a clival chondrosarcoma and received 0.662 Gy per fraction in one of two fields. At GSI, PT-PET measurements were performed during the beam extraction pauses due to the time structure of the synchrotron. Therefore, for this study exclusively the positron emitters ^{15}O, ^{14}O, ^{13}N, ^{11}C, and ^{10}C are taken into account due to their half-lives, where the total number of annihilation points is additionally reduced according to the length of the extraction pauses. As a consequence, the realistic numbers of annihilations used as a basis for the GATE simulation of the detector response are $3.7 \cdot 10^5$ and $2.7 \cdot 10^6$ for the two patients, respectively.

Figures 5.2 and 5.3 show the dose distributions according to the treatment plan and the distributions of the simulated annihilation points for Patient 1 and Patient 2. All images are superimposed on the corresponding CT scans. The annihilation maps have dimen-

sions of $287 \times 287 \times 267\,\mathrm{mm}^3$ and $310 \times 310 \times 306\,\mathrm{mm}^3$, respectively. They are centered around the corresponding isocenters and the voxels have the size $1 \times 1 \times 1\,\mathrm{mm}^3$. In these images all annihilation points in a 1 cm thick slice around the isocenter are depicted.

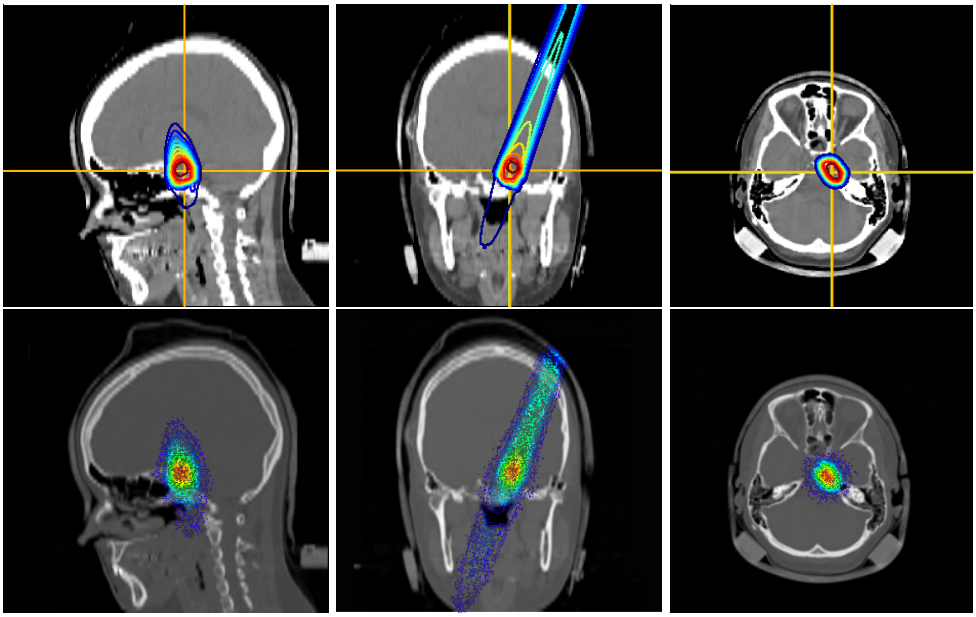

Figure 5.2: Therapeutic irradiation with carbon ions (Patient 1). Upper row: planned dose in sagittal (left), frontal (center), and transversal view (right). The yellow lines indicate the isocenter. Lower row: simulated distribution of annihilation points in a 1 cm thick slice around the isocenter in sagittal (left), frontal (center), and transversal view (right).

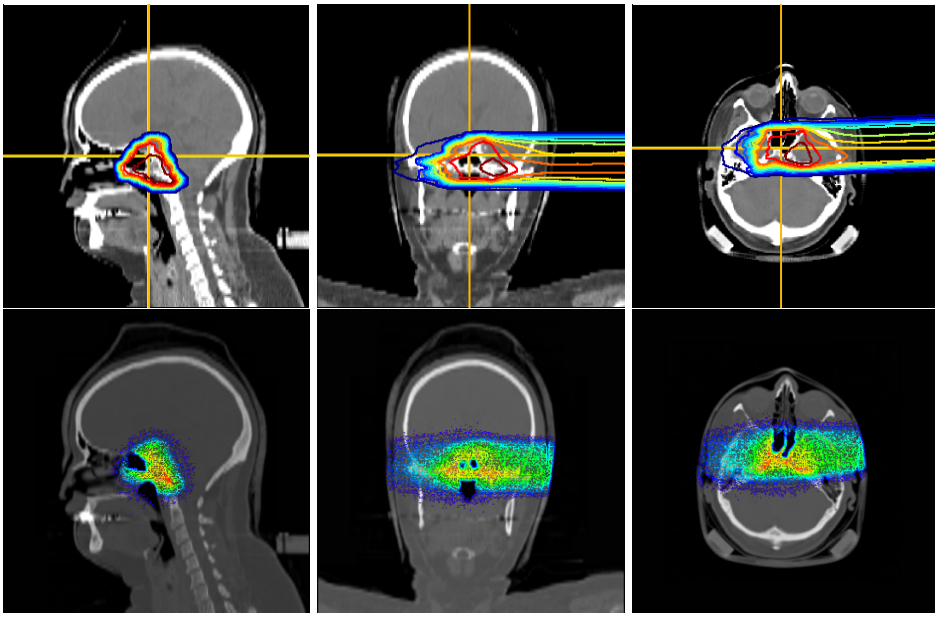

Figure 5.3: Therapeutic irradiation with carbon ions (Patient 2). Upper row: planned dose in sagittal (left), frontal (center), and transversal view (right). The yellow lines indicate the isocenter. Lower row: simulated distribution of annihilation points in a 1 cm thick slice around the isocenter in sagittal (left), frontal (center), and transversal view (right).

5.1.3 Simulation of the detector response with GATE

The simulation of the detector response is performed with the GEANT4 derivative GATE, version 6.1 (Jan et al., 2011). GATE is applied due to its user-friendly features regarding the modelling of a PET scanner, the readout of the energy depositions in the detector system, and the incorporation of human tissue. The schematic drawing in figure 5.4 shows the arrangement of the patient's head in the partial-ring PET camera configuration as modelled in the GATE simulations. By means of GATE the single events, i.e. the energy depositions in the detector, in combination with the corresponding detection positions and the corresponding time stamps, are provided. In detail, for the RPC-based PET camera all electrons are counted which reach the gap filled with gas. Since in reality not every electron induces a signal and, thereby, corresponds to an event, the rate of single events is overestimated but corrected later on, cf. subsection 5.1.4.

The simulated annihilation maps are included as sources into the GATE simulation. With GATE annihilation photons can be modeled as so-called *back-to-back* photons. These two photons are emitted simultaneously to opposed directions. Thus, the deviation from the 180 degree angle that results from the movements of the positrons is not taken into account. Since only the irradiation of one field for each patient is considered for the

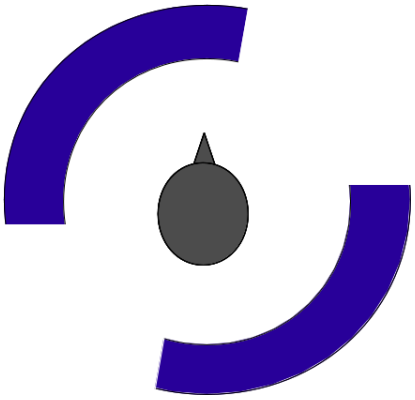

Figure 5.4: Transversal view of the patient laying inside the partial-ring PET cameras as modelled by means of GATE.

GATE simulations, the irradiation time is set to 3 minutes. Using the so-called *voxelized source* in GATE, the activity needs to be provided to ensure that the correct number of annihilation photons is emitted in the defined irradiation time. In the annihilation maps, in each voxel of dimension $1 \times 1 \times 1\,\mathrm{mm}^3$ the total number of annihilations from this voxel is given. Therefore, by means of the *rangetranslator-file* (OpenGATEcollaboration, 2014), each voxel value is scaled from the total number of annihilations to the corresponding activity / Bq.

The patient's tissue is modelled using the original CT scans of the patients. With GATE it is possible to convert the Hounsfield units (HU) given by the CT scan to the density and material of human tissue. First, the CT scan has to be provided in the *AnalyzeTM*-format to make it readable by GATE (OpenGATEcollaboration, 2014). From the HUs, the corresponding material is deduced by means of a calibration file (Schneider et al., 2000), which need to be provided by the user. Furthermore, the calibration file specific for the applied CT scanner indicating the relations between HUs and mass density is required (OpenGATEcollaboration, 2014). The aim of the incorporation of the patient's tissue is the determination of the efficiency of the considered PET camera configurations for realistic scenarios. By using the human tissue in the simulation, the attenuation of the annihilation photons in the material is taken into account, and, thus, realistic numbers of coincidences are obtained. In principle, if tissue or a phantom is modeled, corrections regarding attenuation and scattering are needed for the image reconstruction. Since the aim of this study is not the optimization of these corrections, the simulated events which are used as input for the image reconstruction are obtained without using a phantom but in air. Thus, the number of coincidences used for reconstruction is set according to the efficiency derived for each camera with the human tissue included.

For the crystal-based scanner the number of coincidences obtained this way underesti-

mates the actual efficiency proven by experiments (Surti et al., 2007) due to the readout mode of the single events. GATE provides block-wise and crystal-wise readout for PET cameras, but, unfortunately, the readout scheme of the GeminiTF is more complex. Using the crystal-wise readout mode, the efficiency is underestimated for this camera by a factor of 1.646 according to recent results obtained by Irene Torres-Espellardo (formerly IFIC). Therefore, the number of coincidences obtained for the crystal-based PET camera by means of GATE simulations is corrected according to this factor.

The GATE simulations result in a list of single events. GATE users can chose between two output formats: text-files and root-files. Due to a considerable smaller size, the root-file output is chosen. For this study the GATE simulations return the exact time stamps of the single events, the filtering of the coincidences and the incorporation of time blurring is performed in a post-processing step, cf. subsection 5.1.4.

5.1.4 Filtering of the coincidences from single events

A pair of single events is considered as coincidence, if the following criteria regarding the detection positions, the time stamps, and the values of energy depositions are fulfilled. The first coincidence condition claims that one photon is registered in one head of the partial-ring scanner and the second photon in the other one. This is aimed at the neglection of scattered photons and random coincidences. This condition is fulfilled by true coincidences, since the annihilation maps are placed at the center of the camera. Secondly, another necessary condition for a pair of single events is the compliance with the time window. For the crystal-based PET camera an interval of 3.8 ns is used as coincidence window and 1 ns for the RPC-based camera. Furthermore, single events are filtered according to an energy window. For the crystal-based scanner the energy window is [440 keV, 665 keV] as applied for the GeminiTF (Surti et al., 2007). This limitation concerning the energy deposition also helps to reduce the rate of scattered events. For the RPC-based PET camera a cut of 0.1 keV is applied, since with that cut the experimentally achieved sensitivity is reproduced (according to results obtained by Irene Torres-Espellardo, formerly IFIC). Finally, the time stamps of the coincident events are modified according to the time resolution. For the crystal-based PET camera CTRs of 200, 400, and 600 ps FWHM are applied and for the RPC-based PET camera 100 and 200 ps FWHM.

5.1.5 Reconstruction methods

For the reconstruction three different methods are applied: MLEM (equation (2.4)), the TOF-MLEM method (equation (2.8)), and the Direct TOF procedure (following equa-

tion (2.7)). The Direct TOF method is predominantly relevant for the RPC due to the assumed excellent CTRs. It is tested whether with the Direct TOF algorithm the same image quality as with the TOF-MLEM can be achieved for RPCs. The implementation of these reconstruction algorithms from a previous thesis (Shakirin, 2009) is applied but modified with respect to the calculation of the system matrix for the RPC-based detector and the input of coincidences given in a root-file.

The system matrix in this implementation used for the MLEM and the TOF-MLEM is derived on-the-flight: the necessary components of the system matrix are calculated when they are needed. Ten channels link the detection positions and the thereby affected voxels are considered for the system matrix. During the iterations the activity is distributed along these lines. The ten channels are also used for the Direct TOF method to find the voxel in which most probably the annihilation has taken place. Since the original version of the code was exclusively dedicated to crystal-based detectors, the determination of the channels is based on the random distribution of the end points of the channels on the two crystals in which the event was registered (Shakirin, 2009). The uncertainty of the depth-of-interaction in the crystals was not taken into account. In the extended version of the code the reconstruction for the RPC-based PET camera is included by making use of the simulated detection positions: the end points of the ten channels are distributed around them using a Gaussian blurring according to the spatial resolution of the RPCs in *x*- and *y*-direction.

Prior to the start of the reconstruction, the detection probability for each voxel, i.e. the probability for an emission from this voxel to be detected by the camera, is derived by simulations. This precalculation is performed for each camera configuration. The detection probability for voxel $j,\ j = 1, ..., M$ is used instead of $\sum_{i=1}^{N} a_{ij}$ in the equations (2.4) and (2.8) and is also applied for the Direct TOF procedure to correct for the geometrical design of the camera.

After every iteration a median filtering is applied to smooth the image. This filter replaces the value of one voxel by the median value of this voxel and the 26 neighboring ones. This filtering is highly recommended to reduce noise (Shakirin, 2009).

One important parameter concerning the reconstruction algorithm is the voxel size. In this study, one voxel has the dimension $2 \times 2 \times 2\,\text{mm}^3$. This dimension is chosen in accordance with a previous study of the impact of the voxel size on the image quality (Shakirin et al., 2008). Furthermore, due to the low number of coincidences inherent to the studied patient scenarios and the efficiency of the RPC-based camera, it can be expected that a smaller voxel size than 2 mm would lead to considerably worse image quality.

In addition to that, the optimal number of iterations for the MLEM and the TOF-MLEM procedure needs to be determined. For this, the RMSE is calculated up to the tenth iteration of the MLEM and the TOF-MLEM for both PET cameras and both patients, to assess the improvement in each iteration step. Due to the obtained results, cf. section 5.2, the iteration is stopped after ten repetitions.

5.1.6 Detection of range deviations with YaPET

A crucial point in the evaluation of the considered PET cameras is to test their abilities with respect to the detection of range deviations. For this reason, further annihilation maps including range shifts are generated (Dr. Fine Fiedler / HZDR) and used as bases for additional GATE simulations of detector response. These range deviations correspond to variations of the energy of the beam. In the shape of a frustum of a pyramid, which is 2 cm wide and aligned in beam direction, energy is reduced and increased, respectively, by 6 energy steps (ES). One energy steps equals 1 mm range deviation in water. This method had been used before (Fiedler et al., 2010; Helmbrecht et al., 2012).

The reconstructed images are investigated by visual inspection and with YaPET (Yet another PET Evaluation Tool) which is a semi-automatic software aimed at the detection of range deviations (Helmbrecht et al., 2012; Helmbrecht et al., 2014). With YaPET two images can be analyzed at the same time and compared to each other by considering one-dimensional activity profiles along the beam direction and a distribution of range deviations can be provided. To achieve this, YaPET calculates the distal fall-offs from the one-dimensional activity profiles, since the fall-offs can be correlated to the range (Helmbrecht et al., 2012).

Before using YaPET, the images obtained for the original and the modified annihilation maps needed to be transformed to the data format applied at GSI for PT-PET, which corresponds to the dimensions of the CT scan. By interpolating the image values, images with voxel sizes of $1.12 \times 1.12 \times 3\,\mathrm{mm}^3$ and $1.21 \times 1.21 \times 3\,\mathrm{mm}^3$ for Patient 1 and Patient 2, respectively, were generated. The rotation of the voxel grid to the beam direction is done automatically by YaPET using the corresponding files containing the treatment plan. For this study the images are reconstructed with the TOF-MLEM algorithm using CTRs of 600 ps FWHM for the crystal-based PET camera and 100 ps FWHM for the RPC-based PET camera, where the CTR for the crystal-based camera is realistic and the CTR for the RPC-based camera was not yet achieved.

5.2 Results

5.2.1 Efficiency of the detectors

Table 5.1 lists the efficiency of the crystal-based and the RPC-based partial-ring PET camera under consideration using the annihilation maps of Patient 1 and Patient 2 as obtained by means of the performed GATE simulations. The observed efficiency of the RPC-based PET camera is more than three times lower than the efficiency of the crystal-based PET camera using the crystal-wise readout. By multiplying the number of coincidences obtained with the crystal-based PET camera with the factor 1.646 in order to obtain realistic values, the efficiency differs by a factor of about 5.5 with respect to the RPC-based PET camera. The corrected number of coincidences is applied for the reconstruction of the images.

Table 5.1: Number of coincidences obtained by GATE simulations for the RPC-based PET camera and the crystal-based PET camera using the annihilation maps from Patient 1 and Patient 2. For the crystal-based PET camera the numbers of coincidences used for the reconstruction are given in brackets, it is corrected regarding the disagreement between simulated and experimentally obtained efficiency.

Patient	RPC-based	Crystal-based
Patient 1	1014	3321 (5466)
Patient 2	6840	25252 (41565)

5.2.2 Quality of reconstructed images

Reconstructed images obtained for the RPC- and the crystal-based PET cameras with 10 iterations of the TOF-MLEM algorithms are depicted in figure 5.5 for Patient 1 and in figure 5.6 for Patient 2. As expected due to the higher efficiency, a better agreement with the reference images is provided for the crystal-based PET camera than for the RPC-based PET camera, in particular with respect to the position and the extend of the hot region. Concerning the RPC-based camera, only in the case of Patient 1 and a CTR of 100 ps a quite accurate activity distribution is reconstructed, the hot spot at the isocenter is clearly visible. For the crystal-based scanner smooth distributions are obtained with all considered CTRs. For Patient 1, even no substantial differences between the images generated with the crystal-based PET camera for the applied CTRs of 200, 400, and 600 ps FWHM can be recognized. For Patient 2 the activity distributions gets broader with worse time resolution.

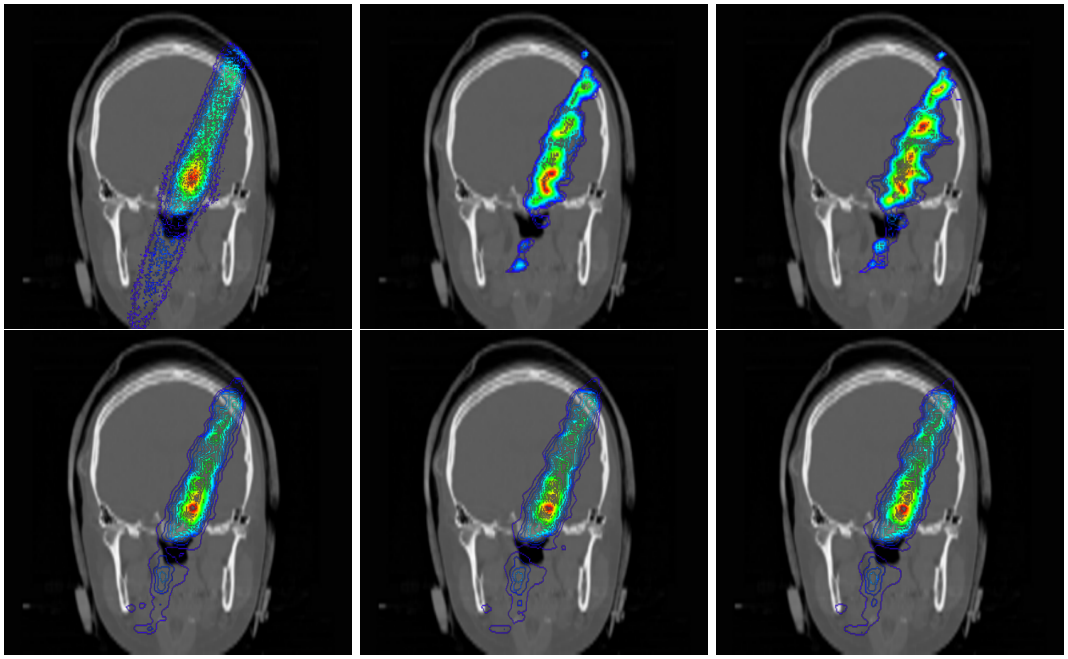

Figure 5.5: Comparison between the reconstructed images for Patient 1 (frontal view) obtained for the RPC-based PET camera and the crystal-based PET camera with 10 iterations of the TOF-MLEM algorithm. First row: reference image (distribution of annihilation points) (left), reconstructed images for the RPC-based camera with a CTR of 100 ps FWHM (center), and 200 ps FWHM (right). Second row: reconstructed images for the crystal-based camera with a CTR of 200 ps FWHM (left), 400 ps FWHM (center), and 600 ps FWHM (right). For these images a 20 mm thick slice containing the isocenter is taken into account.

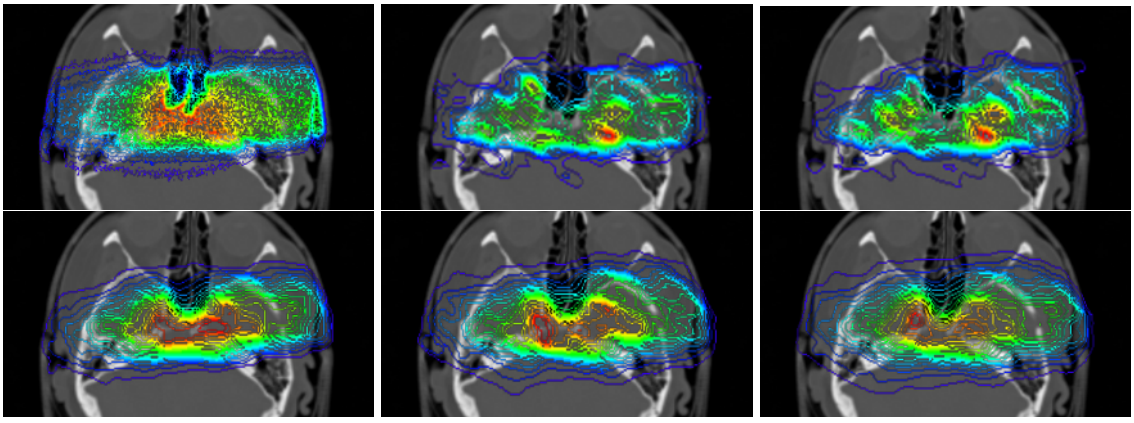

Figure 5.6: Comparison between the reconstructed images for Patient 2 (transversal view) obtained for the RPC-based PET camera and the crystal-based PET camera with 10 iterations of the TOF-MLEM algorithm. First row: reference image (distribution of annihilation points) (left), reconstructed images for the RPC-based camera with a CTR of 100 ps FWHM (center), and 200 ps FWHM (right). Second row: reconstructed images for the crystal-based camera with a CTR of 200 ps FWHM (left), 400 ps FWHM (center), and 600 ps FWHM (right). For these images a 20 mm thick slice containing the isocenter is taken into account.

5.2.3 Influence of the incorporation of TOF on the MLEM algorithm

Figures 5.7 and 5.8 depict reconstructed images which are the result of the standard MLEM and the TOF-MLEM procedure. The positive impact of TOF is especially obvious for the reconstruction of the data obtained with the RPC-based camera. Elongation artifacts, i.e. stretching of the activity towards the heads of the PET camera, appear in images obtained with the MLEM, but not if the TOF-MLEM reconstruction is applied for the RPC-based camera. These artifacts are highlighted by arrows in figures 5.7 and 5.8. For the crystal-based PET camera the impact of TOF information on the reconstruction results is not visible at all for Patient 1. For Patient 2 for both types of cameras the distribution is more compact if the reconstruction is performed with the TOF-MLEM instead of the MLEM.

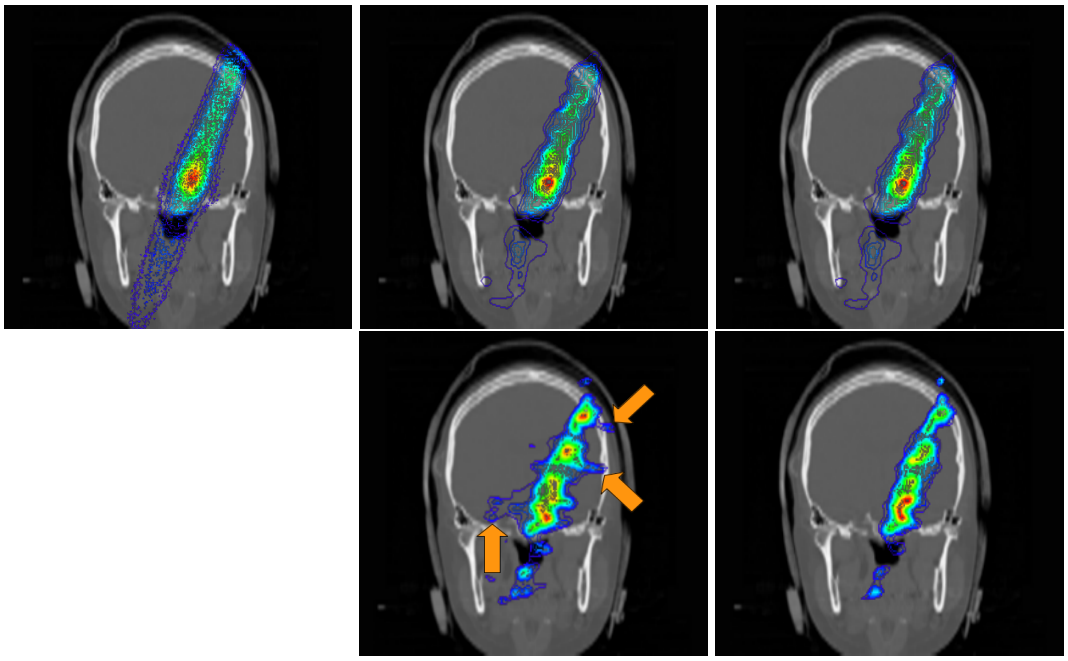

Figure 5.7: Comparison of images reconstructed with MLEM or TOF-MLEM for Patient 1: First row: reference image (distribution of annihilation points) (left), MLEM reconstruction for the crystal-based camera (center), TOF-MLEM reconstruction with 600 ps FWHM (right). Second row: MLEM reconstruction for the RPC-based camera (center) with artifacts indicated by orange arrows, TOF-MLEM reconstruction with 100 ps FWHM (right). For these images a 20 mm thick slice containing the isocenter is taken into account.

Furthermore, the influence of the incorporation of TOF into the MLEM algorithm is assessed with respect to the convergence of the reconstruction procedure. Figure 5.9 shows the RMSE indicating the convergence of the MLEM and TOF-MLEM for both types of detectors. The impact of TOF, i.e. additional information of the place of annihilation, on the convergence is obvious. Most effect is evident for both cameras and both patients for

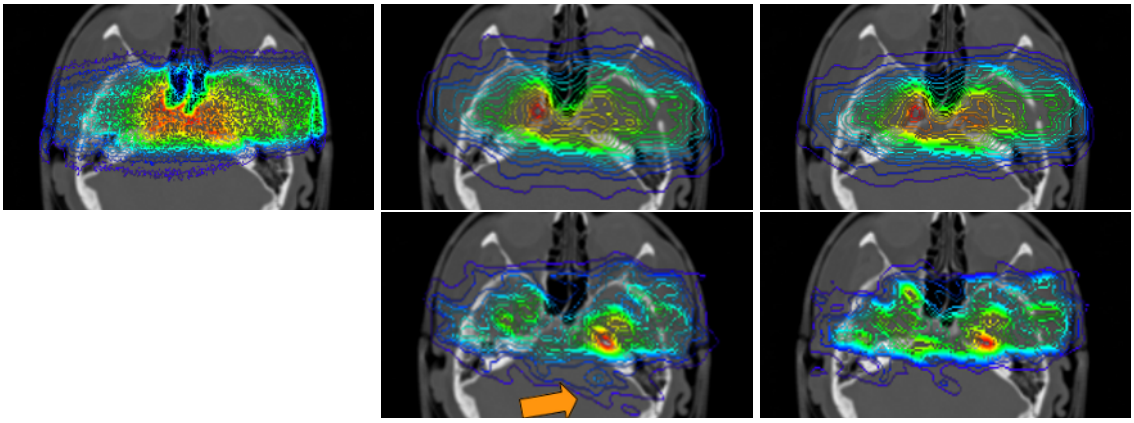

Figure 5.8: Comparison of images reconstructed with MLEM or TOF-MLEM for Patient 2: First row: reference image (distribution of annihilation points) (left), MLEM reconstruction for the crystal-based camera (center), TOF-MLEM reconstruction with 600 ps FWHM (right). Second row: MLEM reconstruction for the RPC-based camera (center) with an artifact indicated by an orange arrow, TOF-MLEM reconstruction with 100 ps FWHM (right). For these images a 20 mm thick slice containing the isocenter is taken into account.

the first iteration. While for the crystal-based scanner the same level of accuracy in terms of RMSE is reached for MLEM and TOF-MLEM after the third iteration, this is not the case for the RPC-based PET camera up to the tenth iteration. In total, the effect of the TOF information on the convergence is higher for the RPC-based PET camera. This can be explained by the lower efficiency and, secondly, by the higher scatter fraction observed for the RPC-based PET camera in comparison with the crystal-based PET camera (Diblen et al., 2012)

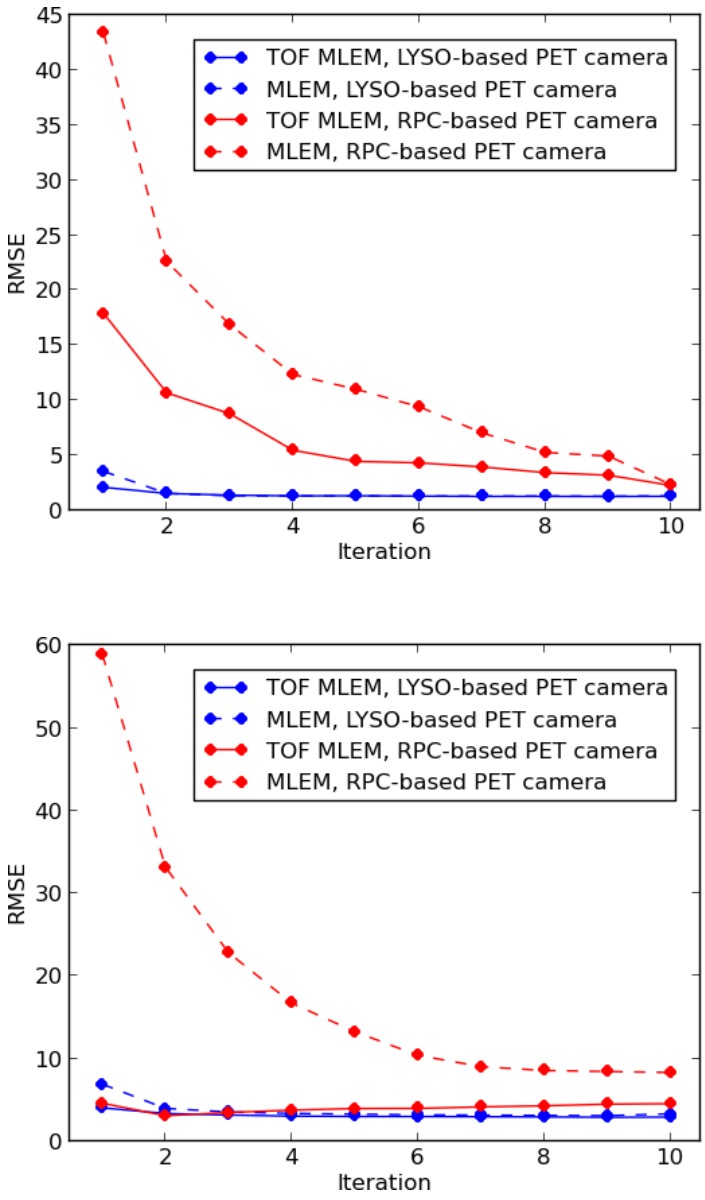

Figure 5.9: RMSE for the reconstructed images as a function of the iteration for Patient 1 (top) and Patient 2 (bottom). The original annihilation maps are used as reference. The TOF-MLEM and the MLEM are applied. A CTR of 200 ps FWHM is considered.

5.2.4 Direct TOF versus TOF-MLEM

In order to assess the Direct TOF method for the RPC-based PET camera, images obtained with the TOF-MLEM on the one hand and the Direct TOF algorithm on the other hand are presented in the figures 5.10 and 5.11. Furthermore, figure 5.12 depicts the RMSE for all three reconstruction methods as a function of the applied CTR. For the MLEM and the TOF-MLEM the tenth iteration is used. While the activity distribution in the images obtained with the Direct TOF procedure is broadened and appear more fragmented compared to the images obtained with the TOF-MLEM method, the image quality in general seems not to be significantly worse. This is confirmed with the values of the RMSE in figure 5.12. The Direct TOF method provides artifact free reconstruction as the TOF-MLEM. In addition to that, in case of Patient 1 and the RPC-based PET camera with an assumed CTR of 200 ps FWHM the hot spot is even reproduced well if the Direct TOF method is applied in contrast to the image resulting from the TOF-MLEM algorithm, cf. figure 5.11.

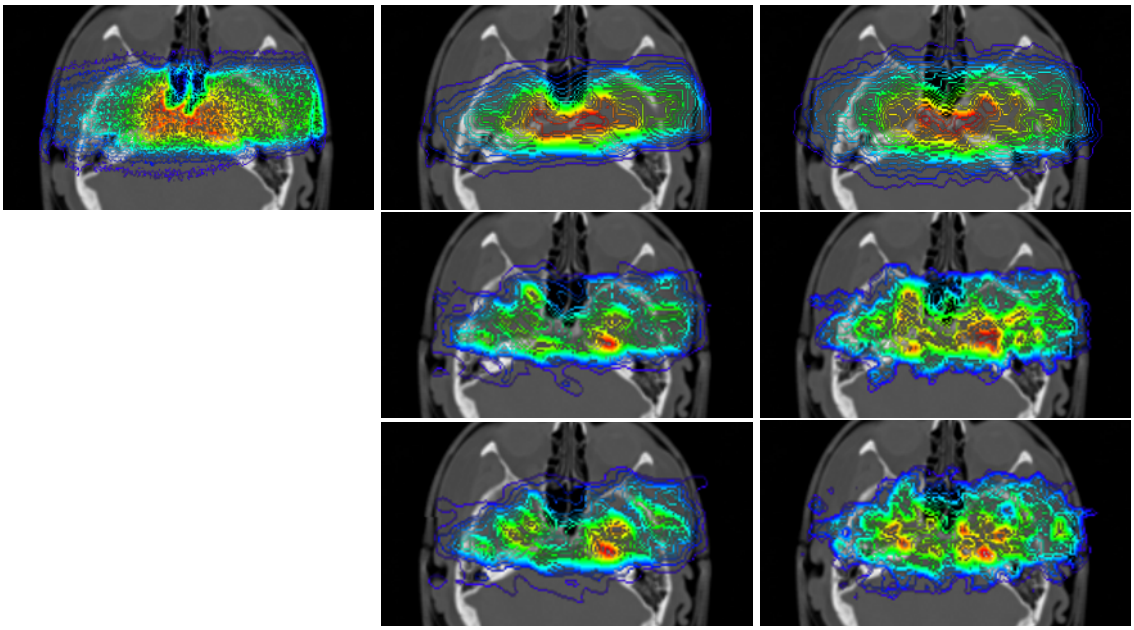

Figure 5.10: Comparison between images obtained with TOF-MLEM (center) and Direct TOF (right) for Patient 2. Upper row: reference image (left), reconstructed images obtained with the crystal-based PET camera with a simulated CTR of 200 ps using the TOF-MLEM (center), and the Direct TOF (right). Central row: reconstructed images obtained with the RPC-based PET camera with a simulated CTR of 100 ps using the TOF-MLEM (center) and the Direct TOF (right). Lower row: reconstructed images obtained with the RPC-based PET camera with a simulated CTR of 200 ps using the TOF-MLEM (center) and the Direct TOF (right). For these images a 20 mm thick slice containing the isocenter is taken into account.

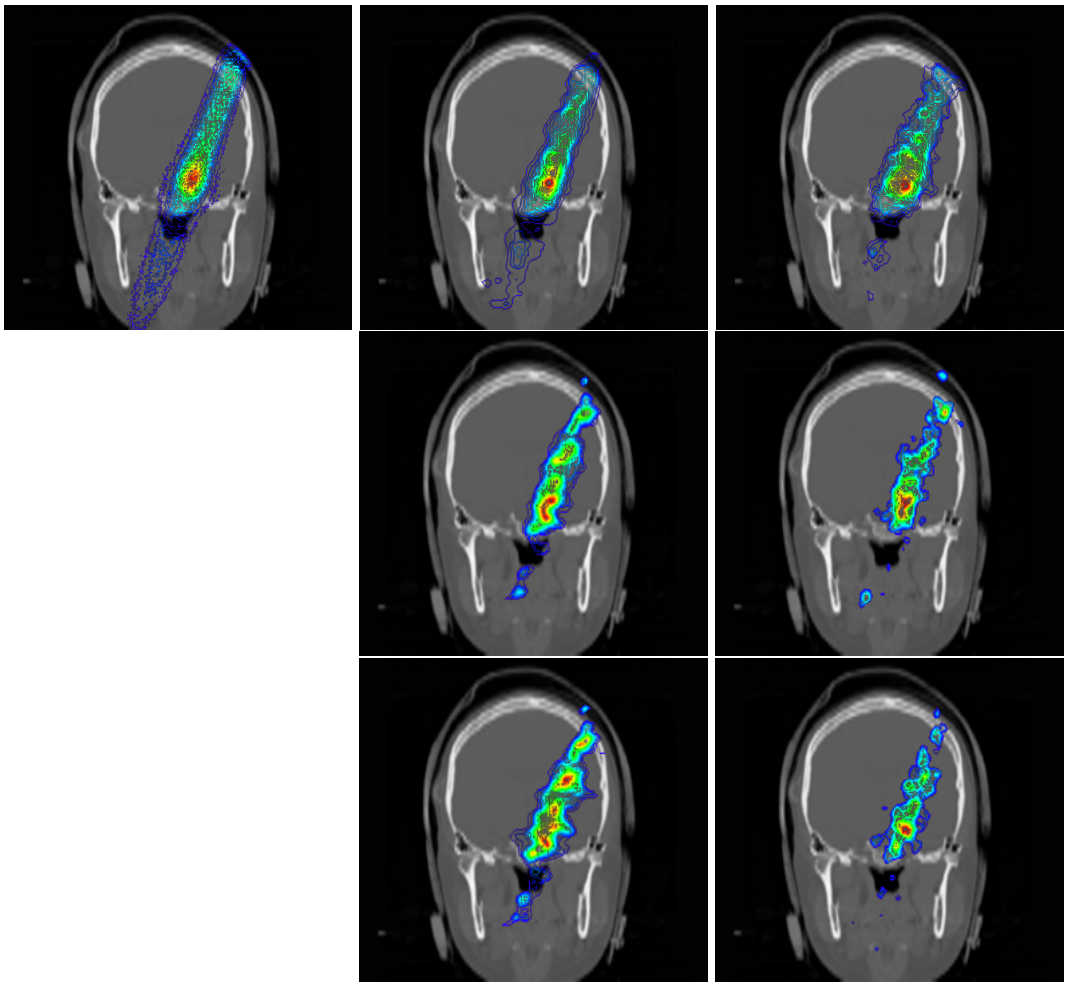

Figure 5.11: Comparison between images obtained with TOF-MLEM (center) and Direct TOF (right) for Patient 1. Upper row: reference image (left), reconstructed images obtained with the crystal-based PET camera with a simulated CTR of 200 ps using the TOF-MLEM (center), and the Direct TOF (right). Central row: reconstructed images obtained with the RPC-based PET camera with a simulated CTR of 100 ps using the TOF-MLEM (center) and the Direct TOF (right). Lower row: reconstructed images obtained with the RPC-based PET camera with a simulated CTR of 200 ps using the TOF-MLEM (center) and the Direct TOF (right). For these images a 20 mm thick slice containing the isocenter is taken into account.

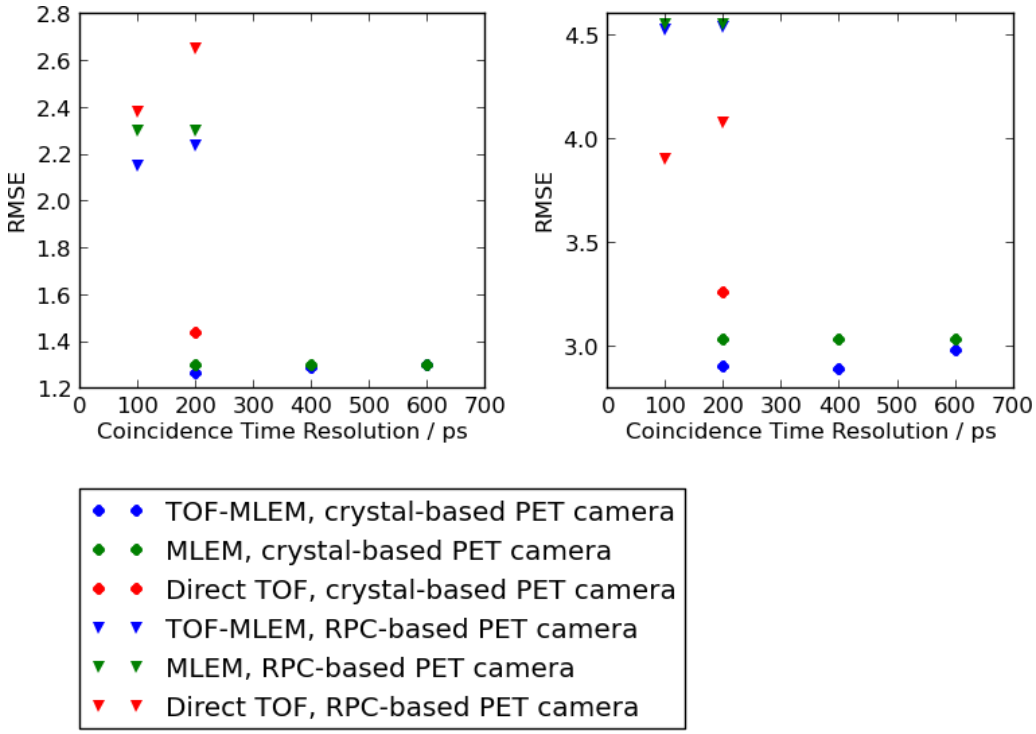

Figure 5.12: RMSE of the reconstructed images obtained with different reconstruction methods for the crystal-based PET camera and the RPC-based PET camera for Patient 1 (left) and Patient 2 (right). The original annihilation map is used as reference. The MLEM and the TOF-MLEM algorithms are stopped after the tenth iteration.

5.2.5 Detectability of range deviations

In figures 5.13 and 5.14 the reconstructed images obtained for the modified annihilation maps which include range shifts are shown using the RPC-based and the crystal-based PET camera. As references, the distributions of annihilation points and the reconstructed images for the original annihilations maps are used, which are depicted as well. For Patient 1 the direction of the range variations are clearly visible in the images obtained for the crystal-based PET camera following the hot spots. Likewise, for Patient 2, the distribution of annihilation points is reproduced accurately enough to detect the range shift, especially by focusing on the appearance of the hot region in comparison to the corresponding annihilation maps. In contrast to this, for the RPC-based PET camera the visualization of range shifts is not clearly successful in any of the four cases. For Patient 2 at least the changes behind the distal fall-offs agree with the original distributions. However, the positions of the hot spots are not true and prohibit a definite statement.

Secondly, an analysis by means of YaPET is performed using these reconstructed images as input, cf. figure 5.15. The histograms obtained with YaPET quantifying the range deviations are analysed for the shape of the distribution and the sum of found range deviations in negative direction in comparison to the positive direction. If there were no range shifts, the distribution provided by means of YaPET would be symmetric and centered at 0. Since the energy shifts do not affect the complete volume of interest but the 2 cm wide frustum of a pyramid in the isocenter, a single peak cannot be expected in this YaPET analysis which takes into account the complete volume of interest. To demonstrate the abilities of YaPET, the comparison of range deviations is also performed with the annihilation maps directly. For the RPC-based camera YaPET gives a hint for the shift in negative direction for Patient 1, and for the positive direction at least the maximum of the curve is on the positive side of the x-axis. For Patient 2 the actual range shifts are not identified with YaPET at all. In contrast to this, for the crystal-based camera YaPET returns clear results, i.e. the histograms present distributions of range deviations skewed to the correct direction.

Table 5.2 summarizes the results concerning the detectability of range deviations for the two types of PET cameras under study and the two patient cases. In total, concerning the RPC-based PET camera, the obtained image quality makes the decisive recognition of range deviations either by visual inspection or by using YaPET difficult. On the contrary, for the crystal-based camera, the range deviations are visible from the reconstructed images and confirmed with YaPET.

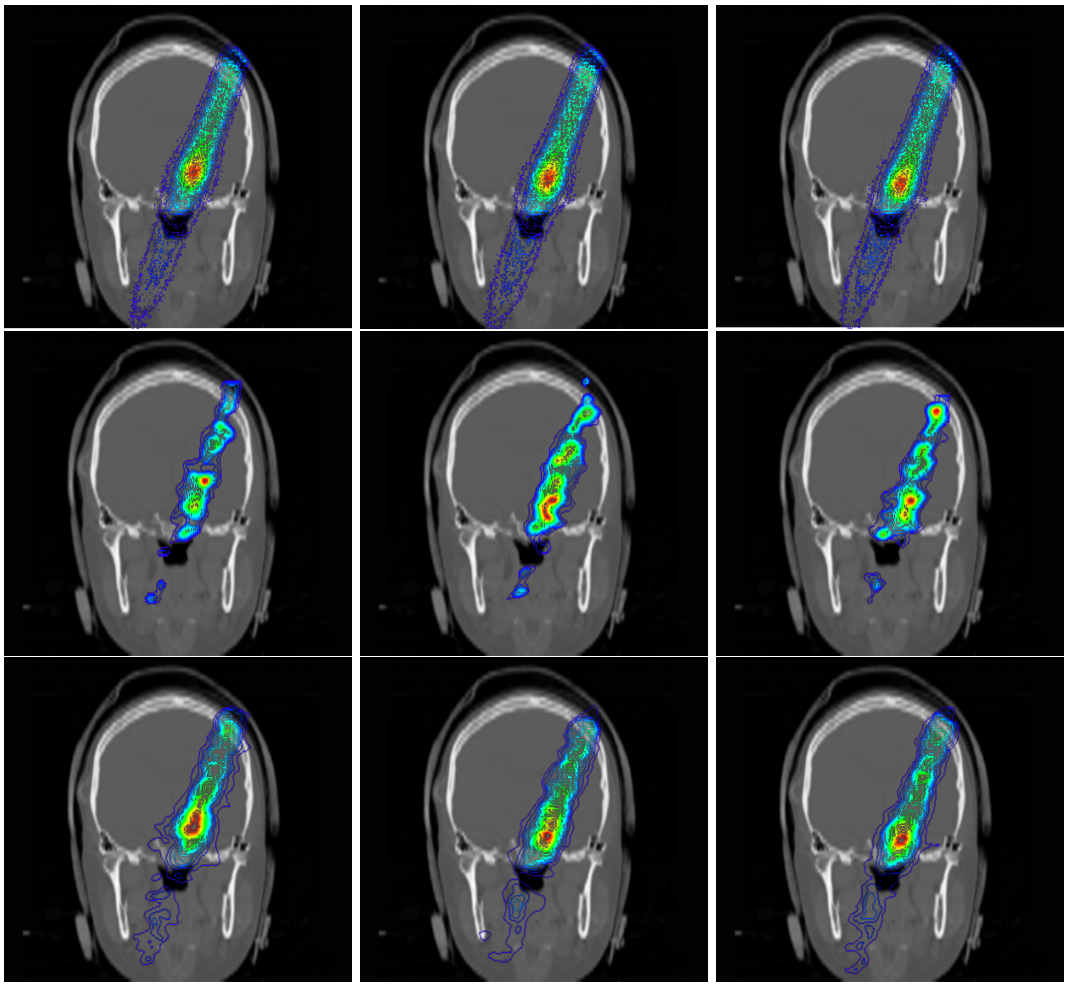

Figure 5.13: Range deviations for Patient 1 (frontal view). Annihilation maps (top) and reconstructed images for the RPC-based PET camera (center) and the crystal-based PET camera (bottom) with range deviations of -6 ES (left), ±0 ES (center), and +6 ES (right). For these images a 20 mm thick slice containing the isocenter is taken into account.

Table 5.2: Detectability of range deviations for the two patients and the range shifts of 6 ES in the positive and the negative direction. The reconstructed images obtained for the RPC-based PET camera and the crystal-based PET camera, cf. figures 5.13, 5.14 are analysed by visual inspection and with the semi-automatic tool YaPET, cf. figure 5.15. For the RPC-based PET camera a CTR of 100 ps and for the crystal-based camera a CTR of 600 ps is assumed.

		RPC-based		crystal-based	
Patient	Shift	Visual	YaPET	Visual	YaPET
1	+6 ES	no	?	yes	yes
	-6 ES	no	yes	yes	yes
2	+6 ES	?	no	yes	yes
	-6 ES	?	no	yes	yes

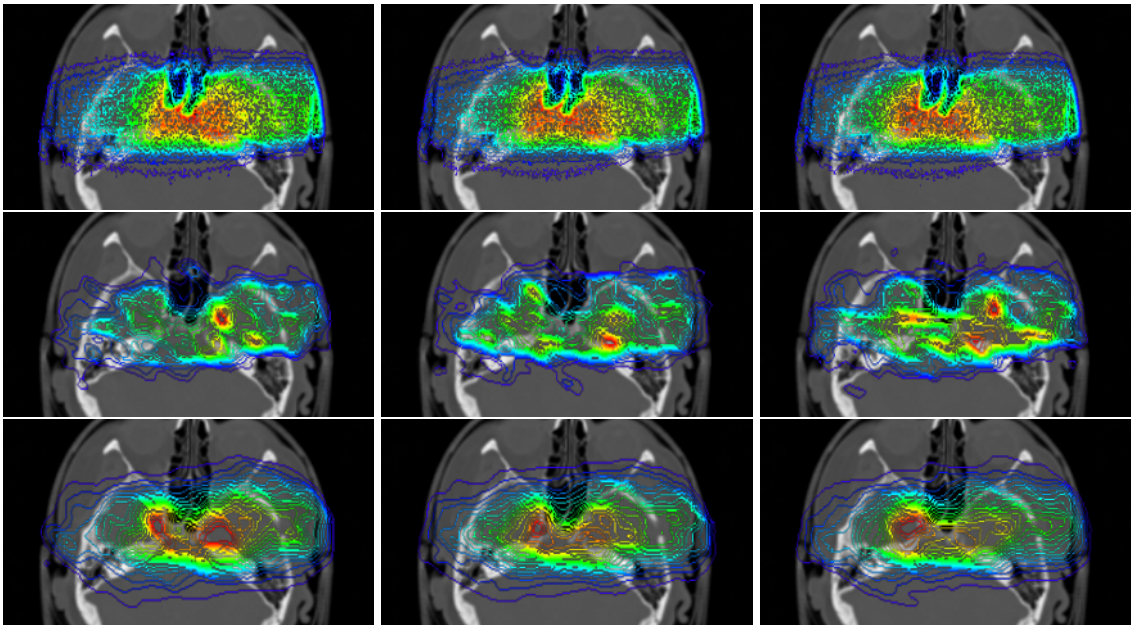

Figure 5.14: Range deviations for Patient 2 (frontal view). Annihilation maps (top) and reconstructed images for the RPC-based PET camera (center) and the crystal-based PET camera (bottom) with range deviations of -6 ES (left), $\pm$0 ES (center), and +6 ES (right). For these images a 20 mm thick slice containing the isocenter is taken into account.

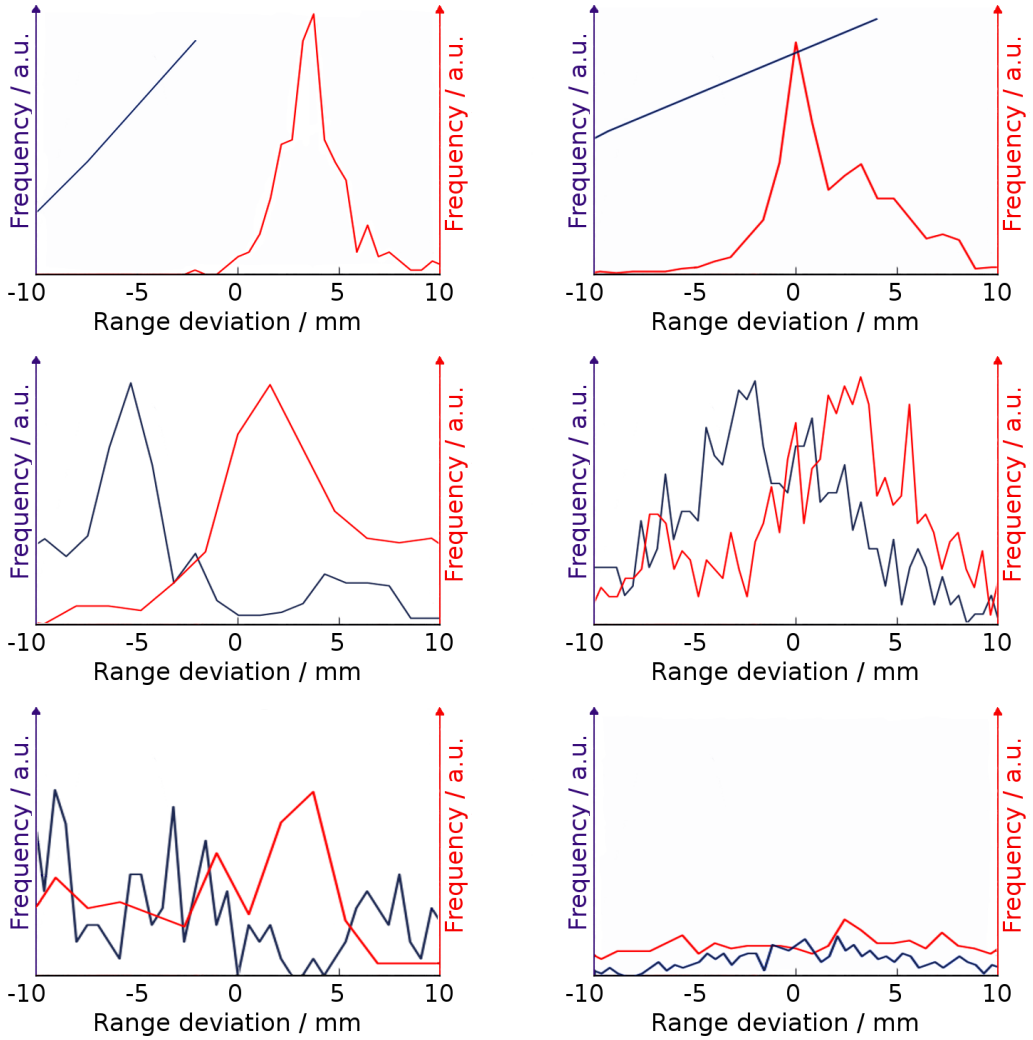

Figure 5.15: YaPET results: histogrammed range deviations for Patient 1 (left) and Patient 2 (right) using the annihilation maps (top) and the reconstructed images obtained with the crystal-based PET camera (center) and with the RPC-based camera (bottom), respectively. For the RPC-based camera a CTR of 100 ps and for the crystal based PET camera a CTR of 600 ps is used. The blue curves indicate the observed range deviations for an actual range shift of -6 ES, whereas the red curves depict the range deviations found in presence of an actual range shift of +6 ES.

6 Conclusions and outlook

In this work, PHITS and a substantially extended HIBRAC version were evaluated with respect to their capabilities to model the production of the most abundant β^+-emitters during particle therapy in comparison to experimental data. In general, PHITS underestimated the production rate of the β^+-emitters and, therefore, previous results obtained for proton beams (Seravalli et al., 2012) were confirmed. However, the selection of the models implemented in PHITS can be important for simulations in this context. Especially, the choice of the evaporation model had much impact on the final results. For energies higher than those applied in particle therapy the impact of the evaporation models on secondary particles was already demonstrated (Mancusi et al., 2011). From the performed simulations in this work it can be concluded that a validation of the evaporation models available in PHITS could be useful. Future simulations should also include the latest intra-nuclear cascade model INCL4.6 (Cugnon et al., 2011), which was recently implemented in PHITS (Sato et al., 2013). The yields obtained with HIBRAC for proton and carbon beams were more accurate than calculated with PHITS and even comparable to GEANT4 results. For carbon ions accurate results were expected since the cross section models and reaction kinematics applied in HIBRAC were used in the Monte Carlo software providing the distribution of annihilation points for the PT-PET monitoring of the carbon ion treatments at GSI (Hasch, 1996). However, HIBRAC would benefit from more detailed benchmarking studies and the adjustment of the implemented cross section models for nuclear reactions, in particular regarding the target fragmentation for helium, lithium, and carbon beams. Especially, the probably imprecise modeling of secondary protons and helium ions, which was remarked before (Sihver et al., 1998), could be a reason for the observed inaccuracies. Experiments aimed at the detection of secondary ions are ongoing, e.g. in the field of proton radiography (Henriquet et al., 2012). After a further validation of the cross section models based on measured data is performed, HIBRAC could be a candidate for the simulation of β^+-emitters in clinical routine PT-PET. Furthermore, it could be tested if the parallelization of the code is possible for a reduction of time consumption which is already low in comparison to GEANT4 and PHITS.

From the simulation study with PHITS regarding the modeling of the prompt γ-rays emitted during proton irradiation, it can be concluded that in the relevant energy range from 3 to 6 MeV PHITS can compete with GEANT4 regarding the quantitative reproduction of

experimental data. In addition to that, the spectrum obtained with PHITS showed accurate Doppler-broadened peaks. In total, PHITS can be considered as an alternative for the modeling of prompt γ-ray emissions awaiting upcoming experiments.

With the intention to optimize the Compton camera prototype, the interactions induced by photons in various camera setups were analyzed by means of GEANT4 simulations. The focus was put onto the evaluation of detection probabilities, the percentage of valid Compton events, the comparison with experimental data, and the suitability of the application of the Compton camera prototype as pair production camera. Between the experimental and simulated energy deposition in the detector layers a good agreement was obtained. Deviations between simulated and measured energy spectra were understood. Thus, an indication for the reliability of the entire simulation study was provided. Furthermore, this comparison led to the reconsideration of the efficiency of the Compton camera prototype. Background mainly results from the escape of secondary particles from one of the detectors. This includes the recoil electrons following a Compton scattering and secondary particles resulting from a pair production. Suitable event selection criteria were provided which improve the percentage of valid Compton events substantially. These selection criteria were based on the filtering of data according to the amount and position of the energy deposition in the detectors. Concerning the detector design and the positioning of the source, several recommendations were derived from the simulations: First of all, to adjust the number of events in order to comply with the electronical capabilities, it is best to change the distance between source and Compton camera. Secondly, although it is unknown which percentage and number of valid Compton events are required for the reconstruction, from these simulations the application of a Compton camera configuration consisting of two CZT detectors with the mentioned dimensions cannot be recommended, since using the CZT-LSO and the CZT-BGO camera a better efficiency and a higher percentage of valid events were achieved. However, the study of the CZT-CZT configuration is relevant for a Compton camera with two CZT detectors used as scatter layers. Using differently shaped sources with varied positions the imaging abilities of the Compton camera prototype for in-vivo dosimetry were confirmed since during a patient treatment there is a broad spatial distribution of γ-ray emissions and, therefore, of scattering angles. A clear advise can be given for experiments with a point source emitting photons with a relatively low energy, e.g. ^{22}Na: to modify the range of feasible scattering angles and, thereby, to obtain a better percentage of valid Compton events, the source should not be in central position in front of the camera, but shifted laterally, or, alternatively, the absorber can be rotated by about 45 degrees with respect to the scatter layer. The adjustment of the lower energy thresholds could be of advantage in terms of the percentage of valid events. In practice, the reduction of the lower energy thresholds is often not possible, in contrast to the rejection of events below a certain threshold, which appeared to be

useful for the absorber. Another possibility to reduce noise is by detecting charged particles associated with invalid events by means of a thin silicon layer placed in-between the scatter and the absorber detector. Additionally, since a high percentage of invalid events originates from energy escape from the absorber layer, a detector behind the absorber registering the escaping particles could also be of advantage. Regarding efficiency as well as rate and number of valid events, large-area Compton cameras are in favor of several small detection systems, given the same overall surface of the cameras. However, the definite evaluation of the applicability of Compton cameras to in-vivo dosimetry requires further experiments including image reconstruction. Finally, the utilization of pair production events for image reconstruction with an existing Compton camera prototype (CZT-LSO) was studied. If in addition to Compton events, electrons and positrons following a pair production are detected, the total efficiency increases by only 10 % for a realistic photon spectrum. Furthermore, even for photons with an energy of 10 MeV an angular resolution was observed which is certainly not enough to detect range deviations of a few millimeters. For these reasons, a further investigation of a similar pair production camera for in-vivo dose verification is not reasonable. Beyond this work is the analysis of further background resulting from particles different to prompt γ-rays. For example, the neutrons produced by interactions of the beam particles need to be studied.

By means of GATE simulations an RPC-based partial-ring PET camera was evaluated with respect to the application to in-beam PET. Realistic distributions of annihilation points derived from carbon ion treatment plans were used to study detector efficiency, the quality of reconstructed images, and the detectability of range deviations. A crystal-based PET camera based on a commercially available PET scanner was used as reference. With the RPC-based PET camera a low efficiency was observed which does not allow the accurate reproduction of the distributions of annihilation points. Furthermore, the reliability of the detection of range deviations with the RPC-based PET camera is questionable. In contrast to the reference crystal-based PET camera, neither the visual inspection of the reconstructed images, nor the results obtained with the semi-automatic tool YaPET provided sufficient information for the RPC-based PET camera. The application of the TOF-MLEM reconstruction was especially advantageous for the considered RPC-based PET camera in terms of convergence and limited angle artifacts. However, the assumed excellent time resolution of the RPC-based PET camera could not fully compensate the low efficiency. For the crystal-based PET camera considerably better images were obtained with MLEM and TOF-MLEM, e.g. limited angle artifacts were not observed at all. With the Direct TOF algorithm about the same level of image quality was achieved as obtained with the TOF-MLEM assuming a CTR of 200 ps FWHM. Eventually, the Direct TOF procedure could be evaluated for the currently investigated RPC-based full-body cameras aimed at diagnostic PET. For the RPC-based PET camera a profound increase

in efficiency would be required for the application to PT-PET. The stacks could be radially increased in width in a way that the gaps in-between the heads, cf. figure 5.1, disappear. Obviously, this would not result in an efficiency as high as achieved for the crystal-based camera. Furthermore, due to the higher scatter fraction inherent to the RPC-based PET camera (Diblen et al., 2012), the same efficiency as obtained with the crystal-based PET camera would not obligatorily result in the same image quality. Since during therapeutic proton irradiation a β^+-activity occurs which is about three times higher than during carbon ion treatment (Parodi et al., 2002; Enghardt et al., 2004; Priegnitz et al., 2008), further studies should include annihilation maps based on treatment plans for proton therapy.

Zusammenfassung

Immer mehr Krebspatienten werden mit Protonen- oder Kohlenstoffstrahlen behandelt. Mit dieser Teilchenstrahlung kann Dosis präzise im Tumor appliziert werden. Allerdings ist die Tiefen-Dosis-Verteilung, die diese Präzision ermöglicht, empfindlich gegenüber Abweichungen vom Bestrahlungsplan, wie z.B. Dichteänderungen im durchstrahlten Gewebe. Um die Qualität der Behandlung zu gewährleisten, ist deshalb eine nicht-invasive In-vivo Dosisverifikation wünschenswert. Diese Überwachung der Partikeltherapie basiert auf der Detektion von Sekundärstrahlung, die entsteht, wenn die eingestrahlten Teilchen mit den Atomkernen des Gewebes wechselwirken.

Bisher ist die einzige klinisch angewandte Methode zur In-vivo Dosisverifikation bei Partikeltherapie die Positronen-Emissions-Tomographie, die auf der während der Bestrahlung entstehenden β^+-Aktivität beruht (PT-PET). Da aus einer PT-PET Messung nicht direkt auf die verabreichte Dosis geschlossen werden kann, wird eine simulierte Verteilung der β^+-emittierenden Kerne als Grundlage für eine Analyse der gemessenen PT-PET Daten genutzt. Dazu ist die zuverlässige Modellierung der Produktionsraten und der tiefenabhängigen Verteilung der β^+-Emitter erforderlich. Wird PT-PET bereits während der Bestrahlung durchgeführt statt im Anschluss, wird von In-beam PET gesprochen. Hierfür stellt das Design der PET-Kamera eine Herausforderung dar, da ein standardmäßiger Vollring-Scanner nicht anwendbar ist. Möglich ist beispielsweise eine Doppelkopf-Kamera, jedoch können niedrige Zählraten und geringe Raumwinkelabdeckung die Bildqualität gefährden. Aus diesem Grund ist ein Detektorsystem mit hoher Zeitauflösung erwünscht, welche die Einbeziehung der Flugzeit (TOF) in den iterativen Rekonstruktionsalgorithmus erlaubt, und dadurch die Bildqualität erheblich verbessern kann.

Ein zweiter Ansatz zielt auf die Detektion der prompten γ-Strahlen und wird als Prompt Gamma Imaging (PGI) bezeichnet. Hinsichtlich der Rate und Energieverteilung der γ-Strahlung, die während Partikelbestrahlung auftritt, ist die experimentelle Datenlage unzureichend, weswegen Simulationen unerlässlich sind. Compton-Kameras, die auf der Detektion inkohärent gestreuter Photonen basieren, sollen für PGI zum Einsatz kommen. In diesem Zusammenhang dienen Monte-Carlo-Simulationen der Optimierung des Aufbaus und der Bewertung von Kriterien zur Selektion der gemessenen Ereignisse.

Voraussetzungen für In-beam PET und PGI sind demnach geeignete Detektorsysteme und detailliertes Wissen über die zugrunde liegenden Strahlungsfelder. Inhalt dieser Arbeit ist die Modellierung der β^+-Emitter und Photonen, die während der Bestrahlung entstehen, sowie die Bewertung der Anwendbarkeit bzw. Optimierung von Detektorsystemen für beide Techniken unter Verwendung verschiedener Simulationsprogramme.

Für die Modellierung der Produktion der häufigsten β^+-Emitter während Partikelbestrahlung wurden das Monte-Carlo-Simulationsprogramm PHITS und der deterministische, eindimensionale Simulationscode HIBRAC getestet. Für Bestrahlungen mit Protonen, Lithium-, Helium- und Kohlenstoffionen wurden die tiefenabhängigen Yields der relevanten β^+-Emitter simuliert und mit Experimentdaten verglichen. Zusätzlich erfolgte ein Vergleich mit Simulationsergebnissen aus dem Monte-Carlo-Programm GEANT4. PHITS unterschätzte im Allgemeinen die Produktionsrate der betrachteten Nuklide und zeigte weit weniger Übereinstimmung mit den Experimenten als die GEANT4 Simulationen, die akzeptable Werte lieferten. Um mit HIBRAC die tiefenabhängigen Yields der einzelnen β^+-emittierenden Nuklide zu simulieren, waren grundlegende Erweiterungen des Codes nötig. Für Protonen und Kohlenstoffionen wurden die Yields der betrachteten β^+-Emitter mit HIBRAC ähnlich genau wie mit GEANT4 modelliert. Da HIBRAC schnell, kompakt und einfach modifizierbar ist, kommt es als Basis für die Simulation der β^+-Emitter im klinischen Einsatz in Frage. Des Weiteren wurde mit PHITS die Reproduzierbarkeit eines Photonenspektrums, das während einer Protonenbestrahlung gemessen wurde, untersucht. Ausgehend von den erzielten Ergebnissen kann PHITS als Alternative zu GEANT4 im Hinblick auf die Simulation prompter γ-Emissionen angesehen werden.

Ein weiteres Ziel der vorliegenden Arbeit war die Optimierung von Compton-Kamera-Prototypen für PGI. Der Fokus der Simulationen mit GEANT4 lag auf der Effizienz der Kameras und den Raten an validen Compton-Ereignissen. Basierend auf diesen Simulationen erscheint eine Compton-Kamera aus einem CZT-Detektor und einem LSO- oder BGO-Detektor anwendbar. Mehrere Empfehlungen, die die Anordnung und den Aufbau der Kamera betreffen, wurden gegeben. Außerdem wurden verschiedene Kriterien zur Selektion der Ereignisse untersucht mit denen der Anteil an validen Compton-Ereignissen erheblich gesteigert werden konnte. Die Simulationen wurden mittels eines Vergleichs zwischen gemessenen und simulierten Energiedepositionen in den Detektoren verifiziert. Der Vergleich ergab eine gute Übereinstimmung und diente außerdem der Kontrolle der Effizienz des Prototyps. In einer weiteren Simulationsstudie wurde die Erweiterung der Compton-Kamera bezüglich der Anwendung als Paarbildungskamera analysiert, d.h. für die Detektion der Elektron-Positron-Paare, die bei einer Paarbildung entstehen. Aufgrund geringer Effizienz und unzureichender Ortsauflösung erscheint die erfolgreiche Anwendung des betrachteten Compton-Kamera-Prototyps als Paarbildungskamera zur In-vivo-

Kontrolle von Partikeltherapie fraglich.

Des Weiteren wurde die Anwendbarkeit von Resistive-Plate-Chambers (RPCs) für In-beam PET diskutiert, da diese Detektoren eine gute Zeitaufösung ermöglichen. Eine aus Szintillatoren bestehende PET-Kamera, die auf einem klinisch angewendeten Scanner basiert, wurde als Referenz verwendet. Für diese Analyse wurde die gesamte Kette, beginnend mit Simulationen der Detektorantwort, über die Bildrekonstruktion unter Verwendung verschiedener Algorithmen, bis zur Bewertung der Bildqualität, betrachtet. Die Grundlage für diese Simulationen bildeten realistische Aktivitätsverteilungen, die auf Plänen für Bestrahlungen mit Kohlenstoffionen basierten. Aufgrund der niedrigen Effizienz der RPC-basierten PET-Kamera ergaben sich rekonstruierte Bilder eingeschränkter Qualität, die weder visuell noch mithilfe des semi-automatischen Werkzeugs YaPET verlässliche Aussagen zur Detektierbarkeit von Reichweiteänderungen lieferten. Die gute Zeitauflösung konnte die niedrige Effizienz also nicht vollständig kompensieren, die Einbeziehung der Flugzeit in den iterativen Rekonstruktionsalgorithmus erwies sich jedoch besonders für die betrachtete RPC-basierte PET-Kamera von erheblichen Vorteil bezüglich Konvergenz und dem Auftreten von Bildartefakten. Direct TOF, eine echtzeitfähige Rückprojektionstechnik, lieferte für die RPC-basierte PET Kamera eine vergleichbare Bildqualität bezogen auf die iterativen Verfahren. Insgesamt erscheint eine weitere Untersuchung von RPC-basierten PET-Kameras ähnlicher Effizienz für In-beam PET wenig aussichtsreich.

In dieser Arbeit wurden Simulationsstudien für die Weiterentwicklung der In-vivo Dosimetrie für Partikeltherapie durchgeführt. Für die Modellierung der β^+-Emitter und prompten γ-Strahlen wurden verschiedene Simulationsprogramme verwendet. HIBRAC könnte eine Basis für die für klinisches PT-PET nötigen Simulationen sein, jedoch wäre eine genauere Überprüfung der zugrunde liegenden Querschnittsmodelle erforderlich. Eine systematische Analyse erbrachte mehrere die Optimierung des Compton-Kamera-Prototyps betreffende Empfehlungen. Für eine abschließende Beurteilung der Anwendbarkeit der Compton Kamera für PGI sind jedoch weitere experimentelle Untersuchungen unerlässlich. Für PT-PET stellt die Effizienz des Detektorsystems den entscheidenden Faktor dar. Basierend auf den Ergebnissen für die betrachtete RPC-basierte PET-Kamera, sollte der Fokus hier weiterhin auf Szintillator-basierten PET-Kameras liegen.

Summary

An increasing number of cancer patients is treated with proton beams or other light ion beams which allow to deliver dose precisely to the tumor. However, the depth dose distribution of these particles, which enables this precision, is sensitive to deviations from the treatment plan, as e.g. anatomical changes. Thus, to assure the quality of the treatment, a non-invasive in-vivo dose verification is highly desired. This monitoring of particle therapy relies on the detection of secondary radiation which is produced by interactions between the beam particles and the nuclei of the patient's tissue.

Up to now, the only clinically applied method for in-vivo dosimetry is Positron Emission Tomography which makes use of the β^+-activity produced during the irradiation (PT-PET). Since from a PT-PET measurement the applied dose cannot be directly deduced, the simulated distribution of β^+-emitting nuclei is used as a basis for the analysis of the measured PT-PET data. Therefore, the reliable modeling of the production rates and the spatial distribution of the β^+-emitters is required. PT-PET applied during instead of after the treatment is referred to as in-beam PET. A challenge concerning in-beam PET is the design of the PET camera, because a standard full-ring scanner is not feasible. For instance, a double-head PET camera is applicable, but low count rates and the limited solid angle coverage can compromise the image quality. For this reason, a detector system which provides a time resolution allowing the incorporation of time-of-flight information (TOF) into the iterative reconstruction algorithm is desired to improve the quality of the reconstructed images.

Secondly, Prompt Gamma Imaging (PGI), a technique based on the detection of prompt γ-rays, is currently pursued. Concerning the emissions of prompt γ-rays during particle irradiation, experimental data is not sufficiently available, making simulations necessary. Compton cameras are based on the detection of incoherently scattered photons and are investigated with respect to PGI. Monte Carlo simulations serve for the optimization of the camera design and the evaluation of criteria for the selection of measured events.

Thus, for in-beam PET and PGI dedicated detection systems and, moreover, profound knowledge about the corresponding radiation fields are required. Using various simulation codes, this thesis contributes to the modelling of the β^+-emitters and photons pro-

duced during particle irradiation, as well as to the evaluation and optimization of hardware for both techniques.

Concerning the modeling of the production of the relevant β^+-emitters, the abilities of the Monte Carlo simulation code PHITS and of the deterministic, one-dimensional code HIBRAC were assessed. The Monte Carlo tool GEANT4 was applied for an additional comparison. For irradiations with protons, helium, lithium, and carbon, the depth-dependent yields of the simulated β^+-emitters were compared to experimental data. In general, PHITS underestimated the yields of the considered β^+-emitters in contrast to GEANT4 which provided acceptable values. HIBRAC was substantially extended to enable the modeling of the depth-dependent yields of specific nuclides. For proton beams and carbon ion beams HIBRAC can compete with GEANT4 for this application. Since HIBRAC is fast, compact, and easy to modify, it could be a basis for the simulations of the β^+-emitters in clinical application. PHITS was also applied to the modeling of prompt γ-rays during proton irradiation following an experimental setup. From this study, it can be concluded that PHITS could be an alternative to GEANT4 in this context.

Another aim was the optimization of Compton camera prototypes. GEANT4 simulations were carried out with the focus on detection probabilities and the rate of valid events. Based on the results, the feasibility of a Compton camera setup consisting of a CZT detector and an LSO or BGO detector was confirmed. Several recommendations concerning the design and arrangement of the Compton camera prototype were derived. Furthermore, several promising event selection strategies were evaluated. The GEANT4 simulations were validated by comparing simulated to measured energy depositions in the detector layers. This comparison also led to the reconsideration of the efficiency of the prototype. A further study evaluated if electron-positron pairs resulting from pair productions could be detected with the existing prototype in addition to Compton events. Regarding the efficiency and the achievable angular resolution, the successful application of the considered prototype as pair production camera to the monitoring of particle therapy is questionable.

Finally, the application of a PET camera consisting of Resistive Plate Chambers (RPCs) providing a good time resolution to in-beam PET was discussed. A scintillator-based PET camera based on a commercially available scanner was used as reference. This evaluation included simulations of the detector response, the image reconstructions using various procedures, and the analysis of image quality. Realistic activity distributions based on real treatment plans for carbon ion therapy were used. The low efficiency of the RPC-based PET camera led to images of poor quality. Neither visually nor with the semi-automatic tool YaPET a reliable detectability of range deviations was possible. The

incorporation of TOF into the iterative reconstruction algorithm was especially advantageous for the considered RPC-based PET camera in terms of convergence and artifacts. The application of the real-time capable back projection method Direct TOF for the RPC-based PET camera resulted in an image quality comparable to the one achieved with the iterative algorihms. In total, this study does not indicate the further investigation of RPC-based PET cameras with similar efficiency for in-beam PET application.

To sum up, simulation studies were performed aimed at the progress of in-vivo dosimetry. Regarding the modeling of the β^+-emitter production and prompt γ-ray emissions, different simulation codes were evaluated. HIBRAC could be a basis for clinical PT-PET simulations, however, a detailed validation of the underlying cross section models is required. Several recommendations for the optimization of a Compton Camera prototype resulted from systematic variations of the setup. Nevertheless, the definite evaluation of the feasibility of a Compton camera for PGI can only be performed by further experiments. For PT-PET, the efficiency of the detector system is the crucial factor. Due to the obtained results for the considered RPC-based PET camera, the focus should be kept to scintillator-based PET cameras for this purpose.

References

Agostinelli S, Allison J, Amako K, Apostolakis J, Araujo H, Arce P, Asai M, Axen D, Banerjee S, Barrand G, Behner F, Bellagamba L, Boudreau J, Broglia L, Brunengo A, Burkhardt H, Chauvie S, Chuma J, Chytracek R, Cooperman G, Cosmo G, Degtyarenko P, Dell'Acqua A, Depaola G, Dietrich D, Enami R, Feliciello A, Ferguson C, Fesefeldt H, Folger G, Foppiano F, Forti A, Garelli S, Giani S, Giannitrapani R, Gibin D, Gómez Cadenas JJ, González I, Gracia Abril G, Greeniaus G, Greiner W, Grichine V, Grossheim A, Guatelli S, Gumplinger P, Hamatsu R, Hashimoto K, Hasui H, Heikkinen A, Howard A, Ivanchenko V, Johnson A, Jones FW, Kallenbach J, Kanaya N, Kawabata M, Kawabata Y, Kawaguti M, Kelner S, Kent P, Kimura A, Kodama T, Kokoulin R, Kossov M, Kurashige H, Lamanna E, Lampén T, Lara V, Lefebure V, Lei F, Liendl M, Lockman W, Longo F, Magni S, Maire M, Medernach E, Minamimoto K, Mora de Freitas P, Morita Y, Murakami K, Nagamatu M, Nartallo R, Nieminen P, Nishimura T, Ohtsubo K, Okamura M, O'Neale S, Oohata Y, Paech K, Perl J, Pfeiffer A, Pia MG, Ranjard F, Rybin A, Sadilov S, di Salvo E, Santin G, Sasaki T, Savvas N, Sawada Y, Scherer S, Sei S, Sirotenko V, Smith D, Starkov N, Stoecker H, Sulkimo J, Takahata M, Tanaka S, Tcherniaev E, Safai Tehrani E, Tropeano M, Truscott P, Uno H, Urban L, Urban P, Verderi M, Walkden A, Wander W, Weber H, Wellisch JP, Wenaus T, Williams DC, Wright D, Yamada T, Yoshida H, Zschiesche D. 2003. GEANT4–a simulation toolkit. Nucl Instrum Methods Phys Res A 506(3):250-303

Armstrong TW, Chandler KC. 1973. A Fortran program for computing stopping powers and ranges for muons, charged pions, protons, and heavy ions. ORNL-4869, Oak Ridge National Laboratory, Oak Ridge

Attanasi F, Knopf A, Parodi K, Paganetti H, Bortfeld T, Rosso V, Del Guerra A. 2011. Extension and validation of an analytical model for in vivo PET verification of proton therapy–a phantom and clinical study. Phys Med Biol 56(16):5079-5098

Ballarini F, Battistoni G, Cerutti F, Empl A, Fassò A, Ferrari A, Gadioli E, Garzelli MV, Ottolenghi A, Pinsky LS, Ranft J, Roesler S, Sala PR, Smirnov G. 2005. Nuclear models in FLUKA: Present capabilities, open problems, and future improvements. AIP Conf Proc 769:1197-1202

Baskar R, Lee KA, Yeo R, Yeoh KW. 2012. Cancer and radiation Therapy: current advances and future directions. Int J Med Sci 9(3):193-199

Bassler N, Alsner J, Beyer G, DeMarco JJ, Doser M, Hajdukovic D, Hartley O, Iwamoto KS, Jäkel O, Knudsen HV, Kovacevic S, Møller SP, Overgaard J, Petersen JB, Solberg TD, Sørensen BS, Vranjes S, Wouters BG, Holzscheiter MH. 2008. Antiproton radiotherapy. Radiother Oncol 86(1):14-19

Bauer J, Unholtz D, Sommerer F, Kurz C, Haberer T, Herfarth K, Welzel T, Combs SE, Debus J, Parodi K. 2013. Implementation and initial clinical experience of offline PET/CT-based verification of scanned carbon ion treatment. Radiother Oncol 107(2):218-226

Berger MJ, Hubbell JH, Seltzer SM, Chang J, Coursey JS, Sukumar R, Zucker DS, Olsen K. 2014. XCOM: Photon Cross Sections Database [updated on Dec. 9th 2011, called on Sept. 26th 2014] URL: http://physics.nist.gov/PhysRefData/Xcom/html/xcom1.html

Bethe HA, Ashkin J. 1953. Passage of radiations through matter. In: Segré E (ed) Experimental Nuclear Physics. Wiley, New York, p. 166-357

Bethge K, Walter G, Wiedemann B. 2008. Kernphysik. 3. Auflage. Springer-Verlag, Berlin, Heidelberg

Bittner MI, Grosu AL, Wiedenmann N, Wilkens JJ. 2014. A systematic review of antiproton radiotherapy. Front Phys 1(37):1-8

Blakely EA, Tobias CA, Ngo FQH, Curtis SB. 1980. Physical and cellular radiobiological properties of heavy ions in relation to cancer therapy applications. In: Pirruccello MC, Tobias CA (eds) Biological and medical research with accelerated heavy ions at the Bevalac, 1977-1980. Biology and Medicine Division, Lawrence Berkeley Laboratory, University of California, p. 73-86

Blanco A, Chepel V, Ferreira-Marques R, Fonte P, Lopes MI, Peskov V, Policarpo A. 2003. Perspectives for positron emission tomography with RPCs. Nucl Instrum Methods Phys Res A 508(1-2):88-93

Böhlen TT, Cerutti F, Dosanjh M, Ferrari A, Gudowska I, Mairani A, Quesada JM. 2010. Benchmarking nuclear models of FLUKA and GEANT4 for carbon ion therapy. Phys Med Biol 55(19):5833-5847

Cerron Zeballos E, Crotty I, Hatzifotiadou, D, Lamas Valverde L, Neupane S, Williams MCS, Zichichi A. 1996. A new type of resistive plate chamber: The multigap RPC. Nucl Instrum Methods Phys Res A 374(1):132-135

Cirrone GAP, Cuttone G, Di Rosa F, Pandola L, Romano F, Zhang Q. 2010. Validation of the Geant4 electromagnetic photon cross-sections for elements and compounds. Nucl Instrum Methods Phys Res A 618(1-3):315-322

Conti M. 2011. Why is TOF PET reconstruction a more robust method in the presence of inconsistent data? Phys Med Biol 56(1):155-168

Crespo P, Shakirin G, Enghardt W. 2006. On the detector arrangement for in-beam PET for hadron therapy monitoring. Phys Med Biol 51(9):2143-2163

Crespo P, Shakirin G, Fiedler F, Enghardt W, Wagner A. 2007. Direct time-of-flight for quantitative, real-time in-beam PET: a concept and feasibility study. Phys Med Biol 52(23):6795-6811

Crespo P, Reis J, Couceiro M, Blanco A, Ferreira NC, Marques RF, Fonte P. 2009. Whole-body single-bed time-of-flight RPC-PET: Simulation of axial and planar sensitivities with NEMA and anthropomorphic phantoms. IEEE Nucl Sci Symp Conf Rec (2009):3420-3425

Cugnon J. 1980. Monte Carlo calculation of high-energy heavy-ion interactions. Phys Rev C Nucl Phys 22(5):1885-1896

Cugnon J, Mizutani T, Vandermeulen J. 1981. Equilibration in relativistic nuclear collisions. A Monte Carlo calculation. Nucl Phys A 352(3):505-534

Cugnon J, Mancusi D, Boudard A, Leray S. 2011. New Features of the INCL4 Model for Spallation Reactions. J Korean Phys Soc 59(2):955-958

Diblen F, Rohling H, Torres-Espallardo I, Solevi P, Gillam J, España Palomares S, Vandenberghe S, Watts D, Fiedler F, Rafecas M. 2012. Comparison study of RPC and crystal based PET systems for hadron therapy monitoring. IEEE Nucl Sci Symp Conf Rec (2012):2212-2217

Dimmock MR, Nikulin DA, Brown JMC, Nguyen CV, Gillam JE. 2010. GPU acceleration of

compton reconstruction for the PEDRO. IEEE Nucl Sci Symp Conf Rec (2010):2665-2668

Dresner L. 1963. EVAP: A FORTRAN program for calculating the evaporation of various particles from excited compound nuclei. Oak Ridge report ORNL-TM-196, Oak Ridge National Laboratory, Oak Ridge

Eickhoff H, Linz U. 2008. Medical Applications of Accelerators. Reviews of Accelerator Science and Technology 1(1):143-161

Enghardt W, Crespo P, Fiedler F, Parodi K, Pawelke J, Pönisch F. 2004. Charged hadron tumour therapy monitoring by means of PET. Nucl Instrum Methods Phys Res A 525(1-2):284-288

Fiedler F, Crespo P, Parodi K, Sellesk M, Enghardt W. 2006. The Feasibility of In-Beam PET for Therapeutic Beams of ^{3}He. IEEE Trans Nucl Sci 53(4):2252-2259

Fiedler F, Priegnitz M, Jülich R, Pawelke J, Crespo P, Parodi K, Pönisch F, Enghardt W. 2008. In-beam PET measurements of biological half-lives of ^{12}C irradiation induced β^{+}-activity. Acta Oncol 47(6):1077-1086

Fiedler F. 2008. Anwendung des in-beam PET Therapiemonitorings auf Präzisionsbestrahlungen mit Helium-Ionen. Technische Universität Dresden, Fakultät Mathematik und Naturwissenschaften, PhD thesis.

Fiedler F, Shakirin G, Skowron J, Braess H, Crespo P, Kunath D, Pawelke J, Pönisch F, Enghardt W. 2010a. On the effectiveness of ion range determination from in-beam PET data. Phys Med Biol 55(7):1989-1998

Fiedler F, Kormoll T, Müller A, Enghardt W. 2010b. Requirements on the instrumentation of a prompt gamma measuring device. IEEE Nucl Sci Symp Conf Rec (2010):1047-1049

Firestone RB. 2004. WWW Table of Thermal Neutron Capture Gammas [updated on March 17th 2004, called on June 3rd 2014] URL: http://ie.lbl.gov/PGAA/PGAASearch.asp

Frey K, Bauer J, Unholtz D, Kurz C, Krämer M, Bortfeld T, Parodi K. 2014. TPS(PET) – A TPS-based approach for in vivo dose verification with PET in proton therapy. Phys Med Biol 59(1):1-21

Furihata S. 2000. Statistical analysis of light fragment production from medium energy

proton-induced reactions. Nucl Instrum Methods Phys Res B 171(3):251-258

Geissel H, Scheidenberger C. 1998. Slowing down of relativistic heavy ions and new applications. Nucl Instrum Methods Phys Res B 136-138:114-124

Georgiev G, Ilieva N, Kozhuharov V, Lessigiarska I, Litov L, Pavlov B, Petkov P. 2013. Multigap RPC for PET: development and optimisation of the detector design. J Instrum 8:P01011

Gillam J, Beveridge T, Svalbe I, Grint A, Cooper R, Boston A, Boston H, Nolan P, Hall C, Lewis R. 2008. Compton imaging using the SmartPET detectors. IEEE Nucl Sci Symp Conf Rec (2008):624-628

Golnik C, Dersch U, Fiedler F, Kormoll T, Rohling H, Enghardt W. 2011. A pair production upgrade for a compton imager for in-vivo dosimetry at therapeutic proton and ion beams. IEEE Nucl Sci Symp Conf Rec (2011):3323-3326

Groiselle CJ, Glick SJ. 2004. 3D PET list-mode iterative reconstruction using time-of-flight information. IEEE Nucl Sci Symp Conf Rec (2004):2633-2638

Hall EJ, Giacca AJ. 2012. Radiobiology for the radiologist. 7th edition. Wolters Kluwer Health, Philadelphia.

Hansen DC, Lühr A, Sobolevsky N, Bassler N. 2012. Optimizing SHIELD-HIT for carbon ion treatment. Phys Med Biol 57(8):2393-2409

Hasch B. 1996. Die physikalischen Grundlagen einer Verifikation des Bestrahlungsplans in der Schwerionen-Tumortherapie mit der Positronen-Emissions-Tomographie. Technische Universität Dresden, Fakultät Mathematik und Naturwissenschaften, PhD thesis.

Helmbrecht S, Enghardt W, Parodi K, Didinger B, Debus J, Kunath D, Priegnitz M, Fiedler F. 2013. Analysis of metabolic washout of positron emitters produced during carbon ion head and neck radiotherapy. Med Phys 40(9):091918

Helmbrecht S, Santiago A, Enghardt W, Kuess P, Fiedler F. 2012. On the feasibility of automatic detection of range deviations from in-beam PET data. Phys Med Biol 57(5):1387-1397

Helmbrecht S, Kuess P, Birkfellner W, Enghardt W, Stützer K, Georg D, Fiedler F. 2014.

Systematic analysis on the achievable precision of PT-PET measurements by means of automated evaluation techniques. Z Med Phys (in press), DOI: 10.1016/j.zemedi.2014.0-8.004

Henriquet P, Testa E, Chevallier M, Dauvergne D, Dedes G, Freud N, Krimmer J, Létang JM, Ray C, Richard MH, Sauli F. 2012. Interaction vertex imaging (IVI) for carbon ion therapy monitoring: a feasibility study. Phys Med Biol 57(14):4655-4669

Hirano Y, Kinouchi S, Ikoma Y, Yoshida E, Wakizaka H, Ito H, Yamaya T. 2013. Compartmental analysis of washout effect in rat brain: in-beam OpenPET measurement using a ^{11}C beam. Phys Med Biol 58(23):8281-8294

Hueso-González F, Golnik C, Berthel M, Dreyer A, Enghardt W, Fiedler F, Heidel K, Kormoll T, Rohling H, Schöne S, Schwengner R, Wagner A, Pausch G. 2014. Test of Compton camera components for prompt gamma imaging at the ELBE bremsstrahlung beam. J Instrum 9:P05002

Incerti S. 2014. Livermore low-energy electromagnetic models. [updated on Dec. 7th 2013, called on May 28th 2014] URL: https://twiki.cern.ch/twiki/bin/view/Geant4/LoweMigratedLivermore

Iseki Y, Kanai T, Kanazawa M, Kitagawa A, Mizuno H, Tomitani T, Suda M, Urakabe E. 2004. Range verification system using positron emitting beams for heavy-ion radiotherapy. Phys Med Biol 49(14):3179-3195

Jan S, Benoit D, Becheva E, Carlier T, Cassol F, Descourt P, Frisson T, Grevillot L, Guigues L, Maigne L, Morel C, Perrot Y, Rehfeld N, Sarrut D, Schaart DR, Stute S, Pietrzyk U, Visvikis D, Zahra N, Buvat I. 2011. GATE V6: a major enhancement of the GATE simulation platform enabling modelling of CT and radiotherapy. Phys Med Biol 56(4):881-901

Japan Atomic Energy Agency. 2014. PHITS Ver. 2.64 User's manual. Available online [updated on Feb. 19th 2014, called on Feb. 28th 2014] URL: http://phits.jaea.go.jp/rirekimanuale.html

Jäkel O, Schulz-Ertner D, Karger CP, Heeg P, Debus J. 2005. Experience with carbon ion radiotherapy at GSI. Nucl Instrum Methods Phys Res B 241(1-4):717-720.

Kaatsch P, Spix C, Hentschel S, Katalinic A, Luttmann S, Stegmaier C, Caspritz S, Cer-

naj J, Ernst A, Folkerts J, Hansmann J, Kranzhöfer K, Krieghoff-Henning E, Kunz B, Penzkofer A, Treml K, Wittenberg K, Baras N, Barnes B, Bertz J, Buttmann-Schweiger N, Dahm S, Franke M, Haberland J, Kraywinkel K, Wienecke A, Wolf U. 2013. Krebs in Deutschland 2009 / 2010. Robert Koch-Institut und die Gesellschaft der epidemiologischen Krebsregister in Deutschland e.V. (eds). 9. Ausgabe, Berlin

Kabuki S, Kimura H, Amano H, Nakamoto Y, Kubo H, Miuchi K, Kurosawa S, Takahashi M, Kawashima H, Ueda M, Okada T, Kubo A, Kunieda E, Nakahara T, Kohara R, Miyazaki O, Nakazawa T, Shirahata T, Yamamoto E, Ogawa K, Togashi K, Saji H, Tanimori T. 2010. Electron-tracking Compton gamma-ray camera for small animal and phantom imaging. Nucl Instrum Methods Phys Res A 623(1):606-607

Kacperek A. 2012. Ocular proton therapy centers. In: Linz U (ed) Ion beam therapy. Springer-Verlag, Heidelberg, Berlin, p. 149-177

Kanbach G, Andritschke R, Zoglauer A, Ajello M, McConnell ML, Macri JR, Ryan JM, Bloser P, Hunter S, DiCocco G, Kurfess J, Reglero V. 2005. Development and Calibration of the tracking Compton/Pair telescope MEGA. Nucl Instrum Methods Phys Res A 541(1-2):310-322

Kim CH, Park JH, Seo H, Lee HR. 2012. Gamma electron vertex imaging and application to beam range verification in proton therapy. Med Phys 39(2):1001-1005

Knopf A, Parodi K, Bortfeld T, Shih HA, Paganetti H. 2009. Systematic analysis of biological and physical limitations of proton beam range verification with offline PET/CT scans. Phys Med Biol 54(14):4477-4495.

Kormoll T, Fiedler F, Schöne S, Wüstemann J, Zuber K, Enghardt W. 2011. A Compton imager for in-vivo dosimetry of proton beams - A design study. Nucl Instrum Methods Phys Res A 626-627:114-119

Kormoll T. 2013. A Compton camera for in-vivo dosimetry in ion-beam radiotherapy. Technische Universität Dresden. Fakultät Mathematik und Naturwissenschaften. PhD Thesis

Kozlovsky B, Murphy RJ, Ramaty R. 2002. Nuclear deexcitation gamma-ray lines from accelerated particle interactions. Astrophys J Suppl Ser 141(2):523-531

Kraft G. 2000. Tumortherapy with ion beams. Nucl Instrum Methods Phys Res A 454:1-10

La Tessa C, Sihver L, Mancusi D, Zeitlin C, Miller J, Guetersloh S, Heilbronn L. 2007. Weak and strong factorization properties in nucleus-nucleus collisions in the energy region 290-2100 MeV/n. Nucl Phys A 791(3-4):451-472

Laube K, Menkel S, Bert C, Enghardt W, Helmbrecht S, Saito N, Fiedler F. 2013. 4D particle therapy PET simulation for moving targets irradiated with scanned ion beams. Phys Med Biol 58(3):513-533

Lauckner, K. 1999. Entwicklung eines iterativen 3D Rekonstruktionsverfahrens für die Kontrolle der Tumorbehandlung mit Schwerionen mittels der Positronen- Emissions-Tomographie. Technische Universität Dresden, Fakultät Elektrotechnik, PhD Thesis

Llacer J, Chatterjee A, Alpen EL, Saunders W, Andreae S, Jackson HC. 1984. Imaging by injection of accelerated radioactive particle beams. IEEE Trans Med Imaging 3(2):80-90

Lois C, Jakoby BW, Long MJ, Hubner KF, Barker DW, Casey ME, Conti M, Panin VY, Kadrmas DJ, Townsend DW. 2010. An assessment of the impact of incorporating time-of-flight information into clinical PET/CT imaging. J Nucl Med 51(2):237-245

Lojacono X, Richard MH, Ley JL, Testa E, Ray C, Freud N, Létang JM, Dauvergne D, Maxim V, Prost R. 2013. Low statistics reconstruction of the Compton camera point spread function in 3D prompt-γ imaging of ion beam therapy. IEEE Trans Nucl Sci 60(5): 3355-3363

Mancusi D, Boudard A, Cugnon J, David JC, Leray S. 2011. Influence of nuclear deexcitation on observables relevant for space exploration. Adv Space Res 47(7):1194-1199

Maxim V, Frandes M, Prost R. 2009. Analytical inversion of the Compton Transform using the full set of available projections. Inverse Probl 25(9):095001

Mayer R, Mock U, Jäger R, Pötter R, Vutuc C, Eiter H, Krugmann K, Hammer J, Hirn B, Hawliczek R, Knocke-Abulesz TH, Lukas P, Nechville E, Pakisch B, Papauschek M, Raunik W, Rhomberg W, Sabitzer H, Schratter-Sehn A, Sedlmayer F, Wedrich I, Auberger T. Epidemiological aspects of hadron therapy: a prospective nationwide study of the Austrian project MedAustron and the Austrian Society of Radiooncology (OEGRO). 2004. Radiother Oncol 74(Suppl. 2):24-28.

Michelson PF, Atwood WB, Ritz S. 2010. Fermi gamma-ray space telescope: high-energy

results from the first year. Rep Prog Phys 73(7):074901

Min CH, Kim CH, Youn MY, Kim JW. 2006. Prompt gamma measurements for locating the dose falloff region in the proton therapy. Appl Phys Lett 89(18):183517

Mizuno H, Tomitani T, Kanazawa M, Kitagawa A, Pawelke J, Iseki Y, Urakabe E, Suda M, Kawano A, Iritani R, Matsushita S, Inaniwa T, Nishio T, Furukawa S, Ando K, Nakamura YK, Kanai T, Ishii K. 2003. Washout measurement of radioisotope implanted by radioactive beams in the rabbit. Phys Med Biol 48(15):2269-2281

Moses WW. 2003. Time of flight in PET revisited. IEEE Trans Nucl Sci 50(5):1325-1330

Müller A, Fiedler F, Georg D, Hopfgartner J, Enghardt W. 2012. In-beam SPECT based in vivo dosimetry: from treatment planning to measured dose. Radiother Oncol 102(Suppl. 1):47-48

Nara Y, N Otuka, Ohnishi A, Niita K, Chiba S. 1999. Relativistic nuclear collisions at 10 AGeV energies from p+Be to Au+Au with the hadronic cascade model. Phys Rev C Nucl Phys 61:024901

National Nuclear Data Center. 2013. Experimental Nuclear Reaction Data (EXFOR). [updated on Feb. 26th 2013, called on March 28th 2013] URL: www.nnudc.bnl.gov/exfor-/exfor00.htm

National Nuclear Data Center. 2014. Experimental Nuclear Reaction Data (EXFOR). [updated on April 22th 2014, called on June 2nd 2014] URL: https://www-nds.iaea.org/exfor/exfor.htm

Niita K, Chiba S, Maruyama T, Maruyama T, Takada H, Fukahori T, Nakahara Y, Iwamoto A. 1995. Analysis of the (N,xN') reactions by quantum molecular dynamics plus statistical decay model. Phys Rev C Nucl Phys 52:2620-2635

Nishio T, Miyatake A, Ogino T, Nakagawa K, Saijo N, Esumi H. 2010. The development and clinical use of a beam ON-LINE PET system mounted on a rotating gantry port in proton therapy. Int J Radiat Oncol Biol Phys 76(1):277-286

Olson DL, Berman BL, Greiner DE, Heckman HH, Lindstrom PJ, Crawford HJ. 1983. Factorization of fragment-production cross sections in relativistic heavy-ion collisions. Phys Rev C Nucl Phys 28:1602-1613

OpenGATEcollaboration. 2014. Users Guide V6.1 [updated on Jan. 8th 2014, called on June 4th 2014] http://www.opengatecollaboration.org/index.php/Users_Guide_V6.1

Paganetti H, Niemierko A, Ancukiewicz M, Gerweck LE, Goitein M, Loeffler JS, Suit HD. 2002. Relative biological effectiveness (RBE) values for proton beam therapy. Int J Radiat Oncol Biol Phys 53(2):407-421.

Parodi K, Enghardt W. 2000. Potential application of PET in quality assurance of proton therapy. Phys Med Biol 45(11):N151-N156

Parodi K, Enghardt W, Haberer T. 2002. In-beam PET measurements of β^+ radioactivity induced by proton beams. Phys Med Biol 47(1):21-36

Parodi K, Crespo P, Eickhoff H, Haberer T, Pawelke J, Schardt D, Enghardt W. 2005. Random coincidences during in-beam PET measurements at microbunched therapeutic ion beams. Nucl Instrum Methods Phys Res A 545(1-2):446-458

Parodi K, Bortfeld T. 2006. A filtering approach based on Gaussian–powerlaw convolutions for local PET verification of proton radiotherapy. Phys Med Biol 51(8):1991-2009

Parodi K, Paganetti H, Shih HA, Michaud S, Loeffler JS, DeLaney TF, Liebsch NJ, Munzenrieder JE, Fischman AJ, Knopf A, Bortfeld T. 2007. Patient study of in vivo verification of beam delivery and range, using positron emission tomography and computed tomography imaging after proton therapy. Int J Radiat Oncol Biol Phys 68(3):920-934

Parodi K, Saito N, Chaudhri N, Richter C, Durante M, Enghardt W, Rietzel E, Bert C. 2009. 4D in-beam positron emission tomography for verification of motion-compensated ion beam therapy. Med Phys 36(9):4230-4243

Particle Therapy Co-Operative Group. 2013. Particle therapy facilities in operation (incl. patient statistics) [updated on March 14th 2013, called on March 26th 2013] URL: http://ptcog.-web.psi.ch/ptcentres.html

Pönisch F, Enghardt W, Lauckner K. 2003. Attenuation and scatter correction for in-beam positron emission tomography monitoring of tumour irradiatians with heavy ions. Phys Med Biol 48(15):2419-2436

Pönisch F, Parodi K, Hasch BG, Enghardt W. 2004. The modelling of positron emitter

production and PET imaging during carbon ion therapy. Phys Med Biol 49(23):5217-5232

Priegnitz M, Möckel D, Parodi K, Sommerer F, Fiedler F, Enghardt W. 2008. In-beam PET measurement of $^{7}Li^{3+}$ irradiation induced β^{+}-activity. Phys Med Biol 53(16):4443-4453

Priegnitz M, Fiedler F, Kunath D, Laube K, Enghardt W. 2012. An experiment-based approach for predicting positron emitter distributions produced during therapeutic ion irradiation. IEEE Trans Nucl Sci 59(1):77-87

Priegnitz M. 2012. Ein neues Konzept zur Modellierung der Positronenemitter-Produktion bei der Partikeltherapie. Technische Universität Dresden, Medizinische Fakultät, PhD thesis.

Pshenichnov I, Mishustin I, Greiner W. 2006. Distributions of positron-emitting nuclei in proton and carbon-ion therapy studied with GEANT4. Phys Med Biol 51(23):6099-6112

Pshenichnov I, Larionov A, Mishustin I, Greiner W. 2007. PET monitoring of cancer therapy with ^{3}He and ^{12}C beams: a study with the GEANT4 toolkit. Phys Med Biol 52(24):7295-7312

Qi J, Leahy RM. 2006. Iterative reconstruction in emission comuted tomography. Phys Med Biol 51(15):541-578

Richard MH, Chevallier M, Dauvergne D, Freud N, Henriquet P, Le Foulher F, Létang JM, Montarou G, Ray C, Roellinghoff F, Testa E, Testa M, Walenta AH. 2011. Design guidelines for a double scattering Compton camera for prompt-γ imaging during ion beam therapy: a Monte Carlo simulation study. IEEE Trans Nucl Sci 58(1):87-94

Roellinghoff F, Richard MH, Chevallier M, Constanzo J, Dauvergne D, Freud N, Henriquet P, Le Foulher F, Létang JM, Montarou G, Ray C, Testa E, Testa M, Walenta AH. 2011. Design of a Compton camera for 3D prompt-γ imaging during ion beam therapy. Nucl Instrum Methods Phys Res A 648(Suppl. 1):20-23

Roellinghoff F, Benilov A, Dauvergne D, Dedes G, Freud N, Janssens G, Krimmer J, Létang JM, Pinto M, Prieels D, Ray C, Smeets J, Stichelbaut F, Testa E. 2014. Real-time proton beam range monitoring by means of prompt-gamma detection with a collimated camera. Phys Med Biol 59(5):1327-1338

Sato T, Sihver L, Iwase H, Nakashima H, Niita K. 2005. Simulations of an accelerator-

based shielding experiment using the particle and heavy-ion transport code system PHITS. Adv Space Res 35(2):208-213

Sato T, Kase Y, Watanabe R, Niita K, Sihver L. 2009. Biological dose estimation for charged-particle therapy using an improved PHITS code coupled with a microdosimetric kinetic model. Radiat Res 171:107-117

Sato T, Niita K, Matsuda N, Hashimoto S, Iwamoto Y, Noda S, Ogawa T, Iwase H, Nakashima H, Fukahori T, Okumura K, Kai T, Chiba S, Furuta T, Sihver L. 2013. Particle and Heavy Ion Transport Code System, PHITS, Version 2.52. J Nucl Sci Technol 50(9):913-923

Schaart DR, Seifert S, Vinke R, van Dam HT, Dendooven P, Löhner H, Beekman FJ. 2010. LaBr(3):Ce and SiPMs for time-of-flight PET: achieving 100 ps coincidence resolving time. Phys Med Biol 55(7):N179-N189

Schardt D, Elsässer T, Schultz-Ertner D. 2010a. Heavy-ion tumor therapy: Physical and radiobiological benefits. Rev Mod Phys 82(1):383-425

Schardt D, Iwase H, Martino G, Kaderka R, La Tessa C, Meer D, Safai S, Sihver L. 2010b. Energy spectrum of fast neutrons produced by 130 MeV protons in water. GSI SCIENTIFIC REPORT 2010 HEALTH-42:481

Scheidenberger C, Geissel H. 1998. Penetration of relativistic heavy ions through matter. Nucl Instrum Methods Phys Res B 135(1-4):25-34

Schneider W, Bortfeld T, Schlegel W. 2000. Correlation between CT numbers and tissue parameters needed for Monte Carlo simulations of clinical dose distributions. Phys Med Biol 45(2):459-478.

Schöne S, Shakirin G, Kormoll T, Herbach CM, Pausch G, Enghardt W. 2010. A common approach to image reconstruction for different applications of Compton cameras. IEEE Nucl Sci Symp Conf Rec (2010):2292-2293

Schönfelder V, Aarts H, Bennett K, de Boer H, Clear J, Collmar W, Connors A, Deerenberg A, Diehl R, von Dordrecht A, den Herder J W, Hermsen W, Kippen M, Kuiper L, Lichti G, Lockwood J, Macri J, McConnell M, Morris D, Much R, Ryan J, Simpson G, Snelling M, Stacy G, Steinle H, Strong A, Swanenburg BN, Taylor B, de Vries C, Winkler C. 1993. Instrument description and performance of the Imaging Gamma-Ray Telescope COMPTEL

aboard the Compton Gamma-Ray Observatory. Astrophys J Suppl Ser 86(2):657-692

Schönfelder. 2004. Imaging principles and techniques in space-borne gamma-ray astronomy. Nucl Instrum Methods Phys Res A 525(1-2):98-106

Schulz-Ertner D. 2012. Scull Base Tumors. In: Linz U. Ion Beam Therapy, Springer-Verlag, Berlin, Heidelberg, p. 193-205

Seravalli E, Robert C, Bauer J, Stichelbaut F, Kurz C, Smeets J, Van Ngoc Ty C, Schaart DR, Buvat I, Parodi K, Verhaegen F. 2012. Monte Carlo calculations of positron emitter yields in proton radiotherapy. Phys Med Biol 57(6):1659-1673

Shakirin G, Crespo P, Fiedler F, Wagner A, Enghardt W. 2008. Optimum voxel size for reconstruction of in-beam PET data. IEEE Nucl Sci Symp Conf Rec (2008):5066-5069

Shakirin G. 2009. System solution for in-beam positron emission tomography monitoring of radiation therapy. Technische Universität Dresden, Fakultät Elektrotechnik und Informationstechnik, PhD thesis.

Shakirin G, Braess H, Fiedler F, Kunath D, Laube K, Parodi K, Priegnitz M, Enghardt W. 2011. Implementation and workflow for PET monitoring of therapeutic ion irradiation: a comparison of in-beam, in-room, and off-line techniques. Phys Med Biol 56(5):1281-1298

Shen W, Wang B, Feng J, Zhan W, Zhu Y, Feng E. 1989. Total reaction cross section for heavy-ion collisions and its relation to the neutron excess degree of freedom. Nucl Phys A 491(1):130-146

Shepp LA, Vardi Y. 1982. Maximum likelihood reconstruction for emission tomography. IEEE Trans Med Imaging 1(2):113-122

Shinoto M, Yamada S, Yasuda S, Imada H, Shioyama Y, Honda H, Kamada T, Tsujii H, Saisho H. 2013. Phase I/II trial of carbon-ion radiotherapy with concurrent gemcitabine for patients with locally advanced pancreatic cancer. J Clin Oncol 31, 2013 (suppl; abstr e15008)

Sihver L, Tsao CH, Silberberg R, Kanai T, Barghouty AF. 1993. Total reaction and partial cross section calculations in proton-nucleus ($Z_t \leq 26$) and nucleus-nucleus reactions (Z_p and $Z_t \leq 26$). Phys Rev C Nucl Phys 47(3):1225-1236

Sihver L, Tsao CH, Silberberg R, Barghouty AF, Kanai T. 1996. Calculations of depth dose distributions, cross sections and momentum loss. Adv Space Res 17(2):105-108

Sihver L, Schardt D, Kanai T. 1998. depth dose distribution of high energy carbon, oxygen and neon beams in water. Japanese Journal of Medical Physics 18(1):1-21

Sihver L, Mancusi D. 2009. Present status and validation of HIBRAC. Radiat Meas 44(1):38-46

Sihver L, Sato T, Puchalska M, Reitz G. 2010. Simulations of the MATROSHKA experiment at the international space station using PHITS. Radiat Environ Biophys 49(3):351-357

Sihver L, Lantz M, Takechi M, Kohama A, Ferrari A, Cerutti F, Sato T. 2012a. A comparison of total reaction cross section models used in particle and heavy ion transport codes. Adv Space Res 49(4):812-819

Sihver L, Lantz M, Böhlen TT, Mairani A, Cerutti AF, Ferrari A. 2012b. A comparison of total reaction cross section models used in FLUKA, GEANT4 and PHITS. IEEE Aerospace Conf(2012):1-10

Smeets J, Roellinghoff F, Prieels D, Stichelbaut F, Benilov A, Busca P, Fiorini C, Peloso R, Basilavecchia M, Frizzi T, Dehaes JC, Dubus A. 2012. Prompt gamma imaging with a slit camera for real-time range control in proton therapy. Phys Med Biol 57(11):3371-3405

Sommerer F, Cerutti F, Parodi K, Ferrari A, Enghardt W, Aiginger H. 2009. In-beam PET monitoring of mono-energetic ^{16}O and ^{12}C beams: experiments and FLUKA simulations for homogeneous targets. Phys Med Biol 54(13):3979-3996

Sportelli G, Belcari N, Camarlinghi N, Cirrone GA, Cuttone G, Ferretti S, Kraan A, Ortuño JE, Romano F, Santos A, Straub K, Tramontana A, Guerra AD, Rosso V. 2014. First full-beam PET acquisitions in proton therapy with a modular dual-head dedicated system. Phys Med Biol 59(1):43-60

Stratton MR, Campbell PJ, Futreal PA. 2009. The cancer genome. Nature 458:719-724

Stützer K, Bert C, Enghardt W, Helmbrecht S, Parodi K, Priegnitz M, Saito N, Fiedler F. 2013. Experimental verification of a 4D reconstruction algorithm used for in-beam PET measurements in particle therapy. Phys Med Biol 58(15):5085-5111

Surti S, Karp JS, Popescu LM, Daube-Witherspoon ME, Werner M. 2006. Investigation of time-of-flight benefit for fully 3-D PET. IEEE Trans Med Imaging 25(5):529-538

Surti S, Kuhn A, Werner ME, Perkins AE, Kolthammer J, Kamp JS. 2007. Performance of a Philipps Gemini TF PET/CT scanner with a special consideration for its time-of-flight imaging capabilities. Journal of Nuclear Medicine 48(3):471-480

Surti S, Zou W, Daube-Witherspoon ME, McDonough J, Karp JS. 2011. Design study of an in situ PET scanner for use in proton beam therapy. Phys Med Biol 56:2667-2685

Takahashi W, Nakajima M, Yamamoto N, Tsuji H, Kamada T, Tsujii H. 2014. Carbon ion radiotherapy in a hypo-fractionation regime for stage I non-small cell lung cancer. J Radiat Res 55(Suppl. 1):i26-i27

Tashima H, Yamaya T, Yoshida E, Kinouchi S, Watanabe M, Tanaka E. 2012. A single-ring OpenPET enabling PET imaging during radiotherapy. Phys Med Biol 57(14):4705-4718

Thirolf PG, Lang C, Aldawood S, v.d. Kolff HG, Maier L, Schaart DR, Parodi K. 2014. Development of a Compton Camera for Online Range Monitoring of Laser-Accelerated Proton Beams via Prompt-Gamma Detection. EPJ Web of Conferences 66(11036)

Tindall CS, Palaio NP, Ludewigt BA, Holland SE, Larson DE, Curtis SW, McBride SE, Moreau T, Lin RP, Angelopoulos V. 2008. Silicon detectors for low energy particle detection. IEEE Trans Nucl Sci 55(2):797-781

Tomitani T, Pawelke J, Kanazawa M, Yoshikawa K, Yoshida K, Sato M, Takami A, Koga M, Futami Y, Kitagawa A, Urakabe E, Suda M, Mizuno H, Kanai T, Matsuura H, Shinoda I, Takizawa S. 2003. Washout studies of ^{11}C in rabbit thigh muscle implanted by secondary beams of HIMAC. Phys Med Biol 48(7):875-889

Toshito T, Kodama K, Sihver L, Yusa K, Ozaki M, Amako K, Kameoka S, Murakami K, Sasaki T, Aoki S, Ban T, Fukuda T, Komatsu M, Kubota H, Naganawa N, Nakamura T, Nakano T, Natsume M, Niwa K, Takahashi S, Yoshida J, Yoshida H, Kanazawa M, Kanematsu N, Komori M, Sato S, Asai M, Koi T, Fukushima C, Ogawa S, Shibasaki M, Shibuya H. 2007. Measurements of total and partial charge-changing cross sections for 200- to 400-MeV/nucleon C12 on water and polycarbonate. Phys Rev C Nucl Phys 75(5):054606

Tripathi RK, Cucinotta FA, Wilson JW. 1999. Accurate universal parameterization of ab-

sorption cross sections III - light systems. Nucl Instrum Methods B 155(4):349-356

Tsao CH, Silberberg R, Barghouty AF, Sihver L, T. Kanai. 1993. Scaling algorithm to calculate heavy-ion spallation cross sections. Phys Rev C Nucl Phys 47:1257-1262

Tsao CH, Silberberg R, Barghouty AF, Sihver, L. 1995. Energy degradation in cosmic-ray nuclear spallation reactions: relaxing the straight-ahead approximation. Astrophys J 451:275-283

Verburg JM, Riley K, Bortfeld T, Seco J. 2013. Energy- and time-resolved detection of prompt gamma-rays for proton range verification. Phys Med Biol 58(20):37-49

Von Essen CF, Bagshaw MA, Bush SE, Smith AR, Kligerman MM. 1987. Long-term results of pion therapy at Los Alamos. Int J Radiat Oncol Biol Phys 13(9):1389-1398

Watts D, Borghi G, Sauli F, Amaldi U. 2013. The use of multi-gap resistive plate chambers for in-beam PET in proton and carbon ion therapy. J Radiat Res 54(Suppl. 1):136-142

Watts D. 2013. Detectors for quality assurance in hadrontherapy. Escola de Postgrau. Universitat Autònoma de Barcelona. Departament de fisica. PhD Thesis.

Wilson RR. 1946. Radiological use of fast protons. Radiology 47(5):487-91

Woo SY. 2012. Rationale for Proton Therapy in Pediatric Malignancies. In: Linz U (ed) Ion Beam Therapy. Springer-Verlag, Berlin, Heidelberg, p. 277-286

Zeil K, Baumann M, Beyreuther E, Burris-Mog T, Cowan TE, Enghardt W, Karsch L, Kraft SD, Laschinsky L, Metzkes J, Naumburger D, Oppelt M, Richter C, Sauerbrey R, Schürer M, Schramm U, Pawelke J. 2013. Dose-controlled irradiation of cancer cells with laser-accelerated proton pulses. Appl Phys B 110(4):437-444

Zoglauer A. 2005. First light for the next generation of compton and pair telescopes. Technische Universität München, Fakultät für Physik, PhD Thesis

Acknowledgement

First of all, I would like to thank Prof. Wolfgang Enghardt for the supervision of this thesis, the encouraging and instructive conversations, and his confidence in me.

The next person to thank is Dr. Fine Fiedler. I am indepted to her because of the substantial supervision and the numerous ideas. She was available at every moment for my questions.

In 2012 I worked six months at Chalmers University of Technology in the wonderful town of Gothenburg / Sweden. I am grateful to Prof. Wolfgang Enghardt for this fantastic opportunity. Likewise I thank a lot Prof. Lembit Sihver for hosting me in his nice group at the Department of Nuclear Engineering. His help and suggestions concerning the activities with the simulation tools PHITS and HIBRAC were indespensable.

In addition to this, I would like to thank my helpful colleages Christian Golnik, Stephan Helmbrecht, Nicolas Hertel, Fernando Hueso-González, Dr. Thomas Kormoll, Andreas Schumann, Dr. Guntram Pausch, Dr. Marlen Priegnitz, Sebastian Schöne, and Dr. Kristin Stützer for their important hints, the constructive discussions, and the funny breaks.

Moreover, I have to thank my boyfriend Tobias, my parents and my brothers for their support and comprehension, especially during the time I spent in Sweden.

I will always keep the years as a PhD student in good memory and I am happy to be given the chance to contribute to this exciting field of research.

This work was performed in the framework of the ENVISION project funded by the EU (FP7, grant agreement number 241851).

Anlage 1

Technische Universität Dresden
Medizinische Fakultät Carl Gustav Carus
Promotionsordnung vom 24. Juli 2011

Erklärungen zur Eröffnung des Promotionsverfahrens

1. Hiermit versichere ich, dass ich die vorliegende Arbeit ohne unzulässige Hilfe Dritter und ohne Benutzung anderer als der angegebenen Hilfsmittel angefertigt habe; die aus fremden Quellen direkt oder indirekt übernommenen Gedanken sind als solche kenntlich gemacht.

2. Bei der Auswahl und Auswertung des Materials sowie bei der Herstellung des Manuskripts habe ich Unterstützungsleistungen von folgenden Personen erhalten: Prof. Dr. W. Enghardt, Dr. F. Fiedler, Prof. Dr. Lembit Sihver und Dr. M. Priegnitz

3. Weitere Personen waren an der geistigen Erstellung der vorliegenden Arbeit nicht beteiligt. Insbesondere habe ich nicht die Hilfe eines kommerziellen Promotionsberaters in Anspruch genommen. Dritte haben von mir weder unmittelbar noch mittelbar geldwerte Leistungen für Arbeiten erhalten, die im Zusammenhang mit dem Inhalt der vorgelegten Dissertation stehen.

4. Die Arbeit wurde bisher weder im Inland noch im Ausland in gleicher oder ähnlicher Form einer anderen Prüfungsbehörde vorgelegt.

5. Die Inhalte dieser Dissertation wurden in folgender Form veröffentlicht:

    - Golnik C, Dersch U, Fiedler F, Kormoll T, **Rohling H**, Enghardt W. 2011. A pair production upgrade for a Compton imager for in-vivo dosimetry at therapeutic proton and ion beams. IEEE Nucl Sci Symp Conf Rec (2011):3323-3326
    - **Rohling H**, Dersch U, Fiedler F, Golnik C, Kormoll T, Müller A, Schöne S, Enghardt W. 2012. Monte-Carlo simulation to optimize SPECT-hardware dedicated to in-beam control of particle therapy. Poster auf der ICTR-PHE Konferenz 2012 in Genf / Schweiz, Abstract in Radiother Oncol 102(Suppl. 1):46
    - Diblen F, **Rohling H**, Torres-Espallardo I, Solevi P, Gillam J, Watts D, España S, Vandenberghe S, Fiedler F, Rafecas M. 2012. Comparison study of RPC and crystal based PET systems for hadron therapy monitoring. IEEE Nucl Sci Symp Conf Rec (2012):2212-2217
    - **Rohling H**, Enghardt W, Hertel N, Kormoll T, Pausch G, Fiedler F. 2013. GEANT4 Simulationen zur Optimierung einer Compton Kamera für die In-vivo

Dosimetrie. Poster auf der DGMP-Jahrestagung 2013 in Köln, Abstract in Medizinische Physik (2013):710

- **Rohling H**, Sihver L, Priegnitz M, Enghardt W, Fiedler F. 2013. Comparison of PHITS, GEANT4, and HIBRAC simulations of depth-dependent yields of β^+-emitting nuclei during therapeutic particle irradiation to measured data. Phys Med Biol 58(18):6355-6368
- Kormoll T, Golnik C, Akhmadaliev S, Bemmerer D, Borany Jv, Fiedler F, Hueso-González F, Heidel K, Kempe M, **Rohling H**, Schmidt K, Schöne S, Wagner L, Pausch G. 2013. Compton Imaging in a high energetic photon field. IEEE Nucl Sci Symp Conf Rec (2013)
- **Rohling H**, Sihver L, Priegnitz M, Enghardt W, Fiedler F. 2014. Comparison of simulations with PHITS and HIBRAC with experimental data in the context of particle therapy monitoring. Poster auf der HITSRS Konferenz in Chiba / Japan, Peer-reviewed Abstract in Radiat Res 55(Suppl. 1):i43-i44

Eingereichte Manuskripte:

- **Rohling H**, Golnik C, Enghardt W, Hueso-González F, Kormoll T, Müller A, Pausch G, Fiedler F. 2014. Evaluation of a combined pair production - Compton camera for in-vivo dosimetry during therapeutic particle irradiation. Eingereicht bei Trans Nucl Sci
- Torres-Espallardo I, Diblen F, **Rohling H**, Solevi P, Gillam J, Watts D, España S, Vandenberghe S, Fiedler F, Rafecas M. 2014. Evaluation of Resistive-Plate-Chamber-based TOF-PET applied to in-beam Particle Therapy Monitoring. Eingereicht bei Phys Med Biol

6. Ich bestätige, dass es keine zurückliegenden erfolglosen Promotionsverfahren gab.
7. Ich bestätige, dass ich die Promotionsordnung der Medizinischen Fakultät Carl Gustav Carus der Technischen Universität Dresden anerkenne.
8. Ich habe die Zitierrichtlinien für Dissertationen an der Medizinischen Fakultät der Technischen Universität Dresden zur Kenntnis genommen und befolgt.

Anlage 2

Hiermit bestätige ich die Einhaltung der folgenden aktuellen gesetzlichen Vorgaben im Rahmen meiner Dissertation (Nicht angekreuzte Punkte sind für meine Dissertation nicht relevant.)

- ☐ das zustimmende Votum der Ethikkommission bei Klinischen Studien, epidemiologischen Untersuchungen mit Personenbezug oder Sachverhalten, die das Medizinproduktegesetz betreffen
- ☐ die Einhaltung der Bestimmungen des Tierschutzgesetzes
- ☐ die Einhaltung des Gentechnikgesetzes
- ☒ die Einhaltung von Datenschutzbestimmungen der Medizinischen Fakultät und des Universitätsklinikums Carl Gustav Carus.